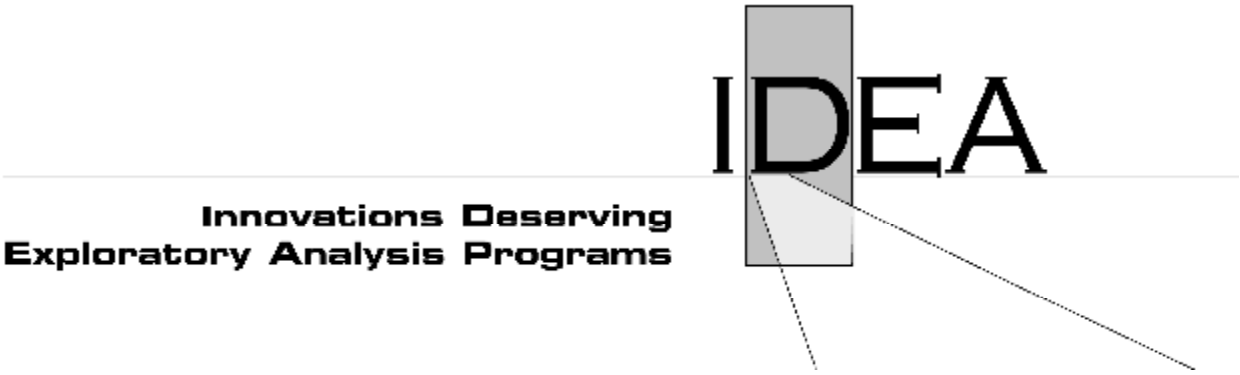


***Highway IDEA Program***

# Real-Time Remote Evaluation of Post-Event Residual Capacity of Highway Bridges

Final Report for Highway IDEA Project 137

Prepared by:
Maria Q. Feng  Newport Sensors, Inc.

***November 2010***

TRANSPORTATION RESEARCH BOARD
OF THE NATIONAL ACADEMIES

**INNOVATIONS DESERVING EXPLORATORY ANALYSIS (IDEA) PROGRAMS MANAGED BY THE TRANSPORTATION RESEARCH BOARD (TRB)**

This NCHRP-IDEA investigation was completed as part of the National Cooperative Highway Research Program (NCHRP). The NCHRP-IDEA program is one of the four IDEA programs managed by the Transportation Research Board (TRB) to foster innovations in highway and intermodal surface transportation systems. The other three IDEA program areas are Transit-IDEA, which focuses on products and results for transit practice, in support of the Transit Cooperative Research Program (TCRP), Safety-IDEA, which focuses on motor carrier safety practice, in support of the Federal Motor Carrier Safety Administration and Federal Railroad Administration, and High Speed Rail-IDEA (HSR), which focuses on products and results for high speed rail practice, in support of the Federal Railroad Administration. The four IDEA program areas are integrated to promote the development and testing of nontraditional and innovative concepts, methods, and technologies for surface transportation systems.

For information on the IDEA Program contact IDEA Program, Transportation Research Board, 500 5th Street, N.W., Washington, D.C. 20001 (phone: 202/334-1461, fax: 202/334-2081, http://www.nationalacademies.org/trb/idea)

# Real-Time Remote Evaluation of Post-Event Residual Capacity of Highway Bridges

**Project NCHRP-137**

**Final Report**

Prepared for

**The IDEA Program**

**Transportation Research Board**

**The National Academies**

**Maria Q. Feng**

Newport Sensors, Inc.

November 2010

# ACKNOWLEDGEMENT

This project is supported by the Innovations Deserving Exploratory Analysis (IDEA) Program, a part of the National Cooperative Highway Research Program (NCHRP), Transportation Research Board, the National Academies, and managed by Dr. Inam Jawed.

The project team would like to thank the NCHRP-IDEA Committee for their invaluable guidance and suggestions regarding the technical requirements for the proposed post-event damage assessment software and constructive comments on this final report. The in-kind support provided by Caltrans for long-term evaluation of the software is also highly appreciated.

# TABLE OF CONTENTS

# EXECUTIVE SUMMARY

The nation's sophisticated highway system is supported by hundreds of thousands of bridge and viaducts. Lack of rapid information about post-event structural integrity of these structures can cause safety hazards to the traveling public, halt mobility of the transportation network, and disrupt emergency response. The current practice relies on visual inspection for damage detection, which is time consuming, insufficient, subjective, and requires physical presence of inspection crew on the structure that is potentially hazardous after major natural or man-made events such as earthquakes, hurricanes, and terrorist attacks. The practice lacks the urgently needed elements for developing a rapid decision-making process that could be accomplished within minutes rather than days or months.

The emerging sensor-based structural health monitoring technology has shown its potential for rapid and remote assessment of structural damage. Despite the research progress made over the last decade, many important issues need to be addressed before the sensor-based damage assessment can be implemented to real bridges. Most of the studies demonstrate the effectiveness of damage assessment methods based on numerical simulation and/or small-scale laboratory tests involving highly artificial structural damage. Second, these methods often require establishment of a baseline that represents the structure's undamaged state, but the baseline is easily influenced by environmental conditions such as temperature and vibration levels. Third, there exists a significant gap between the research and the use of the research results for making post-event decisions on bridge operations and repair.

The primary objective of this project is to bridge the gap between the state of research and the state of the practice, by addressing the technically challenging issues. The scope of the study includes the development and large-scale experimental validation of methods and software for sensor-based, remote, real-time assessment of post-event integrity and safety

of highway bridge structures. It is proposed to use surface-attached accelerometers to monitor bridge vibration, assess structural damage by identifying change in structural stiffness caused by a destructive event based on the vibration data, and further evaluate residual capacity of a bridge based on the identified damage. By identifying the structural element stiffness degradation associated with damage, one can not only detect the occurrence but also locate the damage. A major innovation of the proposed damage assessment method is its independence of a baseline condition of the bridge. Another innovation is in the evaluation of the post-event residual capacity of a bridge based on the damage assessment results, which has never been studied in literature, but is important for making decision in terms of whether the bridge should be closed or partially closed immediately after the event and which bridge should be repaired first.

A significant value of this study is in the experimental validation of a number of promising approaches for damage assessment and capacity estimation, through a large-scale seismic shaking table test of a multi-bent multi-column concrete bridge. The experimental validation using such a realistic bridge model and realistic seismic damage enabled this project to address the most significant challenge faced in implementing the monitoring technology: How can we reliably link the sensor data to the state of structural damage and residual capacity?

In total, six methods have been developed and investigated for post-event damage assessment and capacity estimation of concrete bridges. For rapid damage screening to detect damage occurrence, two methods have been studied including the autoregressive method and the nonlinear damping methods. For detailed damage assessment (to identify occurrence, locations, and extent of damage), three methods have been studied, including the extended Kalman filtering method, the optimization method, and the genetic algorithm-based optimization method. For remaining capacity estimation, a pushover analysis-based method has been developed. None of these methods requires an undamaged baseline model. All these methods have been validated by the large-scale seismic shaking table test.

Although all these methods achieved similar damage assessment results that were consistent with visual inspection and measurement though embedded strain gauges on the bridge (the embedment of strain gauges is not feasible in the field, though), some of the approaches have been selected to implement in an exploratory software package due to their computational stability and efficiency.

A major product of this IDEA project is the software package, referred to as the Bridge Doctor. The software contains three integrated major functions: (1) rapid damage screening to detect occurrence of structural damage, (2) detailed damage assessment to evaluate the location and extent of damage, and finally (3) remaining capacity estimation based on the damage assessment results. The software can be installed on bridge owners' and/emergency responders' computers that are linked to instrumented bridges through Internet. An event will trigger sensor systems on the bridges and send the sensor data via Internet to the software in real time, making it possible to perform remote damage assessment of the bridges. The results will assist bridge owners and emergence responders to make decisions in terms of emergency response operations and post-even bridge repair/retrofit prioritization. In collaboration with Caltrans, the software package has been integrated with an existing sensor monitoring system on Jamboree Overcrossing in Irvine, CA, a concrete bridge testbed, for long-term evaluation and demonstration.

A five-year post-IDEA plan has been developed to drive the software to the marketplace. Although the software is focused on seismic damage of concrete bridges, the proposed approaches can be further developed to address other types of bridges and damage. In addition, these approaches can be applied to detect structural deterioration due to aging and assess bridge structural health and safety under operational loads. The real-time monitoring results can also assist bridge owners to make objective decisions when prioritizing bridges for maintenance and rehabilitation, as well as to improve the current bridge structural design.

# 1. IDEA PRODUCT

This IDEA project developed a sensor-based, real-time, remote system for post-event damage assessment and remaining capacity estimation of highway bridges, which consists of the following steps: (1) installing surface-attached accelerometers at critical locations of a bridge, (2) monitoring bridge vibration response during an event, (3) from the vibration characteristics, identifying changes in structural element stiffness and damping caused by the event, (4) assessing damage extents and locations based on the changes, and (5) estimating remaining capacity of the bridge based on the damage assessment results. Upon validation of a number of promising approaches for structural stiffness/damping identification, damage assessment, and capacity estimation by means of seismic shaking table tests, this project implemented selected approaches into an exploratory software package. Finally the project has delivered the following unique products:

1. A final report that describes recommended methods and algorithms, together with user guidelines, for post-event damage assessment and capacity estimation of highway bridges, which have been validated through large-scale seismic shaking table tests,

2. An exploratory software package incorporated with the selected damage assessment and capacity estimation methods and algorithms developed in this project, and

3. A testbed bridge in California that is instrumented with accelerometers, equipped with real-time data transmission capability, and integrated with the developed software for long-term evaluation, demonstration, and user training.

# 2. CONCEPT AND INNOVATION

## 2.1 BACKGROUND

Post-event damage assessment of structures typically requires a detailed and time-consuming visual inspection and evaluation. Lack of information about damage in highway bridges immediately after an event can cause safety hazards, halt mobility of the transportation network and disrupt emergency response. The vivid image in Fig. 1 reported by the Los Angeles Times after the 1994 Northridge earthquake reminds us the needs for a rapid, automated post-event damage assessment system.

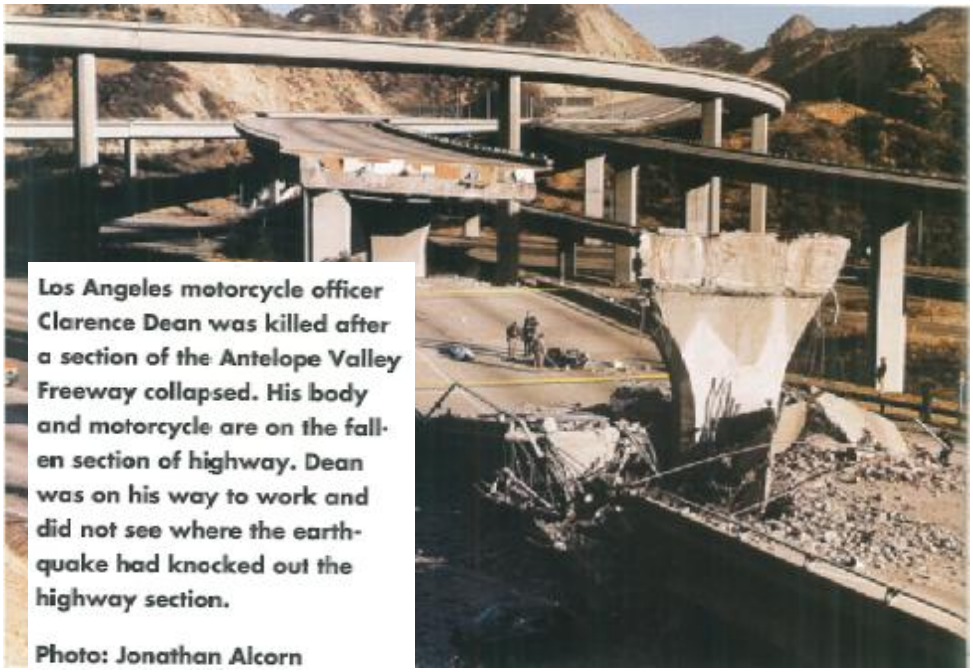


Figure 1 Needs for Rapid Post-Event Damage Assessment

The emerging sensor-based structural health monitoring technology has shown its potential for significantly improving the conventional structural inspection, particularly for post-event damage assessment. By installing appropriate sensors at critical locations on a bridge structure, transmitting the sensor data through a communication network, and analyzing the data through a software package, the locations and severity of bridge damage caused by a destructive event can be automatically, remotely, and rapidly assessed, without sending inspection crew to the site. Once the damage and residual capacity are evaluated, early warning can be issued by the traffic management center in real time to re-route traffic for public safety. The general concept is illustrated in Fig. 2. Sensor data are transmitted from the bridge site through satellite, wireless or wired Internet to a control center, where the data are processed through the damage assessment software in real time.

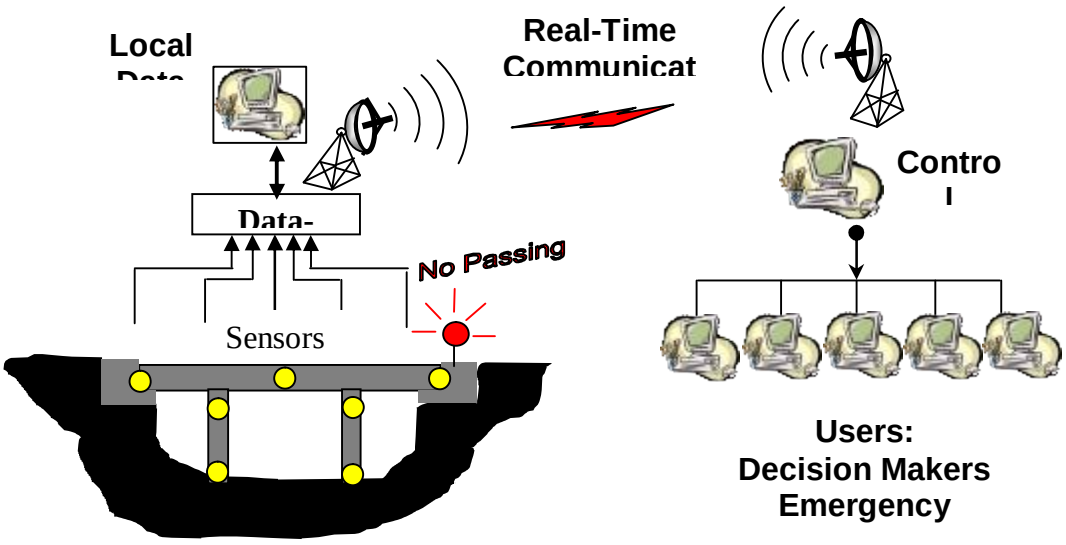


Figure 2. General Concept of Sensor-Based Damage Assessment

Over the last decade, a considerable amount of research has been carried out in both hardware (sensors and sensor networks) and software aspects of structural health monitoring. Particularly, research on vibration-based structural health monitoring and damage detection has produced substantial literatures (e.g., Doebling et al., 1996, Sohn et al. 2003).

Despite the research progress, many important issues still need to be addressed before the sensor-based damage assessment can be implemented in real bridges. First of all, most of the studies demonstrate the effectiveness of damage assessment methods based on numerical simulation and/or small-scale laboratory tests involving highly artificial structural damage. Second, most of the methods require establishment of a baseline that represents the undamaged state of a structure, which is difficult to implement because the baseline is easily influenced by environmental conditions such as temperature and vibration levels. Third, there exists a significant gap between damage assessment results and the use of the results for making decisions (such as post-event bridge closure, prioritization of bridge repair/retrofit).

## 2.2 PROPOSED CONCEPT AND MAJOR INNOVATION

The ultimate goal of this IDEA project is to close the gap between the state of research and the state of the practice by addressing the above-mentioned obstacles that prevent the implementation of the sensor-based damage assessment. The project proposes to use surface-attached accelerometers to monitor bridge vibration, assess post-event structural damage by identifying changes in structural element stiffness and/or damping based on the vibration data during the event, and further evaluate residual capacity of a bridge based on the identified damage. By identifying the amount of decrease in structural element stiffness and increase in nonlinear damping, one can detect not only damage occurrence but also locations of the damage.

In total, six methods have been developed and validated in this project: the autoregressive method and the nonlinear damping method for rapid damage screening; the extended Kalman filtering method, the quasi-Newton optimization method, and the genetic algorithm-based optimization method for more detailed damage assessment (locations and extents), and a pushover analysis-based method for remaining capacity estimation.

A major innovation of these methods lies in their independence of a baseline that represents an undamaged state of a structural. It is difficult to establish a reliable baseline because it depends on the environmental conditions such as temperatures and moisture as well as the intensity of the bridge vibration. In this study, the structural damage assessment, including the rapid screening and the detailed assessment, are solely based on bridge vibration responses measured during an event, without requiring an undamaged baseline. For example, the two optimization methods focus on low-amplitude pre- and post-event responses and identify the difference in structural stiffness between these two states. It is noted that data recorders usually are equipped with buffers that can record pre-event

vibration. The extended Kalman filter method is capable of analyzing a nonlinear system and identifying the change of structural stiffness instantaneously during a damaging event.

Another major innovation of this project is in the evaluation of post-event residual capacity of a bridge based on the damage assessment results, which has never been studied in literature, but is critical for making decisions in terms of whether the bridge should be closed or partially closed immediately after the event and which bridge should be repaired first. This project proposes to superpose the identified equivalent stiffness of a structural element, such as a bridge column, to the analytical pushover curve of the element. The intersection of the pushover curve and the stiffness line indicates the current capacity. The remaining capacity of the column is then estimated by comparing the identified current capacity with the ultimate capacity,

A significant value of this study is in the experimental validation of a number of promising approaches for damage assessment and capacity estimation, by means of a large-scale seismic shaking table test of a multi-bent multi-column concrete bridge. Previous studies often use small-scale structural model subjected to unrealistic damage. The realistic bridge model and the realistic seismic damage enabled this project to address the most significant challenge faced in implementing the monitoring technology: How can we reliably link the sensor data to the state of structural damage and residual capacity?

Upon successful validation by means of the seismic shaking table tests, these methods were developed into computer algorithms and furthermore to an exploratory software package for rapid damage detection, detailed damage assessment, and remaining capacity estimation. This software package was further integrated with an existing sensor monitoring system on the Jamboree Overcrossing in Irvine, CA, a concrete bridge testbed, for long-term evaluation and demonstration. Currently no such a software package is available.

# 3. INVESTIGATION

In this chapter, the research objectives and scope are presented in Section 3.1. The seismic shaking table tests are described in Section 3.2. Then, the six damage assessment and capacity estimation methods are presented – the nonlinear damping method in Section 3.3, the autoregressive model in Section 3.4, the extended Kalman filter method in Section 3.5, the quasi-Newton optimization method in Section 3.6, the genetic algorithm-based optimization method in Section 3.7, and the pushover analysis-based method for remaining capacity estimation in Section 3.8. Finally the software and the testbed are described in Section 3.9

# 3.1 RESEARCH OBJECTIVES AND SCOPE

The overall objectives of this IDEA project are to (1) develop reliable and cost-effective methods and algorithms for assessing post-event structural damage and the residual load-carrying capacities of bridges, and (2) develop an exploratory software package to implement the damage/capacity assessment methods/algorithms, and further integrate the software with an existing sensor monitoring system on a Caltrans bridge for long-term evaluation and demonstration.

In this project, six methods have been developed and investigated for post-event damage assessment and capacity estimation of concrete bridges, based on vibration measurement, which include the autoregressive method and the nonlinear damping method for rapid damage screening; the extended Kalman filtering method, the quasi-Newton optimization method, and the genetic algorithm-based optimization method for more detailed damage assessment (locations and extents), and a pushover analysis-based method for remaining capacity estimation. All these methods have been validated by a seismic shaking table test of a multi-bent, multi-column realistic concrete bridge model progressively damaged by earthquake ground motions of increasing intensities. Based on the results, methods have been selected and developed into algorithms and furthermore an exploratory software package. The software has been integrated with a sensor monitoring system on the testbed bridge for long-term performance evaluation, demonstration and user training.

## 3.2 SEISMIC SHAKING TABLE TESTS

A significant value of this project is in the experimental validation of a number of promising damage assessment and capacity estimation methods, through expensive seismic shaking table tests on a large multi-bent multi-column bridge model, without costs to this project. Numerous damage assessment methods have been developed in the past, but this study represents the first effort in experimentally validating the methods using a realistic bridge subject to realistic seismic damage at various levels.

This project team collaborated with researchers at the University of Nevada, Reno (UNR) in their National Science Foundation-sponsored Network for Earthquake Engineering Simulation (NEES) project on concrete bridge seismic failure studies. Shake table tests were performed on a two-span three-bent reinforced concrete bridge specimen, shown in Fig. 3. Each of the three bents was supported on an individual shake table. The bents were linked by the bridge deck, with a total length of 720 in. Each bent consisted of two columns, having the same design cross sections with a diameter of 12 in. The bents were of different heights, 72 in, 96 in, and 60 in for Bents 1, 2, and 3, respectively, resulting in different column stiffness values. To resemble the inertia of other parts of the superstructure not built into this model, compensative masses were added.

Eleven channels (CH) of accelerometers were installed on the specimen to obtain the acceleration ground motion inputs and responses of the bridge, as illustrated in Fig. 3. In addition, numerous strain gauges were installed (embedded) on the rebar in the column plastic hinge zones during the bridge construction. Displacement sensors were also installed on the tops of the bents.

The shake tables were driven by input acceleration signals in the transverse direction of the

bridge. During the tests, earthquake ground motions of increasing intensity, from low, moderate, high, severe, and extreme, were used as the driving signals of the shake tables to simulate strong motions. Table 1 shows the sequence of the strong motions denoted by "T-number" and their input peak ground accelerations (PGA). Different levels of damage were introduced to the bridge model by these strong motions. In between the strong motions, low-amplitude white noise simulating ambient vibration, denoted by "WN-number" with a PGA of approximately 0.05*g*, drove the shake tables to perturb the specimen in the corresponding damage level. Such perturbations did not introduce further nonlinearity and the system under a perturbation behaved as a linear system with a stable stiffness.

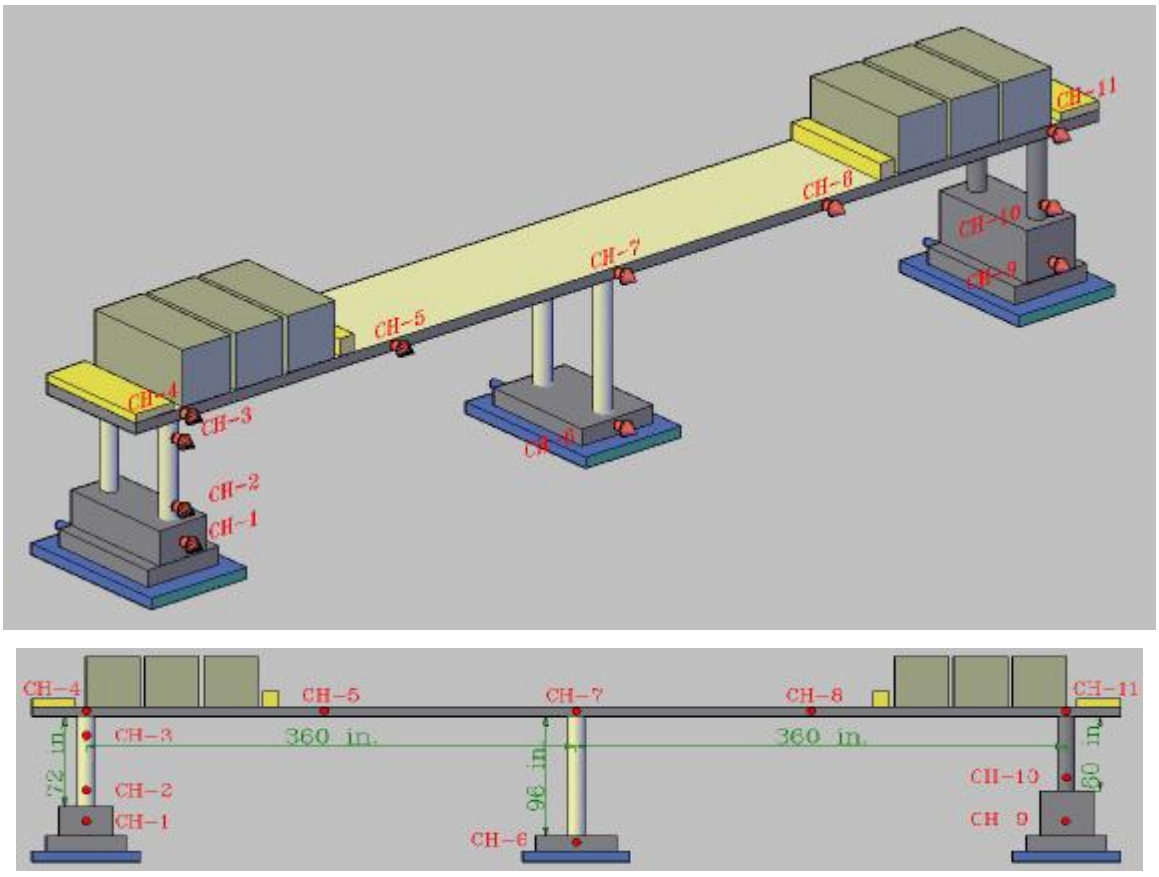


Figure 3 Seismic Shaking Table Test of Concrete Bridge

Table 1 Shaking Table Test Procedure

| Tests | Ground Motion Description | PGA (g) | Damage Description |
|---|---|---|---|
| WN-1 | Ambient White Noise | 0.0723 | |
| T-12 | Low Earthquake | 0.0851 | |
| T-13 | Low Earthquake | 0.1729 | Bent 1 Yields |
| T-14 | Moderate Earthquake | 0.3193 | Bent 3 Yields |
| WN-2 | Ambient White Noise | 0.0723 | |
| T-15 | High Earthquake | 0.6272 | Bent 2 Yields |
| T-16 | Severe Earthquake | | |
| T-17 | Extreme Earthquake | 1.135 | |
| WN-3 | Ambient White Noise | 0.0723 | |
| T-18 | Extreme Earthquake | 1.3975 | |
| T-19 | Extreme Earthquake | 1.7033 | Bent 3 Steel Buckles |
| WN-4 | Ambient White Noise | 0.0723 | |

The sequence of the earthquake inputs with increasing intensities successfully induced seismic damage to the bridge columns at different extents. Damage of the bridge columns after each earthquake shaking is shown in the photos in Fig. 4. Using Bent 1 as an example, as the damage accumulated, more and more cracks were observed, and finally concrete spalls were observed at the bottom of the column.

The cracks, however, are not clear indication of the formation of a plastic hinge. In this experiment, advantages were taken of the densely instrumented strain gauges on the steel rebars embedded before concrete casting to read the deformation of the steels, based on which yielding of the bents was found. As indicated in Table 1, the damage procedure observed can be outlined as: Bent 1 yields **à** Bent 3 yields **à** Bent 2 yields **à** Bent 3 steel buckles. This sequence is largely determined by the relative heights of the bents. The onset of Bent 1 yielding is due to the fact that the first mode of this bridge specimen (in its

undamaged stage) has the largest displacement on Bent 1. After the yielding of Bent 1, Bent 3 attracts most the seismic force and yields, and then so happens to Bent 2 after the yielding of Bents 1 and 3. The final collapse (in the test, the specimen was protected to avoid actual collapse) is associated with the steel buckling at Bent 3, which has the smallest ductility capacity among the three.

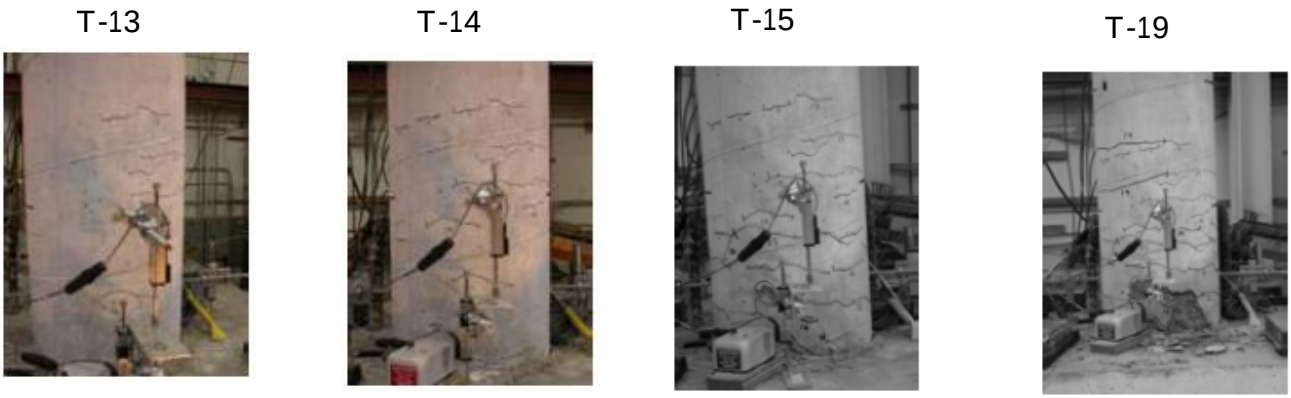


(a) Damage on Bent-1 after each test


(b) Damage on the upper and lower portion of Bent-3 after T-14

Figure 4 Observed Seismic Damage

On existing bridges, however, such dense strain gauge installation is hardly possible. On the contrary, the sectional stiffness reduction obtained by system identification based on acceleration measurement requires only minor instrumentation efforts (surface attached accelerometers vs. embedded strain gauges) and can be implemented on an already existing

structure. And as to be illustrated later, the reduction (represented by correction coefficients of sectional stiffness) correlates satisfactorily with the damage sequence.

In this study, the seismic and ambient responses of the bridge recorded by the accelerometers are used to identify the seismic damage of the bridge, based the proposed methods as described in the following sections. The identification results are then compared with visual inspection as well as those recorded by the embedded strain gauges. Again, the surface attached accelerometers are much more desirable than the embedded strain gauges for the purpose of damage detection, due to their ease of installation on existing bridges as well as new bridges.

# 3.3 DAMAGE DETECTION BASED ON DAMPING ANALYSIS

Damping in a structure is directly associated with structural damage; damage increases friction damping. Although damping in a concrete structure has been widely studied, very few investigations have been conducted to take advantage of the damping change to detect structural damage. The proposed method uses nonlinear damping as a damage index and predicts the presence of damage in a structural without requiring any reference to its undamaged baseline.

A major innovation for applying this method to detect seismic damage is in the use of the random decrement signature technique that enables the process of ambient vibration into decayed free vibration signals for damping assessment. Ambient vibrations are the most accessible data that can be acquired from a real structure, since the measurement requires neither the structure being taken out of service, nor expensive exogenous excitations.

In this project, the results from seismic shaking table tests of the large-scale three-bent bridge model are used to validate the method. The realistic bridge model and its realistic seismic damage at different levels caused by progressive seismic shaking enables a complete evaluation of the efficacy of the proposed damage detection method.

## 3.3.1 Nonlinear Damping and Damage

Damping in a vibrating structure is associated with dissipation of mechanical energy. The energy dissipation equals the work done by the damping force. In case of a free vibration

the presence of damping results in a continuous decay of the amplitude. If the motion is an oscillation, for every cycle the quantity of energy loss $\Delta E$ can be expressed as:

$$\Delta E = \oint \sigma d\varepsilon \tag{1}$$

where $\sigma$ is the stress (or internal force) and $\varepsilon$ is the strain (or deformation). This quantity can be represented as the area inside the hysteretic loop formed for each cycle.

If the system is modeled as a simple linear oscillator, the differential equation of motion is expressed as:

$$m\ddot{x} + c\dot{x} + kx = F(t) \tag{2}$$

where $x$ is the displacement, $m$ is the mass, $k$ is the stiffness and $c$ is the damping coefficient, while $F(t)$ is the external excitation. In an undamaged condition, the dissipation of energy is due mostly to material damping, which appears macroscopically viscous, i.e. proportional to the velocity of motion. The energy dissipated per cycle becomes:

$$\Delta E_{visc} = \int_0^T (c\dot{x})\dot{x}dt = \pi c\omega x_0^2 \tag{3}$$

where $\omega$ is the natural frequency of the system, $x_0$ is the initial amplitude of oscillation and the integral is taken over a period $T$.

A viscous damping ratio can be defined as:

$$\xi = \frac{1}{4\pi}\frac{\Delta E_{visc}}{E_{pot}} \tag{4}$$

where $E_{pot}$ is the maximum strain potential energy of the structure:

$$E_{pot} = \frac{1}{2} k x_0^2 \tag{5}$$

In case of free vibration, from Eqs. 3, 4 and 5 the viscous damping ratio becomes:

$$\xi = \frac{c}{2m\omega} \tag{6}$$

The damping behavior of reinforced concrete elements is strongly influenced by cracking. If the element is damaged, within the cracks the most significant dissipation mechanism can be represented, with the best agreement to the real behavior, with Coulomb friction. This is due to the phenomenon of slip between steel and concrete.

The differential equation that describes a purely friction-damped system is:

$$m\ddot{x} + F_C \frac{\dot{x}}{|\dot{x}|} + kx = F(t) \tag{7}$$

Where $F_C$ is the *friction force*, which is expressed with reference to the compression force $N$ acting between the surfaces, such as:

$$F_C = \mu N \tag{8}$$

Where $\mu$ is the friction coefficient, which depends only on the contact materials.

The energy loss per cycle for this model, with reference to Eq. 1, becomes:

$$\Delta E_{friction} = \int_0^{T} F_C \frac{\dot{x}}{|\dot{x}|} \dot{x} dt = 4F_C x_0 \tag{9}$$

An equivalent frictional damping ratio can be therefore defined as:

$$\gamma = \frac{1}{4\pi} \frac{\Delta E_{friction}}{E_{pot}} = \frac{2F_C}{\pi k x_0} \tag{10}$$

Unlike the viscous damping ratio, this parameter is dependent on the initial amplitude $x_0$.

Figure 5 shows a comparison between the hysteretic loops obtained from the two models of viscous and friction damping respectively. Unlike the viscous damping, the shape of the hysteretic loop of the friction system is due to the fact that the damping force has a constant intensity, always opposite to the direction of motion, as seen in Eq. 7.

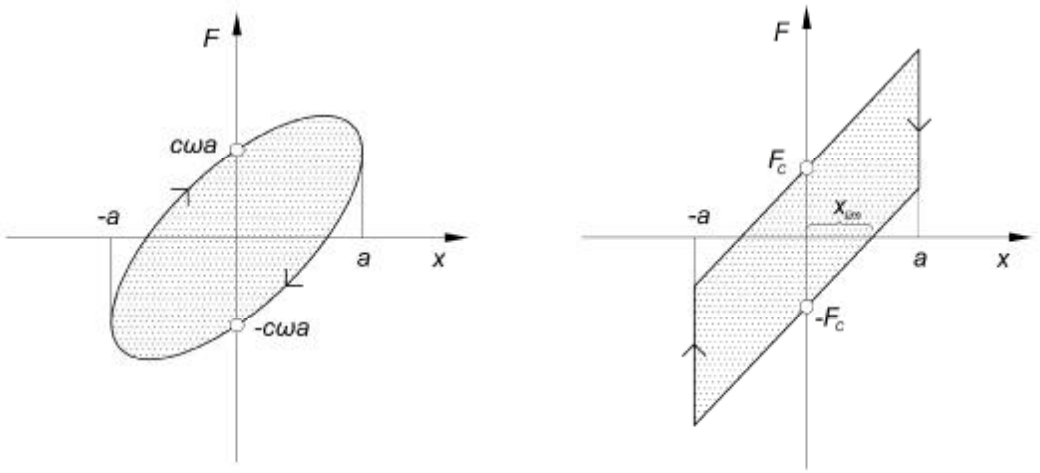


(a) Viscous damping (b) Friction damping

Figure 5. Hysteretic Loops

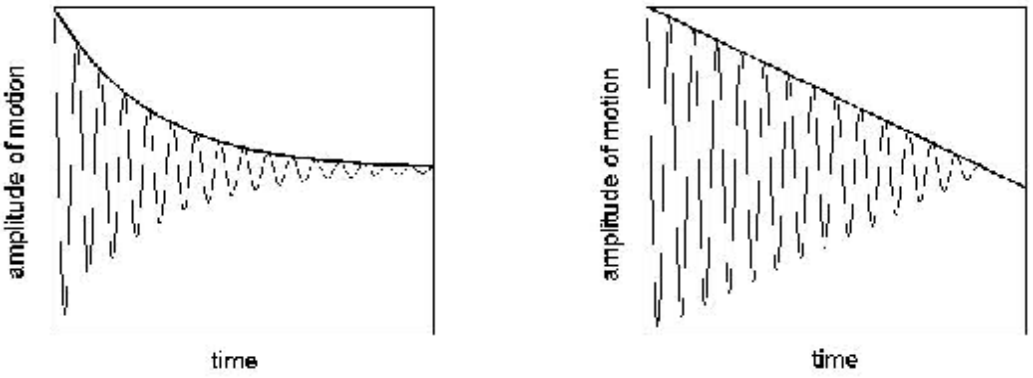


(a) Viscous damping (b) Friction damping

Figure 6. Free decay

The solutions of Eqs. 2 and 7, in case of free vibration, are represented in Fig. 6.

The envelopes of these decays ***a(t)*** represented in Fig. 6 can be expressed respectively as:

$$a(t) = x_0 e^{-\gamma \omega t} \qquad \text{for viscous damping} \qquad (11)$$

$$a(t) = x_0 \left( 1 - \frac{2}{\pi} \frac{x_{lim}}{x_0} \omega t \right) \qquad \text{for friction damping} \qquad (12)$$

where $x_{lim}$ is the limit displacement in static equilibrium, defined as:

$$x_{lim} = \frac{F_C}{k} \qquad (13)$$

From Eqs. (10) and (13) the frictional damping ratio $\gamma$ can be expressed as:

$$\gamma = \frac{2 x_{lim}}{\pi . x_0} \qquad (14)$$

Therefore, Eq. 12 becomes:

$$a(t) = x_1(1 - \gamma\omega t) \tag{15}$$

Considering its complexity, a cracked bending element, where both the viscous and friction damping phenomena co-exist at the same time, can be modeled as a combined system. In particular, Figure 7 shows that in the cracked zone where there is friction in the reinforcement surface, the most significant dissipation mechanism is the friction damping. On the contrary, in the compression zone, it can be assumed that only material (viscous) damping is present. Therefore, the bending element can be modeled as shown in Fig. 7, where the *k* represents the bending stiffness of the element, while *m* the relevant mass.

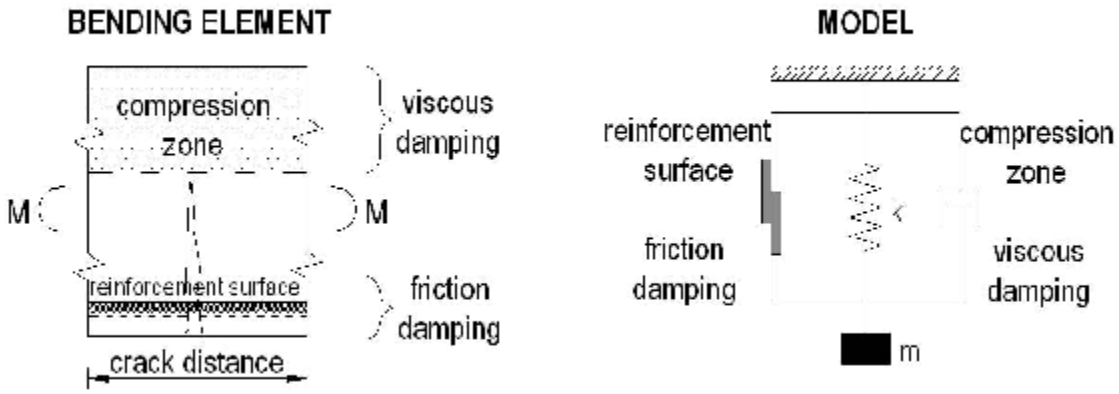


Figure 7. Cracked Bending Element and Corresponding model

The mass-normalized equation of motion of the combined model becomes:

$$\ddot{x} + 2\omega\xi\dot{x} + \omega^2 x_{limit}\frac{\dot{x}}{|\dot{x}|} + \omega^2 x = 0 \tag{16}$$

The solution of Eq.16 can be found through a numerical integration. A sufficiently accurate approximation for practical purposes is obtained, assuming that the total loss of energy $\Delta E_{tot}$ can be interpreted as a simple sum of the viscous and the friction dissipations. If no external forces act on the system (i.e., free vibration), $\Delta E_{tot}$ is equal to the variation of potential energy of the system, i.e.:

$$\Delta E_{tot} = \Delta E_{visc} + \Delta E_{frict} \tag{17}$$

In presence of a Coulomb friction mechanism, the free motion is generally not an exponentially decayed oscillation. However, a sinusoidal solution of Eq. 16 is acceptable when elastic forces are greater than friction forces. In this case, the three terms in Eq. 17 can be replaced with Eqs. 3, 5 and 9, this time considering $x$ instead of $x_0$, since the balance is not yet integrated in time:

$$\Delta\left(\frac{1}{2}\omega^2 x^2\right) = 2\pi\xi\omega^2 x^2 + 4\omega^2 x_{lim} x \tag{18}$$

The same balance can be expressed in terms of power, dividing each member by $\Delta t = T = 2\pi/\omega$, and obtaining:

$$\frac{\Delta x}{\Delta t} = \xi\omega x + \frac{2}{\pi}\omega x_{lim} \tag{19}$$

By integrating Eq. 19 over a period the solution of Eq. 16 can be obtained. Its envelope can be expressed, considering Eqs. 6 and 14 as a function of the initial amplitude $x_0$, the natural frequency of the system $\omega$ and the two damping ratios $\xi$ for viscous damping and $\gamma$ for friction damping:

$$a(t) = x_0 \left[ \left( 1 + \frac{\gamma}{\xi} \right) e^{-\xi \cdot \omega \cdot t} - \frac{\gamma}{\xi} \right] \tag{20}$$

Figure 8 shows the free decay of the described combined model, as defined in Eq. 20.

The values of $\gamma$ and $\xi$ will give information about the percentage of the total energy dissipated by each damping phenomenon. $\gamma=0$ means that no friction damping acts on the system: therefore no cracks are present. On the contrary, a positive value of $\gamma$ means that a frictional dissipation acts on the element. Therefore the friction damping ratio $\gamma$ can be directly correlated to the presence of damage in the considered concrete element.

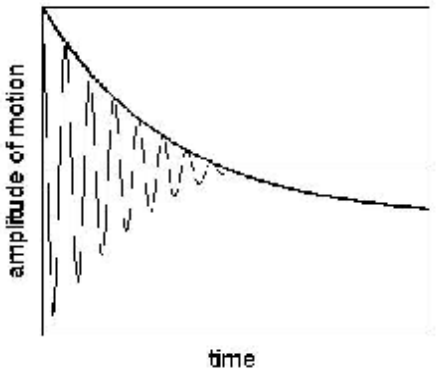


Figure 8. Free Decay for Viscous and Friction Combined Model.

### 3.3.2 Damage Detection from Impulse Response

The proposed procedure for damage detection starts from the analysis of a free vibration of the considered structure, given as a response to an impulse excitation. A free mono-frequency signal is extracted from the response of the structure and the envelope of the decay derived, by picking the oscillation peaks. For every period of oscillation two values –

positive and negative peak – are extracted, by simply considering the opposite value of the negative peaks.

Therefore, concrete damage can be detected based on the shape of the envelope -- the pure exponential decay as shown in Fig. 7(a) indicates no damage, while the combined decay as in Fig. 8 indicates damage. By fitting the measured decayed free vibration signal to both Eqs. 11 and 20, the values of $\xi$ and $\gamma$ can be obtained and subsequently damage assessed.

### 3.3.3 Damage Detection from Ambient Vibration Response

As presented above, the nonlinear damping-based damage detection method analyzes the free vibration or impulse response signals. For large-scale concrete structures in the field, however, it is not practical to obtain such free vibration or impulse response.

This project developed the nonlinear damping-based damage detection method for concrete structures using ambient vibration response, instead of free vibration. In general it is relatively easy to obtain ambient vibration responses without requiring equipment to excite the structure. The random decrement technique is applied to process the measured ambient vibration response to obtain free vibration signals. The technique is based on averaging of sub-segments extracted from the random signal and chosen with appropriate criteria (referred to as triggering conditions). The averaging procedure results in a random decrement (RD) signature, which minimizes the random component in the original signal by leaving only the response to the triggering conditions.

In literature many different triggering conditions can be found. In this study the level crossing triggering condition is employed. Every time the signal crosses the chosen triggering level, a sub-segment is formed. The resulting RD signature is a free decay with

initial value equal to the chosen triggering level. The concept can be expressed with the simple formula:

$$z(\tau) = \frac{1}{N}\sum_{i=1}^{N} y(t_i + \tau) \qquad (21)$$

Where $z(\tau)$ is the RD signature, $\tau$ is the time reference of the sub-segments, $N$ is the number of averages, $y$ is the recoded data and $t_i$ is the time at which the triggering level is crossed. The concept of the algorithm is illustrated in Fig. 9.

The triggering level is usually chosen with reference to the standard deviation $\sigma$ of the distribution of the random response. Many studies suggested selecting $\sqrt{2}\sigma$ as the triggering level, since it corresponds to a minimum in the RD signature variance.

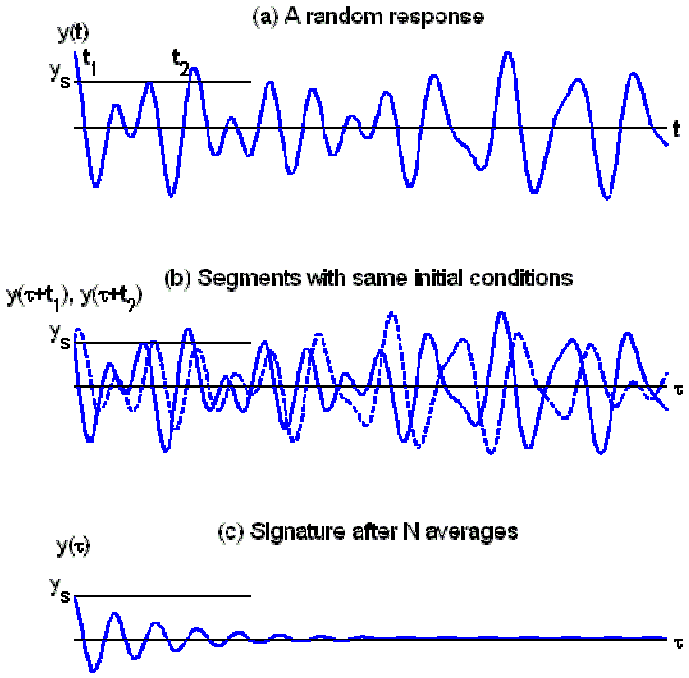


Figure 9. Extraction of RD Signature from a Random Response

### 3.3.4 Validation by Seismic Shaking Table Tests

The proposed nonlinear damping method is validated through the seismic shaking table tests of the three-bent two-column concrete bridge model. As described in Section 3.2, the bridge model was subjected to a series of low to high amplitude earthquakes, inducing progressive seismic damage to the structure. Between earthquake ground motions, low amplitude white noise excitations were input to the bridge structure to simulate ambient vibration. Eleven accelerometers were installed on the tables and bridge to record input ground motions and the responses of the structure.

The objective is to demonstrate that the nonlinear frictional damping ratio $\gamma$, can be reliably identified from the measured bridge vibration and furthermore $\gamma$ can serve as a reliable structural damage index by comparing the $\gamma$ value with the structural damage observed by visual inspection and by the embedded strain sensors (as presented in Table 1).

Figure 10 shows the procedure applied to the third white noise (WN-3) response of Bent-1. It consists of the following four steps: (a) choice of the triggering level with reference to (b) data distribution; (c) application of the random decrement signature and calculation of the envelope through both positive and negative peak picking; and (d) data fitting with the two described damping models.

In Fig. 11 the random decrement signatures obtained from the applied algorithm are shown; the calculated envelopes of the oscillation are also displayed. Figure 12 shows the same curves fitted with the two different models, i.e., the purely viscous model and the viscous-friction combined model.

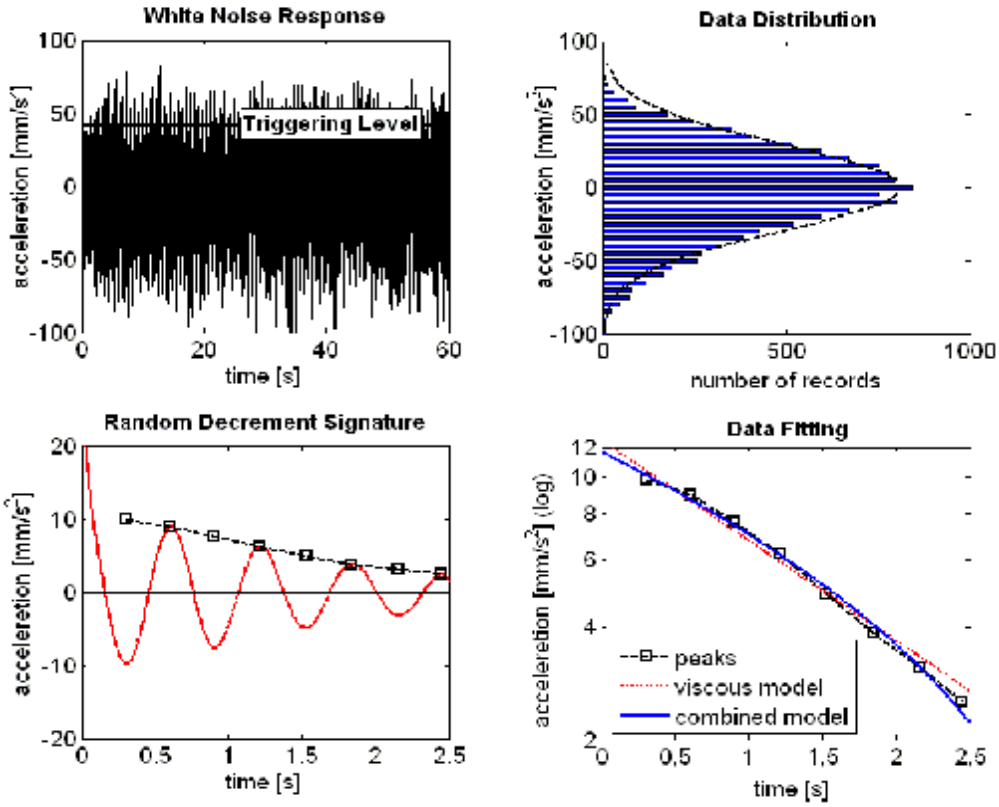


Figure 10. Procedure of Nonlinear Damping Analysis

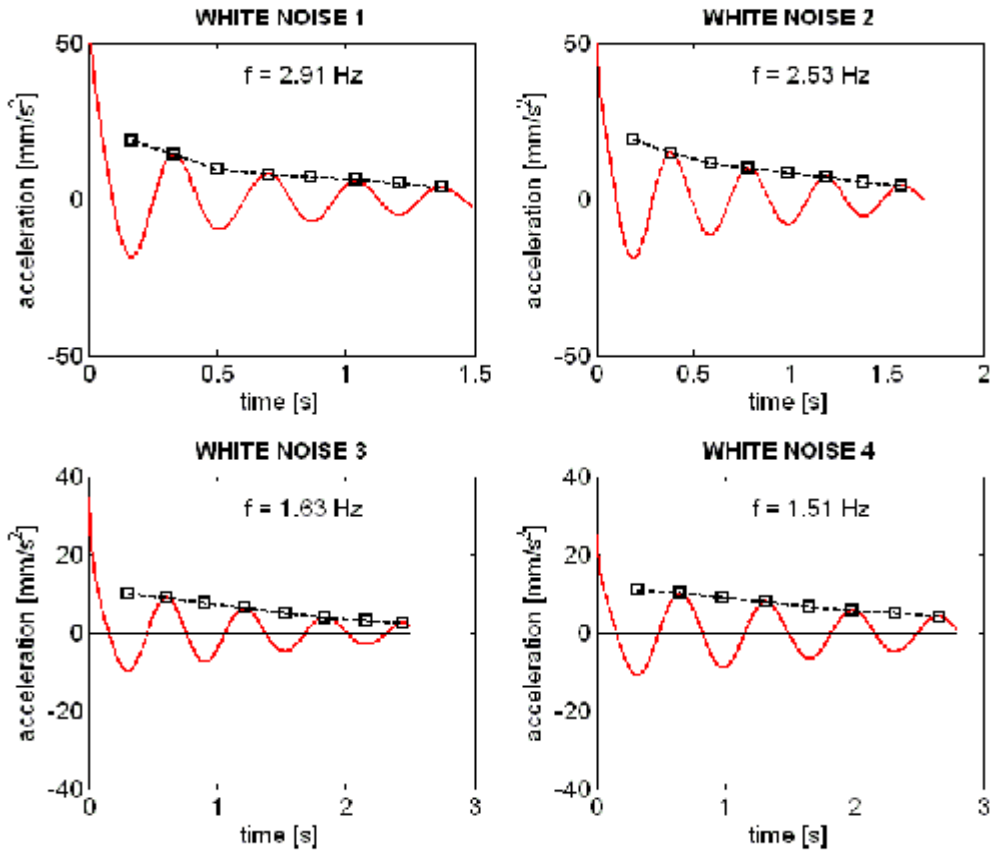


Figure 11. Random Decrement Signature and Envelopes of Oscillation.

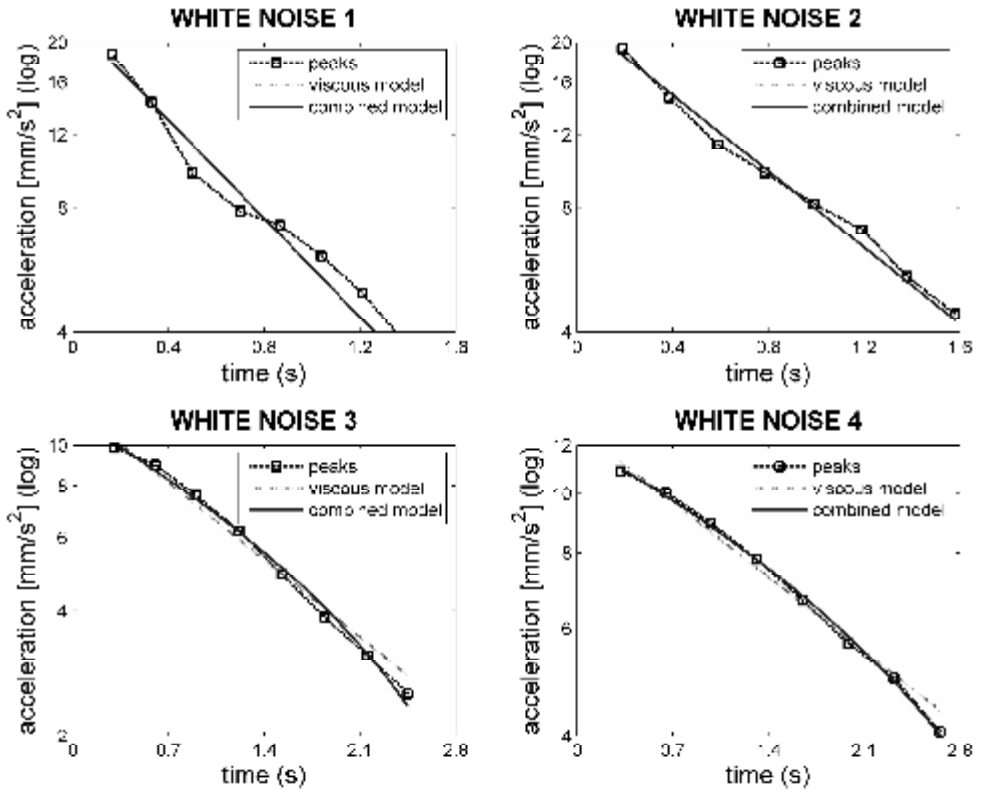


Figure 12. Fitting of the Envelopes with Two Models

Table 2 presents the damping identification results based on the two models – the purely viscous model and the viscous-friction combined model. By comparing the root mean square error (RMSE) between the identified and theoretical damping ratios as listed in the table, it is observed that the purely viscous model describes the WN-1 results better than the combined model. In contrast, for WN-3 and WN-4 in which the bridge is damaged, the combined model fits better the envelopes than the purely viscous damping model, as demonstrated from their RMSE values. Overall the viscous-friction combined model fits better with the results identified from the measurement, particularly when the bridge suffers more severe damage.

Table 2. Identified Damping Parameters and Corresponding RMSE

| | WN-1 | WN-2 | WN-3 | WN-4 |
|---|---|---|---|---|
| **Frequency (Hz)** | 2.91 | 2.53 | 1.63 | 1.51 |
| **ξ (viscous)** | 0.074 | 0.066 | 0.056 | 0.041 |
| **RMSE (viscous)** | 9.32e-4 | 5.61e-4 | 3.59e-4 | 2.82e-4 |
| **ξ (combined)** | 0.074 | 0.066 | 0.028 | 0.013 |
| **γ (combined)** | 0.000 | 0.000 | 0.014 | 0.017 |
| **RMSE (combined)** | 1.10e-3 | 6.59e-4 | 2.53e-4 | 1.46e-4 |

Figure 13 plots the identified viscous and friction damping ratios in the combined model. Recall that the four sets of white noise (ambient vibration) responses were measured at the bridge with different levels of seismic damage as shown in Table 1, with no damage in WN-1 to severe damage in WN-4. Therefore, the X-axis also represents the severity of the seismic damage. As the seismic damage becomes more severe, the viscous damping ratio $\xi$ decreases, while the frictional damping ratio $\gamma$ increases. As mentioned above, the values of $\gamma$ and $\xi$ provide information about the percentage of the total energy dissipated by each damping phenomenon. Following this interpretation it can be concluded that there is a shift of dissipated energy from a viscous mechanism (material damping) to a friction mechanism (crack damping) as the bridge column damage increases.

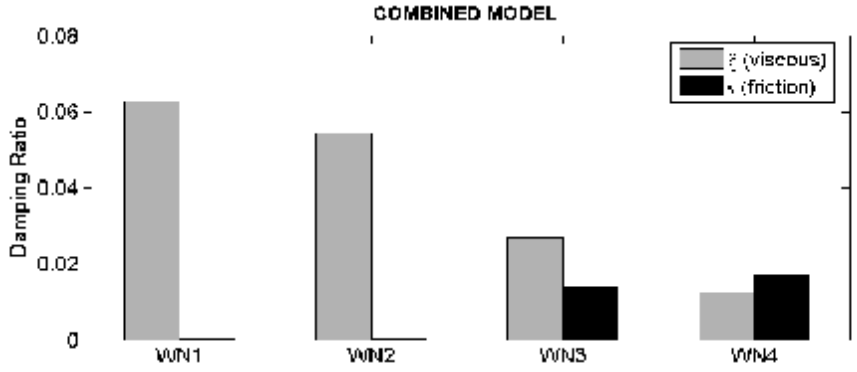


Figure 13. Comparison of Damping Parameters

The nonlinear damping parameter $\gamma$ can serve as a damage index. When its value equals zero, it means no damage. A significant advantage of this damage index is its baseline-free feature. The damage identification can be performed using only one set of post-event ambient vibration measurement without comparison with a non-damaged state. For example, if only WN-4 is measured at the bridge in the seismic shaking table tests, the bridge structure can be identified as damaged, because the value of $\gamma$ is larger than zero. Similarly, from the results of WN-1, the structure can be considered undamaged, because there is no energy dissipated by the friction mechanism.

The seismic damage identified based on the nonlinear damping analysis shown in Fig. 13 is, in general, consistent with the observed damage described in Table 1 that was based on the strain measurement at the column rebar as well as visual inspection. It is noted that at white noise 2 (WN-2), bent-1 and bent-3 already started yielding, but the nonlinear damping does not have a significant increase. For more extensive seismic damage at WN-3 and WN-4, a significant increase of the nonlinear damping is observed. The nonlinear damping parameter $\gamma$ proved to be a reliable damage index, particularly for more sever seismic damage.

In conclusion, the seismic shaking table tests successfully validated the proposed nonlinear damping method by demonstrating that the nonlinear frictional damping ratio $\gamma$, can be reliably identified from the measured bridge vibration and furthermore $\gamma$ can serve as a reliable structural damage index.

Although the nonlinear damping-based method only detects the occurrence of structural damage without being able to locate the damage, it offers many advantages including the baseline-free feature. The nonlinear damping parameter is able to detect the presence of damage in the structure without any reference to the undamaged baseline. Another advantage is that this method does not require vibration measurement with a dense array of sensors. In this study, only one sensor on top of each column was used.

# 3.4 DAMAGE DETECTION BASED ON AUTOREGRESSIVE MODEL

In addition to the nonlinear damping method, this study also developed an autoregressive (AR) model-based method for rapid damage screening based on acceleration response measurement. The AR model has been widely used in statistical analysis of time history data, and it is potentially useful in the representation of certain practically occurring time series, such as structural damage caused by a destructive event. The effectiveness of this method in rapidly detecting the occurrence of seismic damage on a concrete bridge has been demonstrated through the seismic shaking table tests.

## 3.4.1 Autoregressive Model

The proposed damage detection method is based on the identification of AR coefficients in the AR model of a structure. The AR model predicts responses of the structure using measured signals from sensors. According to the definition of the AR model as shown in Eq.22, the current value of a time series data is expressed as a finite linear combination of previous values of the time series data and a random error.

$$y_t = a_1 y_{t-1} + a_2 y_{t-2} \mathbf{L} + a_p y_{t-p} + e_t \qquad (22)$$

Where $y_t, y_{t-1}, \mathbf{L}$ denote the values of a time series data at equally discretized times $t, t-1, \mathbf{L}$ , $a_1, a_2, \mathbf{L}$ are coefficients of autoregressive model and $e_t$ is a random error of time series data at time *t*. The random error $e_t$ means probabilistic error which cannot be explained by this model, such as measurement error. The mean of the time series data should be zero because the expectation of the random error is zero. In case of a nonzero mean, the autoregressive model of order *p* should be modified as shown in Eq. 23.

$$[y_t - m] = a_1[y_{t-1} - m] + a_2[y_{t-2} - m]\mathbf{L} + a_p[y_{t-p} - m] + e_t \qquad (23)$$

There are several methods to calculate coefficients of the autoregressive model such as least squared method, moment method, maximum likelihood, Bayesian theory and so on. Because of its simplicity and clarity, the least squared method is selected to estimate the coefficients of the autoregressive model. The predicted value from the autoregressive model of order *p* can be stated as follows.

$$\tilde{y}_t = a_1 y_{t-1} + a_2 y_{t-2} + \mathbf{L} + a_p y_{t-p} = \sum_{m=1}^{p} a_m y_{t-m} \qquad (24)$$

The residuals can be defined as the difference between measured and predicted values using the autoregressive model at each time step.

$$e_t = y_t - \tilde{y}_t = y_t - \sum_{m=1}^{p} a_m y_{t-m} \quad (t \geq p+1) \qquad (25)$$

The residuals contain unknown signals $y_{1-p}, \mathbf{L}, y_0$, the reason why the residual can be defined after *p*+1. The residuals of total number of measured signals can be rewritten in a matrix form for simplicity.

$$\mathbf{e} = \begin{pmatrix} e_{p+1} \\ e_{p+2} \\ \mathbb{M} \\ e_N \end{pmatrix} = \begin{pmatrix} y_{p+1} \\ y_{p+2} \\ \mathbb{M} \\ y_N \end{pmatrix} - \begin{bmatrix} y_p & y_{p-1} & \mathbf{L} & y_1 \\ y_{p+1} & y_p & \mathbf{L} & y_2 \\ \mathbb{M} & \mathbb{M} & \mathbf{O} & \mathbb{M} \\ y_{N-1} & y_{N-2} & \mathbf{L} & y_{N-p} \end{bmatrix} \begin{pmatrix} a_1 \\ a_2 \\ \mathbb{M} \\ a_p \end{pmatrix} = \mathbf{Y} - \mathbf{Qa} \qquad (26)$$

Where *N* represents total number of measured signals.

The minimization problem by the least squared method is represented in Eq. 27.

$$\underset{\mathbf{a}}{\text{Min}}\,\Pi_E = \frac{1}{2}\mathbf{e}^T \cdot \mathbf{e} = \frac{1}{2}(\mathbf{Y}-\mathbf{Q}\mathbf{a})^T(\mathbf{Y}-\mathbf{Q}\mathbf{a}) \tag{27}$$

The optimal solution of **a** can be obtained from the first order necessary condition of Eq. 27.

$$\frac{\partial \Pi_E}{\partial \mathbf{a}} = \mathbf{Q}^T\mathbf{Q}\mathbf{a} - \mathbf{Q}^T\mathbf{Y} = 0 \quad \Rightarrow \quad \mathbf{a} = (\mathbf{Q}^T\mathbf{Q})^{-1}\mathbf{Q}^T\mathbf{Y} \tag{28}$$

The autoregressive coefficients estimated by minimizing the least squared errors generally tend to be unstable because of sparseness of data, environmental interference, measurement noise and so on. So a regularization technique, the regularized least square estimator, as shown in Eq. 29, was adopted to alleviate instability of autoregressive coefficients (Park et al., 2001). The regularization function is added to the error function.

$$\underset{\mathbf{a}}{\text{Min}}\,\Pi(t) = \frac{1}{2}\mathbf{e}_t^T \cdot \mathbf{e}_t + \frac{b^2}{2}\left\|\mathbf{a}_t - \bar{\mathbf{a}}_t\right\|_2^2 = \frac{1}{2}(\mathbf{Y}_t - \mathbf{Q}_t\mathbf{a}_t)^T(\mathbf{Y}_t - \mathbf{Q}_t\mathbf{a}_t) + \frac{b^2}{2}\left\|\mathbf{a}_t - \bar{\mathbf{a}}_t\right\|_2^2 \tag{29}$$

Where $\bar{a}_t$ represent the mean value of the autoregressive coefficients vector up to current time step and $b$ represents regularization factor. The final solution with the regularization technique can be obtained by minimizing the least square estimator, as shown in Eq. 30.

$$\mathbf{a}_t = (\mathbf{Q}_t^T\mathbf{Q}_t + b^2\mathbf{I})^{-1}(\mathbf{Q}_t^T\mathbf{Y}_t + b^2\bar{\mathbf{a}}_t) \tag{30}$$

The regularization factor has a critical effect on the stability of the solution. The optimal regularization factor is determined by the geometric mean scheme shown below.

$$b = \sqrt{S_{\max} \cdot S_{\min}} \tag{31}$$

Where $S_{\max}$ , $S_{\min}$ represent a maximum and minimum singular value obtained from singular value decomposition of system matrix $\mathbf{Q}_t$.

### 3.4.2 Damage Index

An ideal damage index is capable of distinguishing damaged and undamaged states. For example, an ideal damage index would indicate 1 for a damaged state and 0 for the undamaged state, without any value in between and any possibility of false warning or damage missing.

There are two possible damage features in damage detection using the AR model (Sohn et al., 2000, Sohn et al., 2001, Zhang, 2007). One is the residual and the other is the autoregressive coefficient. The residual has good characteristic that is highly stable and sensitive to both amplitude and frequency change of measured data, but it is difficult to identify the source of changes. The AR coefficients are the system parameter of the AR model, and they are sensitive to frequency change and insensitive to amplitude change, but they generally suffer from ill-posedness in minimizing the least squared errors.

When structural damage occurs, both the residual and the AR coefficients vary abruptly at the damage instance. Abnormality in the residual lasts for about two times the order of an AR model, while abnormality in the AR coefficients last for the time window size. In a pseudo damaged situation, both residual and AR coefficients also vary abruptly at the damage instance. But the abnormality in the residual and AR coefficients disappear very quickly within one or two time steps. So the key idea of a noble damage index is that damage can be identified clearly by considering the duration of the abnormal values in the residual and AR coefficients.

Aiming to making use of information on both residuals and AR coefficients instantaneously, a new damage index is proposed in this study. The proposed damage index is a covariance-like variable between the residuals and AR coefficients, as shown in Eq. 32. The absolute value of the residuals and AR coefficients are used because the directional information of damage index is not necessary.

$$
\begin{aligned}
& e = (e_{t-n_w\Delta t}, \mathbf{L}, e_{t-\Delta t}, e_t), \quad a = (a_{t-n_w\Delta t}, \mathbf{L}, a_{t-\Delta t}, a_t) \\
& D_t = E(|e-\bar{e}||a-\bar{a}|) = \frac{1}{n_w+1}\sum_{k=0}^{n_w}|e_{t-k\Delta t}-\bar{e}_0||a_{t-k\Delta t}-\bar{a}_0| \\
& \bar{e}_0 = \frac{1}{N(t)}\sum_{k=0}^{N(t)} e_{t-k\Delta t}, \quad \bar{a}_0 = \frac{1}{N(t)}\sum_{k=0}^{N(t)} a_{t-k\Delta t}
\end{aligned} \tag{32}
$$

$N(t)$ : Total number of time steps from $t=0$

### 3.4.3 Damage Detection

This study further develops the AR model into a baseline-free damage detection algorithm. It is proposed to detect structural damage solely based on the analysis of the measured structural responses and their relative discrepancies during an event. A bilinear fitting method (BFM) is utilized to detect damage in the process (Park et al., 2007a). BFM is originally proposed to determine the optimal truncation number in system identification problems. BFM is an approach to determine the critical value that separates a physical state from others by discretely measured or calculated physical quantities as shown in Figure 14.

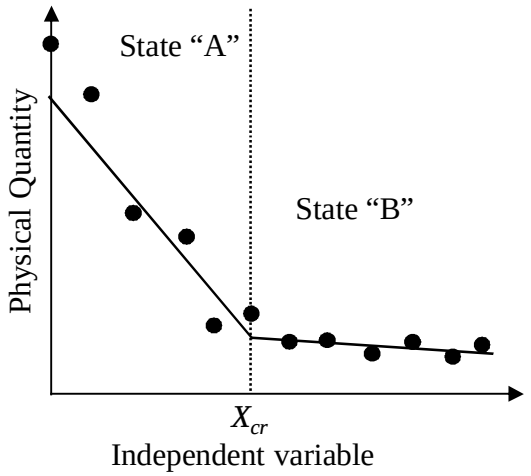


Figure 14 Schematics of Bilinear Fitting Method

The computed damage index should be rearranged in the descending order shown in Eq. 14.

$$D_{\max} = D_1 \geq D_2 \geq \mathbf{L} \geq D_{nd} = D_{\min} \tag{33}$$

Where $D$ represents a damage index and $nd$ represents the total number of the damage index. A discrete partial variance function (DPVF) can be defined as shown in Eq. 34.

$$\begin{aligned} q_k &= \frac{1}{nd-k+1}\sum_{i=k}^{nd}(D_i - D_{avg})^2 \quad \text{for } k = 1, \mathbf{L}, nd \\ D_{avg} &= \frac{1}{nd-k+1}\sum_{i=k}^{nd} D_i \end{aligned} \tag{34}$$

If there is no damage on the targeted structure, no large value of the damage index exist since the system parameters in the structure are not altered during an event. Taking out damage indices from lager values sequentially, the DPVF decreases gradually, and can be represented by a single line as shown in Fig. 15.

On the contrary, if the structure suffered damage, two groups of damage indices exist since the system parameters change during an event. One group is associated with larger damage indices and the other with smaller ones. As the larger damage indices in the first group are removed sequentially, the DPVF decreases rapidly for the first group. The slope of DPVF suddenly becomes mild when all damage indices for the damage instants are excluded in DPVF, as shown in Fig. 16.

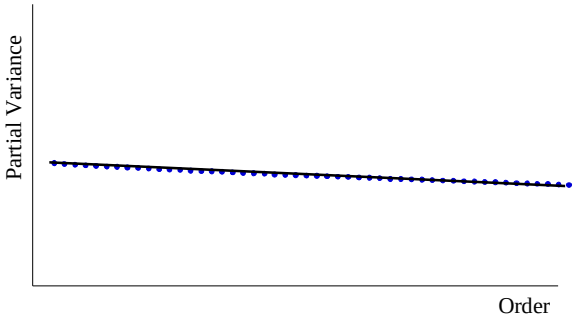


Figure 15 DPVF in Undamaged Case

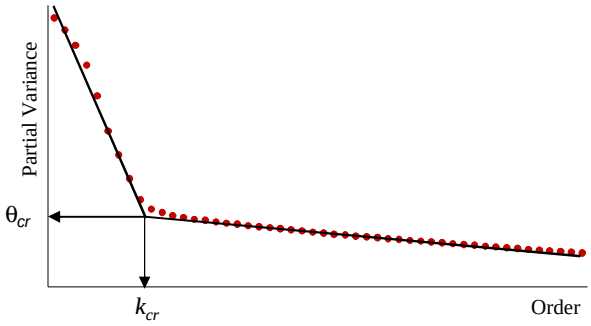


Figure 16 DPVF in Damaged Case

The optimal bilinear function can be obtained by minimizing the least squared error between the measured and the estimated DPVF as shown in Figure 17, in which $k_b$ represents the optimal truncation number to separate the damaged state from undamaged state and $q_{cr}$ represents the threshold value of the partial variance, related to the threshold value of the real damage index. The minimization is performed in the logarithmic scale to detect minor or relatively insensitive damage.

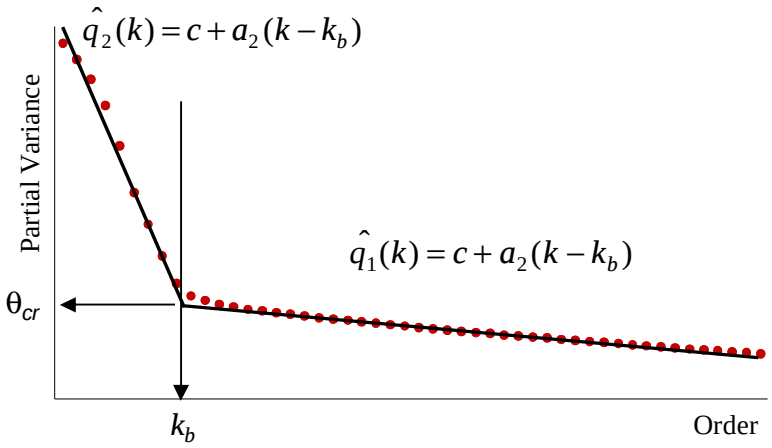


Figure 17 Minimization of Least Squared Error in BFM

Furthermore, an integrated decision making procedure is developed in this study to enhance the reliability of damage detection. The integration of individual decisions based on data from individual sensors is very important for accurately assessing the state of the structure. Even if only one sensor indicates damage, the target structure can be actually damaged. So the final decision on the structure should be made by "or" condition based on individual decisions from data of each sensor.

$$D_t^I = \frac{1}{n_s}\sum_{i=1}^{n_s} D_t^i \tag{35}$$

Data from each sensor have a different sensitivity to damage, but the damage state of the structure should be determined based on the relative magnitude of the damage index to the critical value. Therefore the damage index should be normalized by its own critical value. A bilinear fitting index can be categorized into two cases as shown in Eq. 36.

$$D_t^I = \frac{1}{n_s}\sum_{i=1}^{n_s} D_t^i / D_{cr}^i \tag{36}$$

Where $q_{\max}$ , $q_0$ represents the maximum value and the minimum value of the partial variance of the first group which include damage index of a damaged state such as in Fig. 18.

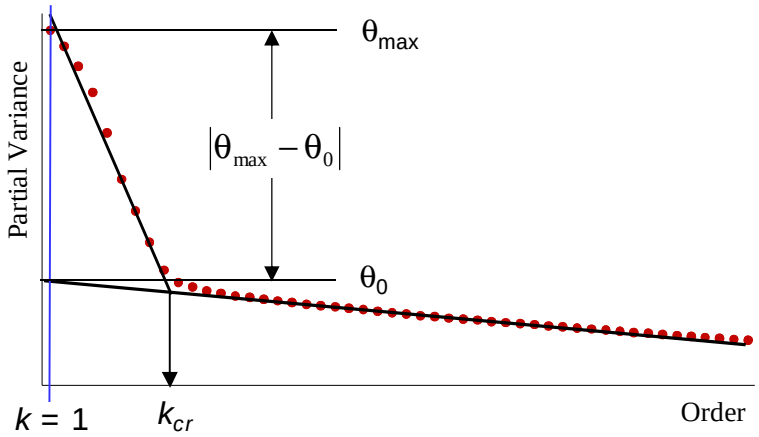


Figure 18 Bilinear Fitting Index

The final integrated decision is made by the weighted form as shown in Eq. 37.

$$D_t^I = \sum_{i=1}^{n_s} W^i D_t^i / D_{cr}^i \quad \text{where} \quad W^i = w_q^i / \sum_{m=1}^{n_s} w_q^m \tag{37}$$

Any false warnings issued by sensors with damage indices slightly larger than the critical value can be suppressed by the weighted decision shown in Eq. 37.

### 3.3.4 Validation by Seismic Shaking Tables Tests

The proposed post-event damage screening based on the baseline-free AR model algorithm is validated through the seismic shaking table tests of a large three two-column bent concrete bridge model. As described in Section 3.2, the bridge model was subjected to a series of low to high amplitude earthquakes, inducing progressive seismic damage to the structure.

The objective is to demonstrate that the integrated damage index shown in Eq. 37 can be reliably identified from the measured bridge seismic response and furthermore can serve as a reliable structural damage index by comparing the index with the structural damage observed by visual inspection and by the embedded strain sensors (as presented in Table 1).

Figures 19 through 22 present the damage detection results based on sensor data measured at channel 4 during seismic shaking tests T-12 through T-15, respectively. The result for T-12 shows no damage to the structure and the results for T-14 and T-15 clearly indicate structural damage. These are consistent with the experimental observations by both visual inspection and strain measurement (as shown in Table 2). However, the results for T-13 do not clearly indicate structural damage.

On the other hand, Figures 23 through 26 show integrated decision results based on multiple measured data from multiple sensors for the same seismic shaking tests T-12 through T-15. It is noted that peaks in the initial time period in these figures are due to the numerical instability. From these figures, the seismic damage during T-14 and T-15 can be clearly detected. However, the damage (yielding of Bent-1, as confirmed by the strain measurement) during T-13 is not detected.

In general, the damage detection results by the proposed AR method are consistent with the seismic damage measured by the embedded strain sensors and by visual inspection,

particularly for more severe seismic damage. In conclusion, the seismic shaking table test results validated the proposed AR method with the integrated decision index shown in Eq. 37.

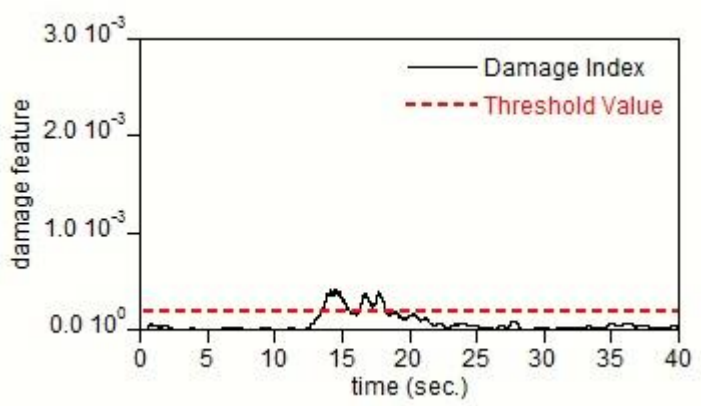


Figure 19 Damage Detection Results Based on Ch-4 Data – T-12

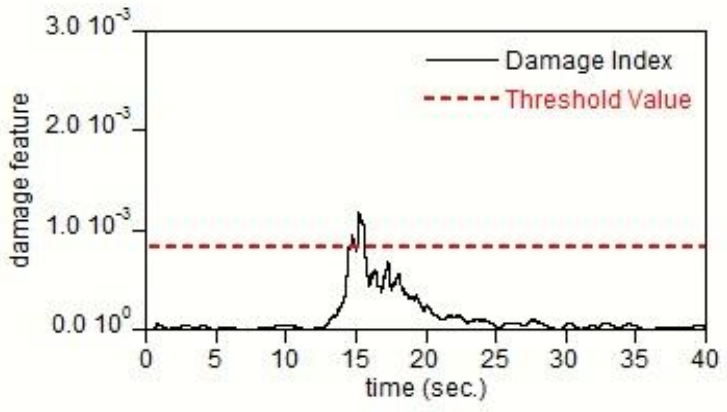


Figure 20 Damage Detection Results Based on Ch-4 Data - T-13

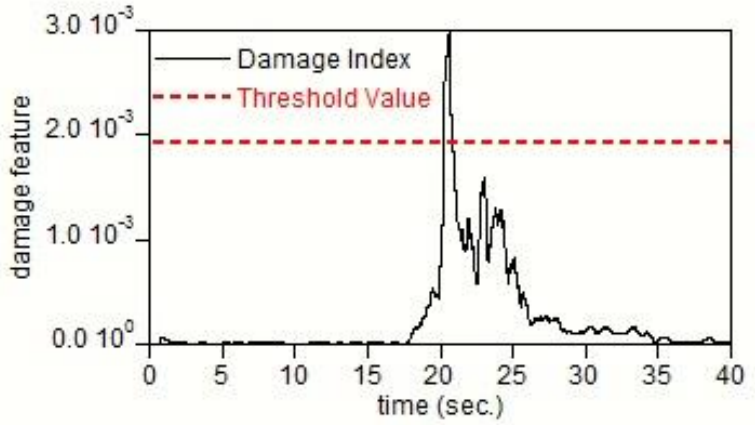


Figure 21 Damage Detection Results Based on Ch-4 Data - T-14

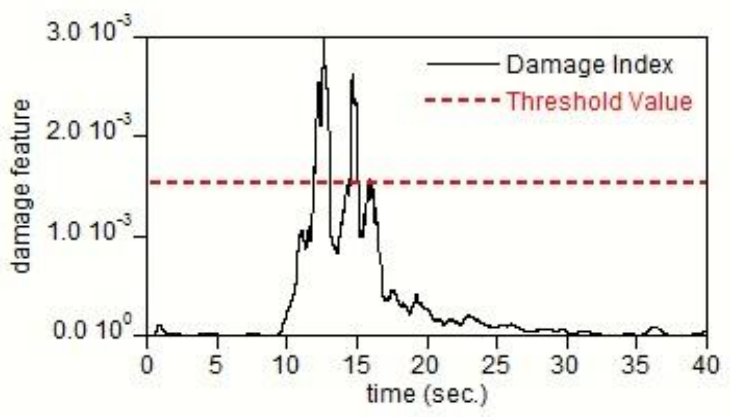


Figure 22 Damage Detection Based on Ch-4 Data - T-15

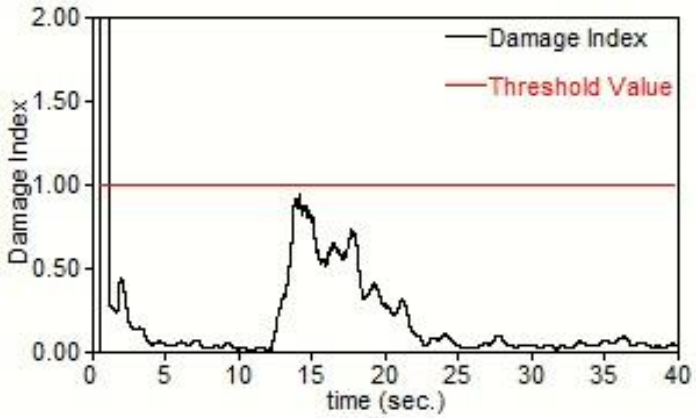


Figure 23 Integrated Damage Detection - T-12

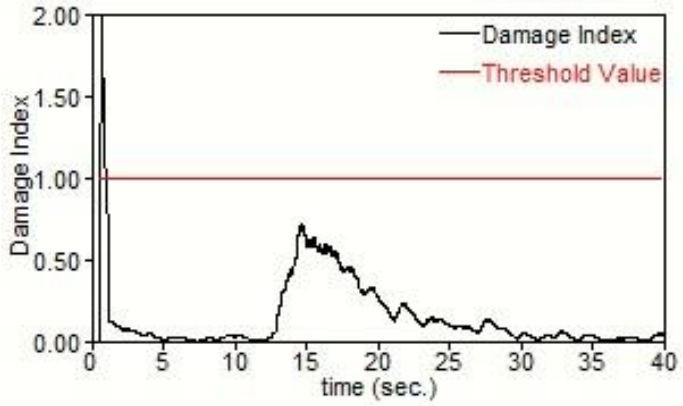


Figure 24 Integrated Damage Detection - T-13

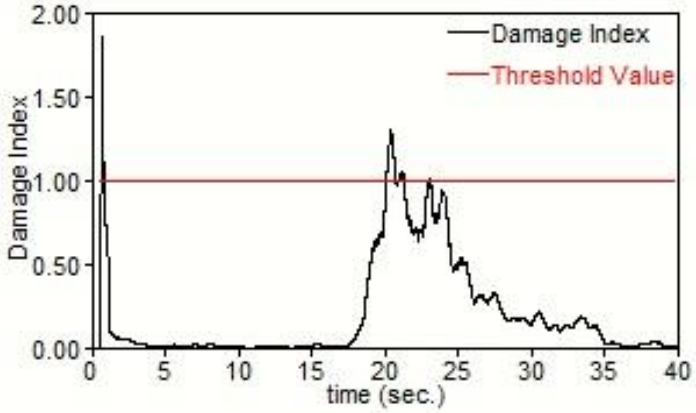


Figure 25 Integrated Damage Detection - T-14

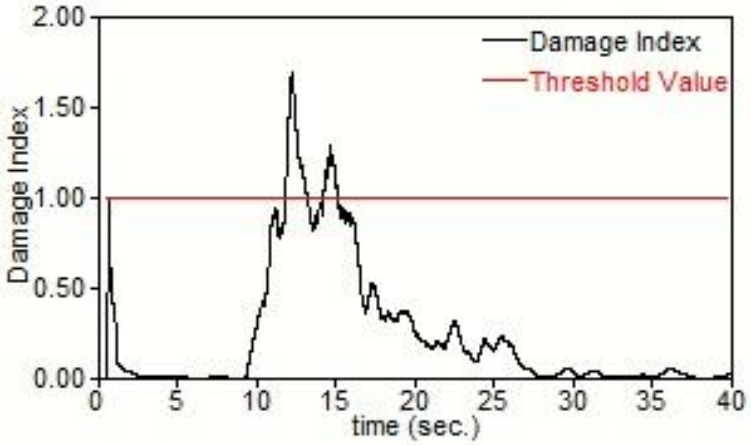


Figure 26 Integrated Damage Detection - T-15

## 3.5 DAMAGE ASSESSMENT BASED ON EXTENDED KALMAN FILTER

The goal of a more detailed post-event damage assessment is to determine not only whether structural damage has occurred, but also the location and extent of such damage. In order to achieve this goal, it is proposed to identify the change of stiffness of structural elements based on the analysis of dynamic responses of a structure. Post-event structural damage causes the change in the stiffness of structural elements. By identifying the structural elements whose stiffness values have been degraded, the damage locations can be determine.

Reinforced concrete bridges, a focus of this project, exhibit significant hysteresis behaviors when subjected to strong earthquakes or other events causing large cyclic deformations. Hysteresis is not only a highly nonlinear phenomenon, but also a process that possesses memory. Recently, considerable efforts in the structural health monitoring research community have been endeavored to track the structural conditions (e.g. the instantaneous stiffness and damping at every instance), by identifying the hysteresis from global vibration measurements during a strong cyclic deformation. This has been found a highly challenging problem because of the nonlinearity of the system and the dependency of the current nonlinearity on previous deformation conditions.

In this project, a time-domain extended Kalman filter method has been developed, which is capable of identifying parameters of nonlinear systems. The Kalman filtering technique uses not only the measurement data in a probabilistic sense but also information from structural models so that identification becomes possible even under noise contaminated measurements and for uncertain models (Kalman, 1960). Results obtained by an extended Kalman filter approach from simulated data with known damage scenarios were reported (e.g., Yun and Shinozuka, 1980; Hoshiya and Saito, 1984; Loh and Chung, 1993; Loh and

Tou, 1995; Yang et al, 2005). The extended Kalman filtering method is applied in this study to assess seismic damage by instantaneously identifying changes in elemental stiffness values of a bridge structure during a seismic event based on seismic response measurement. The seismic response data collected from the large-scale shaking table test of a three-bent concrete bridge model are used to validate this method.

### 3.4.2 Extended Kalman Filter for Instantaneous Stiffness Identification

The extended Kalman filter formulation for structural damage assessment can be summarized as follows.

A second order equation of motion for a multi degree of freedom system can be written

$$M.\ddot{u}(t) + C(t).\dot{u}(t) + K(t).u(t) = -M.I.\ddot{u}_g \tag{38}$$

Where $M$ is the mass matrix, $C(t)$ is the time varying damping matrix, $K(t)$ is the time varying stiffness matrix, $u$ is the relative displacement vector, $I$ is the influence vector and $\ddot{u}_g$ is the input ground acceleration. $\ddot{u}+\ddot{u}_g$ and $\ddot{u}_g$ are measured, $M$ is calculated from the structural design drawings, $C(t)$ is considered to be of Rayleigh type damping, i.e. linear combination of $K(t)$ and $M$ matrices. The objective is to identify $K(t)$, which is directly used as the damage indicator.

An extended state vector is defined as:

$$x(t) = [u(t), \dot{u}(t), \Psi(t)]^{\mathrm{T}} \tag{39}$$

Where $\Psi(t)$ is the extended state. In this study it is the stiffness values for the structural elements to be identified.

The extended Kalman filter determines the optimal estimate of the state $\hat{x}_{k|k}$ that minimizes the trace of the error covariance

$$P_{k|k} = E[(x_k - \hat{x}_{k|k})(x_k - \hat{x}_{k|k})^{\mathrm{T}}] \tag{40}$$

Where ^ denotes estimation.

There are mainly two conceptual phases in the extended Kalman filter, namely the prediction and correction phases. In the prediction phase, state estimate and the error covariance $P_{k-1|k-1}$ are projected ahead in time resulting in a-priori estimates of $\hat{x}_{k|k-1}$ and $P_{k|k-1}$. In the correction phase these a-priori estimates are filtered using the information from the new measurements resulting in a-posteriori estimate $\hat{x}_{k|k}$ and $P_{k|k}$.

The system can be defined as:

$$\dot{x}(t) = f(x,t) + w(t) \tag{41}$$

Where $w(t)$ is process noise.

$$y(t) = h(x,t) + v(t) \tag{42}$$

Where $y(t)$ is the measurement and $v(t)$ is the measurement noise.

The system is supposed to meet the conditions below:

$$E[w(t)] = 0 \tag{43}$$

$$E[v_k] = 0 \tag{44}$$

$$E\left[w(t)v_k^T\right] = 0 \tag{45}$$

Where subscript *k* indicates discrete time.

The values of $Q$, $R$, $x_0$, $P_0$ are defined as:

$$E[w(t)w^{\mathrm{T}}(t)] = Q_c(t) \tag{46}$$

$$E\left[v_j v_k^T\right] = R_k d_{jk} \tag{47}$$

$$E[x(t_0)] = x_0 \tag{48}$$

$$E[(x(t_0) - x_0)(x(t_0) - x_0)^{\mathrm{T}}] = P_0 \tag{49}$$

Where subscript *c* indicates continuous time and *j* indicates discrete time.

Linearized measurement matrix $H_k$ (for steps 3, 4 & 5 below) can be obtained as:

$$H(x,t) = \frac{\partial h(x,t)}{\partial x} \tag{50}$$

$$H_k = H(\hat{x}_{k|k-1}, t_k) \tag{51}$$

Linearized state matrix $F_k$ (for calculating the state transition matrix) can be obtained as:

$$F(x,t) = \frac{\partial f(x,t)}{\partial x} \tag{52}$$

$$F_k = F(\hat{x}_{k|k-1}, t_k) \tag{53}$$

State transition matrix $\Phi_{k-1}$ can be obtained (for step 1) as:

$$\Phi_{k-1} = I + \int_{t_{k-1}}^{t_k} F(\ddot{x}_{t|k-1}, t)\Phi(t, t_{k-1})dt \tag{54}$$

The last equation is written as:

$$\Phi(t_k, t_{k-1}) = \exp(\Delta t.F_{k-1}) \qquad \text{Constant } F \forall t \in [t_{k-1}, t_k) \tag{55}$$

This is approximated as:

$$\Phi(t_k, t_{k-1}) = I + \Delta t.F_{k-1} \tag{56}$$

Also the process noise can be discretized as:

$$Q_{k-1} = \Delta t.Q_c(t_{k-1}) \tag{57}$$

After initializing $Q$, $R$, $x_0$, $P_0$, Kalman filtering can be performed in the following five steps:

Step 1: Predicting Covariance:

$$P_{k|k-1} = \Phi_{k-1}P_{k-1|k-1}\Phi_{k-1}^T + Q_{k-1} \tag{58}$$

Step 2: Predicting State:

$$\hat{x}_{k|k-1} = \Phi_{k-1}\hat{x}_{k-1|k-1} \tag{59}$$

Step 3: Computing Kalman Gain:

$$G_k = P_{k|k-1}H_k^{\mathrm{T}}(H_k P_{k|k-1}H_k^{\mathrm{T}} + R_k)^{-1} \tag{60}$$

Step 4: Correcting Covariance:

$$P_{k|k} = (I - G_k H_k)P_{k|k-1} \tag{61}$$

Step 5: Correcting State:

$$\hat{x}_{k|k} = \hat{x}_{k|k-1} + G_k[y_k - H_k \hat{x}_{k|k-1}] \tag{62}$$

Therefore, state vector $x$ is obtained at each time step. As described in Eq. 39, the state vector contains information of not only displacement and velocity but also of the stiffness value. This means that the stiffness value is identified for each time step.

### 3.5.2 Validation by Seismic Shaking Table Tests

The extended Kalman filter method was validated by the seismic shaking table tests. As presented in Section 3.2, the bridge model was subjected to a series of low to high amplitude earthquakes, inducing progressive seismic damage to the structure.

The objective is to demonstrate that the stiffness of the bridge columns can be instantaneously identified by processing the measured seismic response data online, and the change of the stiffness pre- and post-earthquake can be reliably linked to the structural damage observed by visual inspection and by the embedded strain sensors (as presented in Table 1).

It is noted that the extended Kalman filter method is applicable to nonlinear as well as linear responses, which is a significant advantage. Stiffness values in the damaged zones are considered as piecewise linear within each time step. However they are updated at each time step, so that the nonlinearity of the stiffness is taken into consideration. These identified stiffness values at each time step are referred to as instantaneous stiffness values. At each time step, the state transition matrix in Eq. 35 is obtained analytically from a finite element model of the bridge, each of the five steps of EKF show in Eqs. 58 through 62 is implemented, the structural stiffness is corrected after Eq. 62, and the new Jacobian matrix,

Eq. 52 and 53 (which is used for state transition matrix) is calculated again. So at the end of the seismic input motion, the structural stiffness value at assigned locations can be obtained.

Figure 27 shows the time histories of the instantaneously identified stiffness values at different plastic hinge locations of the bridge columns during seismic excitation T-13. The stiffness value is presented by the ratio of the identified stiffness versus the stiffness before damage. From the time history plots of the stiffness ratio, it is obvious that the lower plastic hinges of Bent-1 and Bent-3 suffered more than 20% stiffness degradation.

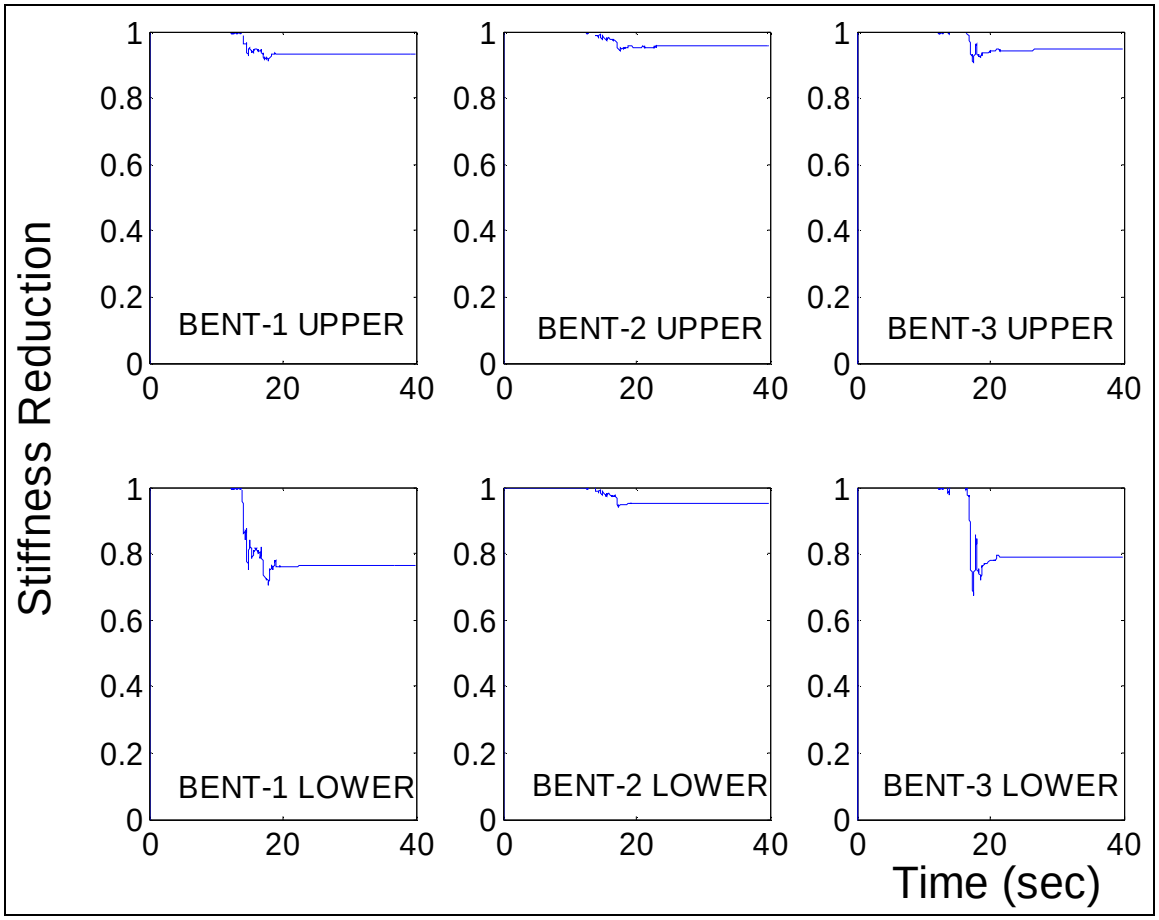


Figure 27 Instantaniesly Identified Stiffess at Different locations during T-13

Figure 27 compares the time histories of the response acceleration at the top of bent-2 to seismic excitation T-13 measured by the accelerometer and predicted by the extended Kalman filter method. An excellent agreement between the measured and simulated response accelerations is observed in the figure. The agreement confirms the accuracy of the identified instantaneous stiffness values during event T-13.

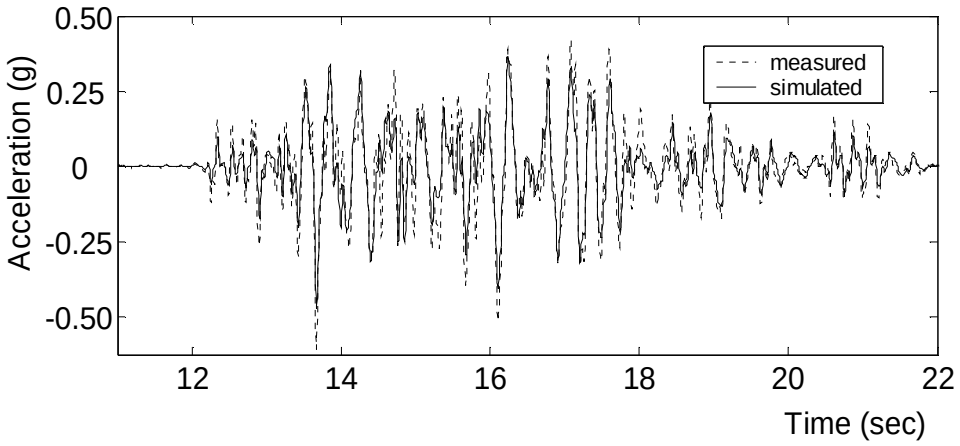


Figure 28 Comparison of Measured and Simulated Responses to Event T-13

Similarly, the instantaneous stiffness values, identified at each time step, during the T-14, T-15 and T-19 seismic excitations are shown in Figs. 27 through 31 respectively. From Fig. 29, significant degradation of the stiffness at the lower portions of bent-1 and bent-3 is observed. From Fig. 30, bent-2 suffered, for the first time, stiffness degradation during event T-15. This is, in general, consistent with the damage observed by the strain measurement and visual inspection, as described in Table 2. Furthermore, the agreement between measured and simulated acceleration responses during T-19, as shown in Fig. 32, confirms the accuracy of these instantaneously identified stiffness values.

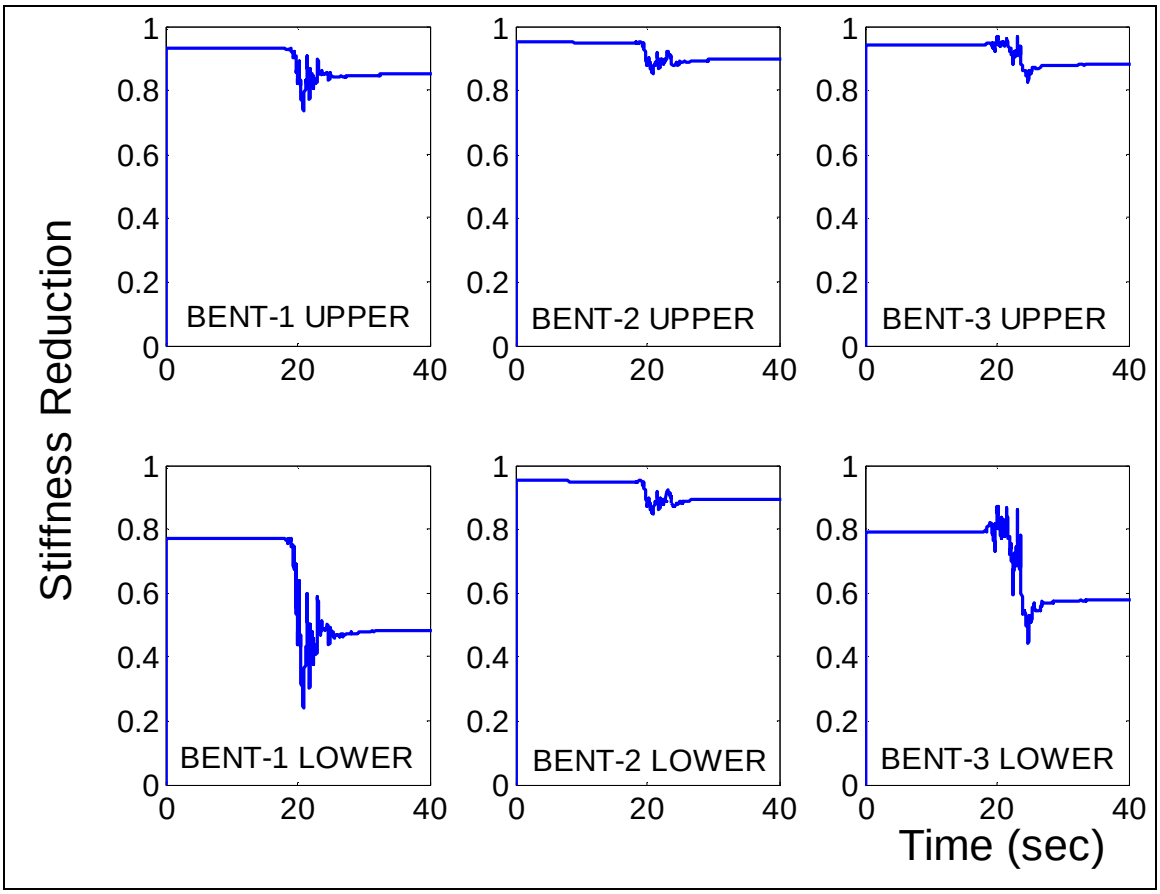


Figure 29 Instantaniesly Identified Stiffess at Different locations during T-14

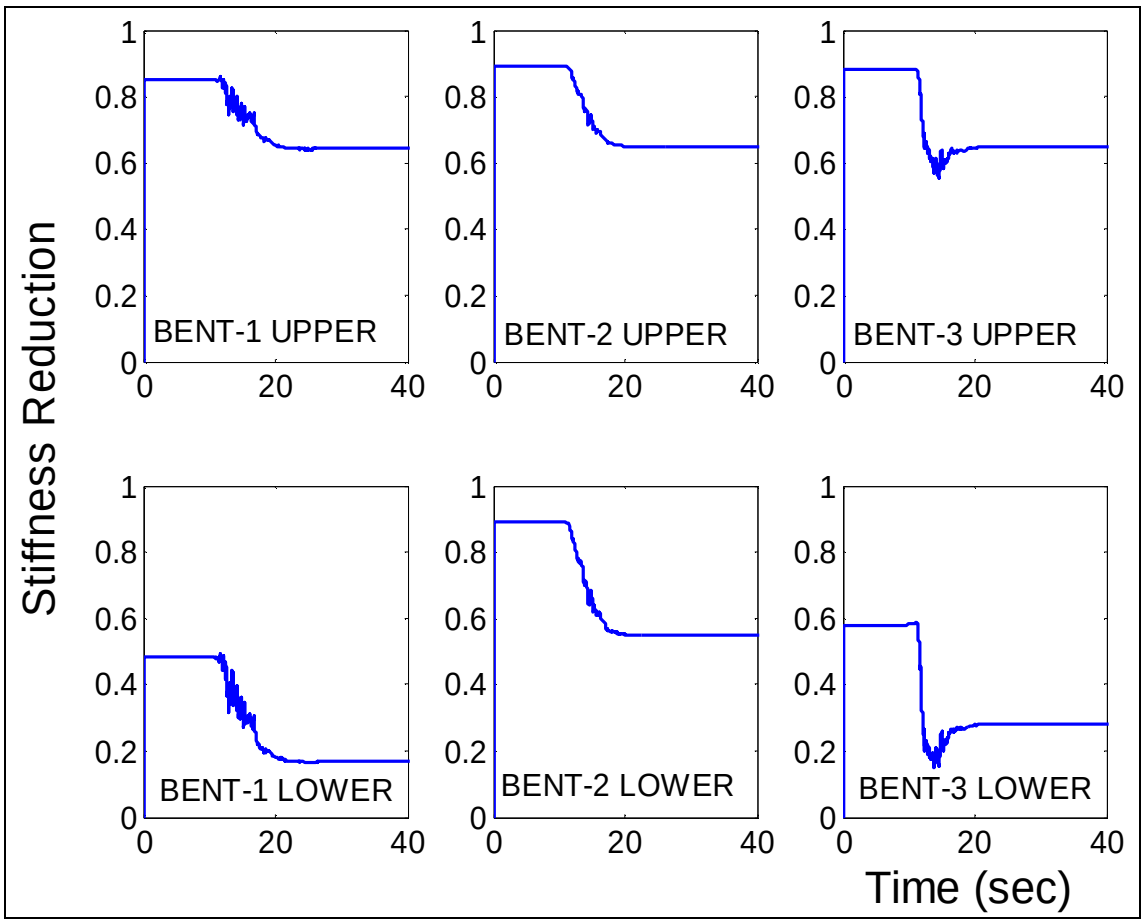


Figure 30 Instantaniesly Identified Stiffess at Different locations during T-15

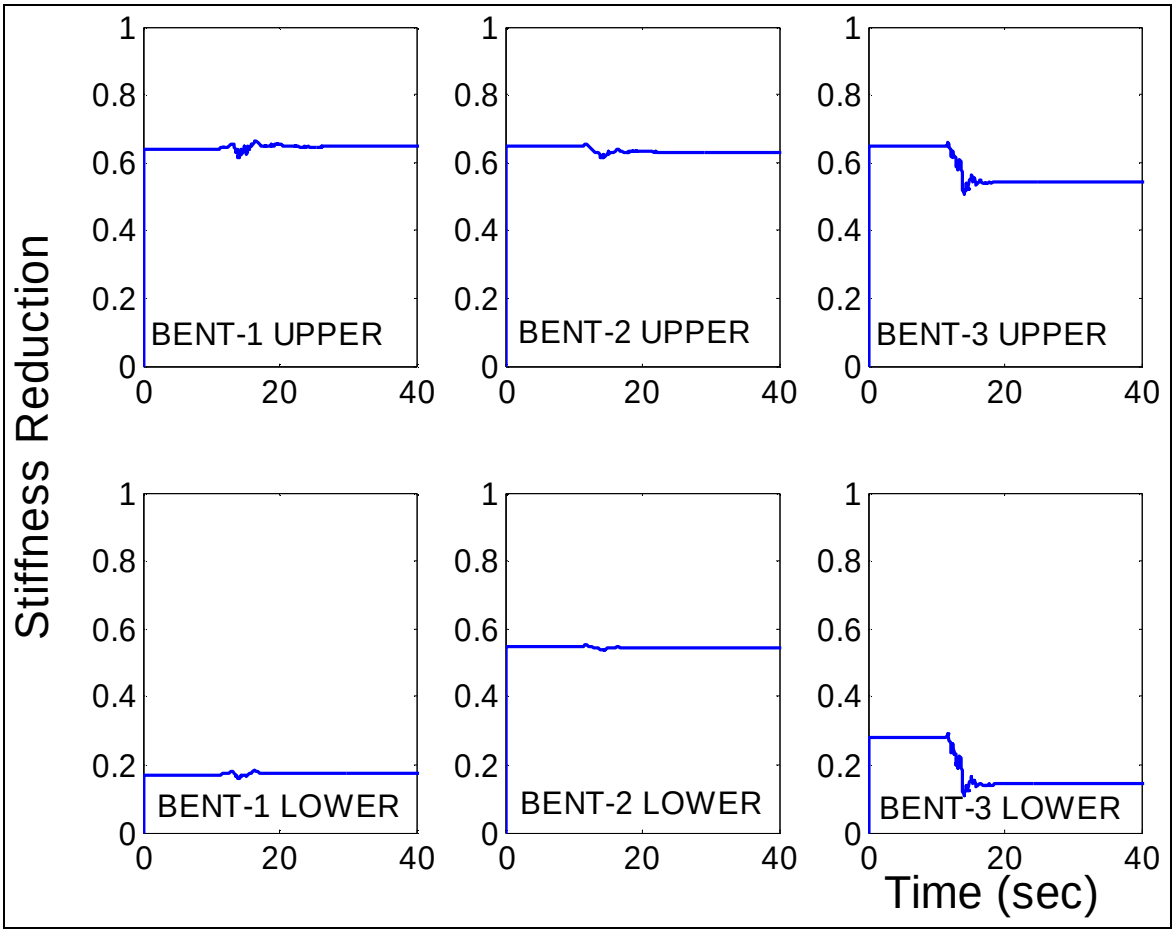


Figure 31 Instantaniesly Identified Stiffess at Different locations during T-16

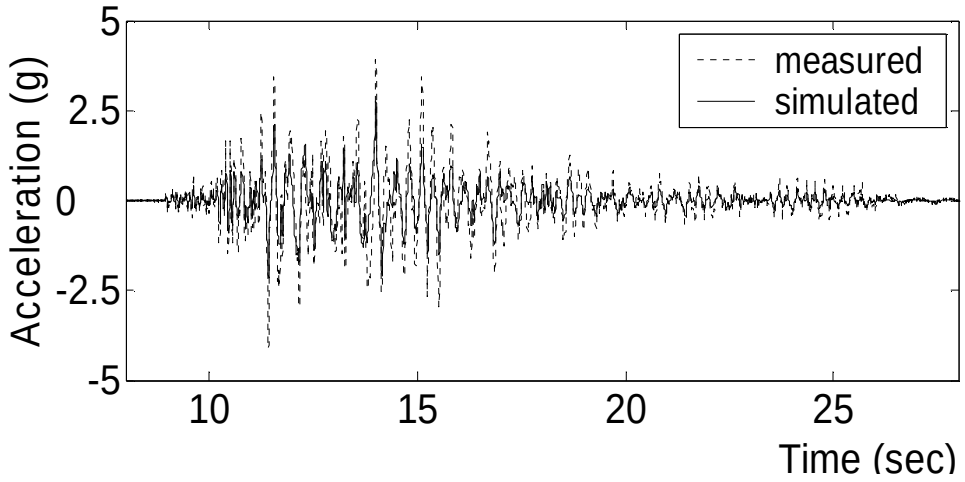


Figure 32 Comparison of Measured and Simulated Responses to Event T-19

In conclusion, the extended Kalman filter method is experimentally validated by the seismic shaking table tests. Using the response acceleration measurement during each earthquake, elemental stiffness values at the upper and lower plastic hinge locations of the bridge columns were instantaneously identified by the extended Kalman filter method, in which the unknown stiffness constitutes the extended states of the Kalman filter. The identified stiffness degradation at different locations of the bridge columns is consistent with the damage observed by the strain gauge measurement and visual inspection.

The identification results also demonstrate the capability of the proposed damage assessment method for identifying invisible damage. Although after the T-13 and T-14 earthquakes, no apparent damage is visible (see Fig. 4), stiffness degradation was identified on bent-1 and bent-3.

The extended Kalman filter method has the following advantages: (1) it does not require an undamaged baseline model of the bridge, (2) it can locate and quantify the damage as well as detect the damage, and (3) the stiffness identification is performed online in real time, without requiring post-processing.

# 3.6 DAMAGE ASSESSMENT BASED ON QUASI-NEWTON OPTIMIZATION

This method detects, locates and quantifies post-event damage of a structure by identifying change of structural stiffness based on a parameter optimization routine using low-amplitude pre- and post-event vibration data. A structure, particularly a concrete structure, experiencing a damaging event, exhibits significant hysteresis behaviors and thus is a nonlinear system. However, the same structure experiencing low-amplitude ambient vibration pre and post the event can be modeled as a linear and time-invariant (LTI) system, which significantly eases the identification of structural properties. Compared with the extended Kalman filter method described in Section 3.5 that instantaneously identify the change of structural stiffness during an event, a simpler method is developed in this section that focuses on the post-event structural stiffness with respect to the pre-event stiffness using low-amplitude vibration data, by treating the structure as an LTI system.

## 3.6.1 Optimization-Based Parameter Identification

In this subsection, an optimization method for identifying structural stiffness and damping is outlined. This model-based parametric method utilizes global optimization to identify the stiffness and damping that reconcile the predicted and measured vibration characteristics (i.e., frequencies and mode shapes, Method 1) or response time histories (Method 2). The system model is assumed as LTI, and the identification is relatively easy to implement by quasi-Newton optimization routines.

**Model parameterization: sectional stiffness correction coefficients**

Actual sectional stiffness is represented by a set of correction coefficients, $\beta_i$'s , being a fraction of the sectional stiffness calculated from drawings. To be specific,

$$\beta_i = \frac{(k)_A}{(k)_D}, \tag{63}$$

Where $(k)_A$ is the actual (subscript *A*) sectional stiffness of Element *i*, and $(k)_D$ is the sectional stiffness of the same element calculated from drawings (subscript *D*). Sectional stiffness *k* can be either *EI* for bending stiffness or *EA* for axial stiffness of an element, depending on the applications.

Rayleigh type damping was assumed in this study for all the models. A Rayleigh damping matrix **C** is a linear combination of the mass and stiffness matrices **M** and **K**, by

$$\mathbf{C} = a\mathbf{M} + b\mathbf{K}. \tag{64}$$

Two correction coefficients, $\alpha_i$ ( $i$ = 1, 2 ), quantifying the damping characteristics of the specimens are defined as

$$\alpha_1 = \frac{(a)_A}{(a)_D} \text{ and } \alpha_2 = \frac{(b)_A}{(b)_D}, \tag{65}$$

Where $(a)_A$ is the actual (subscript *A*) Rayleigh coefficient *a*, and $(a)_D$ is the Rayleigh coefficient *a* assumed for design purpose (subscript *D*); while $(b)_A$ is the actual (subscript *A*) Rayleigh coefficient *b* and $(b)_D$ is that for design purpose (subscript *D*). Following the general design practice, $(a)_D$ and $(b)_D$ are assigned so that the finite element model derived from design drawings has 5% damping for both the first and the second modes.

The damage assessment problem is, therefore, converted to a problem of identifying the correction coefficients collectively denoted as

$$\theta = \{\beta_1, \cdots, \beta_n, \alpha_1, \alpha_2\}^T, \tag{66}$$

A multiple-input-multiple-output (MIMO) state-space formulation is developed below to predict the structural response time histories. The stiffness and damping correct coefficients are identified by minimizing errors between the predicted and the measured response time histories, based on the quasi-Newton optimization routines, as described below.

**MIMO state-space model formulation**

If the structure has $n$ degrees-of-freedom (DOFs), they can be classified into two catalogs: (i) $n_I$ DOFs associated with prescribed inputs (acceleration, velocity, displacement, or force time histories) and therefore subjected to external forces; and (ii) $n_f$ other DOFs that are not associated with inputs nor subjected to external forces, 'free' in this sense. The equations of motion are then partitioned as following by grouping the DOFs of these two catalogs denoted by subscript 'I' or 'f' respectively.

$$\begin{bmatrix} M_{II} & M_{If} \\ M_{fI} & M_{ff} \end{bmatrix} \begin{Bmatrix} \ddot{X}_I \\ \ddot{X}_f \end{Bmatrix} + \begin{bmatrix} C_{II} & C_{If} \\ C_{fI} & C_{ff} \end{bmatrix} \begin{Bmatrix} \dot{X}_I \\ \dot{X}_f \end{Bmatrix} + \begin{bmatrix} K_{II} & K_{If} \\ K_{fI} & K_{ff} \end{bmatrix} \begin{Bmatrix} X_I \\ X_f \end{Bmatrix} = \begin{Bmatrix} F \\ 0 \end{Bmatrix} \tag{67}$$

Now only address the case where inputs are specified by desired acceleration time histories. In this case, vector $F$ on the right hand site of Eq. 67, representing external forces (in this experiment, these forces are from the shake tables, transferred to the bases of the bents), is

usually not directly available. Instead, the acceleration time histories at the input DOFs are known, therefore, rewrite the motion equations in:

$$\begin{bmatrix} I & 0 \\ M_{fi} & M_{ff} \end{bmatrix} \begin{Bmatrix} \ddot{X}_i \\ \ddot{X}_f \end{Bmatrix} + \begin{bmatrix} 0 & 0 \\ C_{fi} & C_{ff} \end{bmatrix} \begin{Bmatrix} \dot{X}_i \\ \dot{X}_f \end{Bmatrix} + \begin{bmatrix} 0 & 0 \\ K_{fi} & K_{ff} \end{bmatrix} \begin{Bmatrix} X_i \\ X_f \end{Bmatrix} = \begin{Bmatrix} \ddot{X}_i \\ 0 \end{Bmatrix}. \tag{68}$$

Letting $\bar{M} = \begin{bmatrix} I & 0 \\ M_{fi} & M_{ff} \end{bmatrix}$, $\bar{C} = \begin{bmatrix} 0 & 0 \\ C_{fi} & C_{ff} \end{bmatrix}$ and $\bar{K} = \begin{bmatrix} 0 & 0 \\ K_{fi} & K_{ff} \end{bmatrix}$; and $\bar{X} = \begin{Bmatrix} X_i \\ X_f \end{Bmatrix}$ and $\bar{U} = \begin{Bmatrix} \ddot{X}_i \\ 0 \end{Bmatrix}$, a state-space representation of the structural dynamic system can be obtained by the standard procedure:

$$\begin{Bmatrix} \dot{\bar{X}} \\ \ddot{\bar{X}} \end{Bmatrix} = \begin{bmatrix} 0 & I \\ -\bar{M}^{-1}\bar{K} & -\bar{M}^{-1}\bar{C} \end{bmatrix} \begin{Bmatrix} \bar{X} \\ \dot{\bar{X}} \end{Bmatrix} + \begin{Bmatrix} 0 \\ \bar{M}^{-1}\bar{U} \end{Bmatrix}. \tag{69}$$

Assuming that the experimental measurements are the acceleration responses at some of the DOFs, the observation matrix is $O$ such that $Z = O \cdot \ddot{\bar{X}}$, the measurement $Z$ is then

$$Z = O \begin{bmatrix} -\bar{M}^{-1}\bar{K} & -\bar{M}^{-1}\bar{C} \end{bmatrix} \begin{Bmatrix} \bar{X} \\ \dot{\bar{X}} \end{Bmatrix} + O\bar{M}^{-1}\bar{U} \tag{70}$$

With this MIMO state-space model (Eqs. 69 and 70), responses can be efficiently simulated. When the structure is parameterized, $M_{fi}$, $M_{ff}$, $C_{fi}$, $C_{ff}$, $K_{fi}$ and $K_{ff}$ are all argumented by the parameter $\theta$. Therefore, the MIMO state-space model is a good device to simulate the responses when the structure status is represented by a finite number of parameters, facilitating the system identification procedure.

**Parameter identification**

A weighted-nonlinear-least-square procedure was used to identify $\alpha_i$'s and $\beta_i$'s (i.e., $\theta$) based on measured low-amplitude acceleration responses of a structure. The object function is to minimize the difference between measured and simulated acceleration time histories:

$$Obj(\theta) = (\Delta \mathbf{Z})^T \mathbf{W} (\Delta \mathbf{Z}) \tag{71}$$

where, $\Delta \mathbf{Z} = \mathbf{Z}^M - \mathbf{Z}(\theta)$. $\mathbf{Z}^M$ is a matrix containing the measured time histories of the acceleration responses at the sensor locations, arranged in such a way that its columns are associated with different sensor channels and rows are associated with increasing time. $\mathbf{Z}(\theta)$ is a matrix of simulated acceleration responses using the MIMO state-space model parameterized by $\theta$, arranged in the same manner as $\mathbf{Z}^M$. $\mathbf{W}$ is the inverse matrix of the covariance of the noises in different channels, so that the channels with lower noise level are trusted more than those with higher noise level. The identification of sectional stiffness reduction is now optimizing $\theta$ to obtain a minimum of the object function.

Parameters in $\theta = \{\beta_1, \cdots, \beta_n, \alpha_1, \alpha_2\}^T$ are each confined to a lower bound and an upper bound, based on a priori knowledge of the structural system. To reduce the risk of converging to a local minimum, a large number of random searches are performed to obtain a globally plausible initial set of $\theta^0$. In each of the random search, $\beta_i^0$'s and $\alpha_i^0$'s are randomly picked from uniform distributions between their lower and upper bounds. The smallest $Obj(\cdot)$ is registered and the associated set of $(\beta_1^0, \cdots, \beta_n^0, \alpha_1^0, \alpha_2^0)$ is adopted as the initial values for quasi-Newton optimization (Polak, 1997). The quasi-Newton optimization further refines the parameters, and obtains the parameters that best reconcile the simulated and measured responses.

### 3.6.2 Validation by Seismic Shaking Table Tests

The proposed damage assessment method based on quasi-Newton optimization is validated through the seismic shaking table tests of the three-bent two-column concrete bridge model. As described in Section 3.2, the bridge model was subjected to a series of low to high amplitude earthquakes, inducing progressive seismic damage to the structure. Between earthquake ground motions, low amplitude white noise excitations were input to the bridge structure to simulate ambient vibration. Eleven accelerometers were installed on the tables and bridge to record input ground motions and the responses of the structure.

The objective is to demonstrate that the stiffness of the bridge columns can be reliably identified by processing the measured low-amplitude vibration data, and the change of the stiffness pre- and post-earthquake can be reliably linked to the structural damage observed by visual inspection and by the embedded strain sensors (as presented in Table 1).

Responses to the white noise excitations are used to identify three stiffness and two damping correction coefficients, $(\beta_1, \beta_2, \beta_3, \alpha_1, \alpha_2)$. Each of the three $\beta_i$ is for each of the three bents of the bridge. Each of the parameters is confined to a lower bound 0.001 and an upper bound 4, based on a priori knowledge of the bridge structure. 500 to 1000 times of random searches are performed to obtain a globally plausible initial set of $\theta^0$. In each of the random search, $\beta_i^s$'s and $\alpha_i^s$'s are randomly picked from uniform distributions between their lower and upper bounds. The smallest $J(\theta)$ is registered and the associated set of $(\beta_1^s, \beta_2^s, \beta_3^s, \alpha_1^s, \alpha_2^s)$ is adopted as the initial values for quasi-Newton optimization. The quasi-Newton optimization further refines the parameters, and obtains the parameters that best reconcile the simulated and measured responses.

Following the optimization method outlined above, the correction coefficients are identified at different damage stages using the acceleration measurements obtained in the low-amplitude white noise tests. The identified stiffness and damping correction coefficient results are listed in Table 3.

Table 3. Identified Stiffness and Damping Correction Coefficients

| TESTS | $b_1$ | $b_2$ | $b_3$ | $a_1$ | $a_2$ |
|---|---|---|---|---|---|
| WN-1 | 0.78 | 0.79 | 0.85 | 1.02 | 2.05 |
| WN-2 | 0.53 | 0.80 | 0.61 | 0.33 | 6.24 |
| WN-3 | 0.19 | 0.31 | 0.18 | 0.82 | 3.52 |
| WN-4 | 0.20 | 0.16 | 0.11 | 2.12 | 1.28 |
| WN-5 | 0.17 | 0.13 | 0.13 | 0.85 | 4.21 |

The sectional stiffness correction coefficients for the three bents are further plotted in Fig. 33. The identified stiffness degradation clearly indicate the same damage procedure as observed in the experiment. Bent 1 yields **à** Bent 3 yields **à** Bent 2 yields **à** Bent 3 steel buckles. Between the two white noise tests, WN-X-1 and WN-X-2, $\beta_1$ and $\beta_3$ drop from 0.78 to 0.52 and from 0.84 to 0.61 respectively, while $\beta_2$ remains same level, indicating in a quantitative manner the yielding of Bent 1 and Bent 3 between these two tests. Then between WN-X-2 and WN-X-3, the decrements in all $\beta_1$, $\beta_2$ and $\beta_3$ signal that not only Bent 2 yielded, but also the damage in Bent 1 and Bent 3 further developed. In WN-X-4, $\beta_3$ touches down to a very low value, 0.11, associating with the severe damage in Bent 3 (steel buckling). And the results of WN-X-5 are comparable to those in WN-X-4, which is consistent with the observation that the after-shot earthquake actually had not further damaged the bridge specimen significantly.

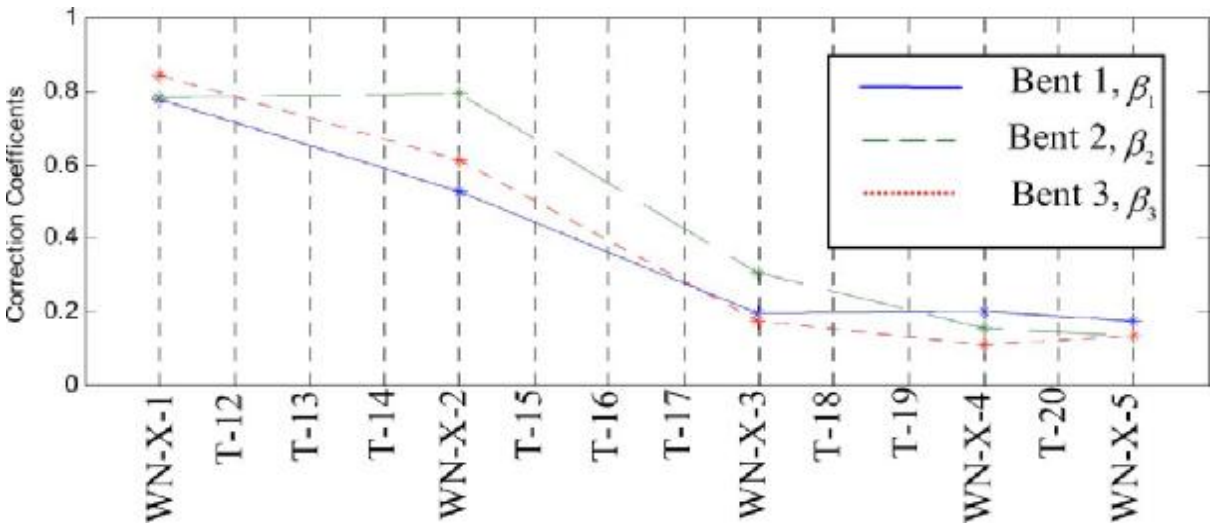


Figure 33 Identified Stiffness Degradation

To further verify the identified results, a MIMO model with proper corrections made according to the identified $(\beta_1, \beta_2, \beta_3, \alpha_1, \alpha_2)$ were used to simulate the bridge responses to WN-X-2, and WN-X-5 ground motions in time domain. They capture the primary characteristics of the bridge response, as evident in the time-history simulation shown in Fig. 34. The accuracy of the identified stiffness and damping change is clearly demonstrated.

In conclusion, the seismic shaking table test results validated the proposed quasi-Newton optimization method, by demonstrating that the stiffness reduction of the bridge columns can be reliably identified by processing the measured vibration data, and the amount of stiffness reduction shows a strong correlation with the extent of damage observed by visual inspection and by the embedded strain sensors. The identified damage locations also agree well with the observations.

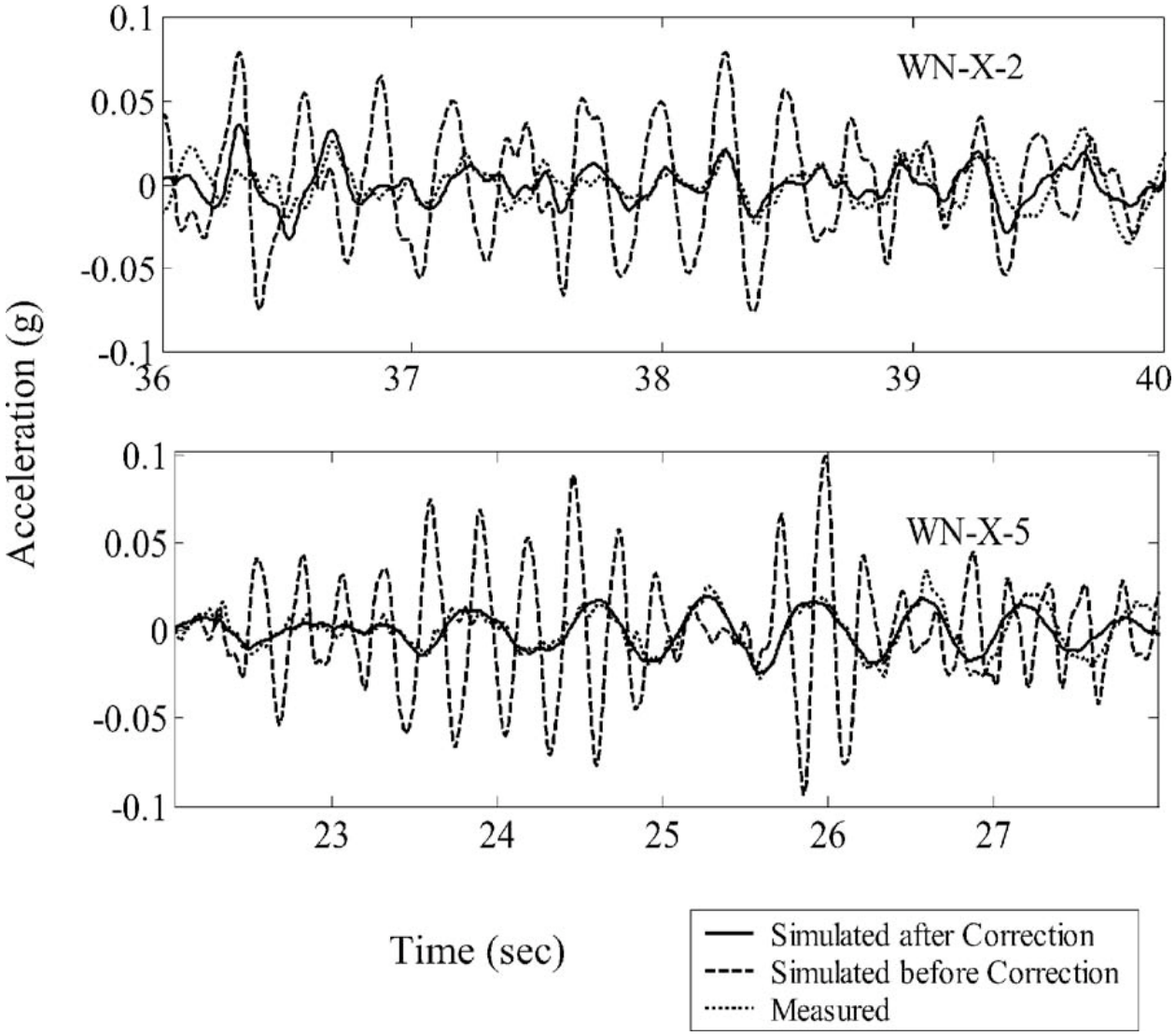


Figure 34 Comparison of Responses Measured and Simulated (wt and w/o Parameter Correction)

Based on previous discussion on hysteresis behavior in post-event low amplitude vibration, $\beta_i$ (in both experiments) is a quantitative indicator of the structural condition of the bent, which can be plausibly postulated as the secant sectional stiffness at the associated damage stage normalized by the initial sectional stiffness. If a pushover analysis is performed and a

capacity curve of the specimen is obtained, $\beta_i$ can further be correlated to the deformation capacity reservation the specimen/element has at a damage stage. This can be better seen later when experimental hysteresis is examined in Section 3.8..

# 3.7 DAMAGE ASSESSMENT BASED ON GENETIC ALGORITHM OPTIMIZATION

Conventional optimization methods, such as the quasi-Newton optimization presented in Section 3.6, are gradient based and may lead to a local minimum depending on the assumed initial parameter values. In order to overcome this difficulty, genetic algorithms (GA's) are proposed to improve the initial parameter search in the optimization process. This section presents the GA-based optimization method and the experimental validation by the seismic shaking table tests of the two-span three-bent bridge.

The objective is to demonstrate that the stiffness of the bridge columns can be reliably identified by processing the measured low-amplitude vibration data using the genetic algorithm-based optimization method, and the change of the stiffness pre- and post-earthquake can be reliably linked to the structural damage observed by visual inspection and by the embedded strain sensors (as presented in Table 1).

In addition to the ambient white noise response data (as shown in Section 3.5), the GA-based optimization method is also applied to the seismic data by using the low-amplitude segments of the seismic responses. For the white noise data, the structural parameter (such as the sectional stiffness of a bridge column) is identified in the time domain by minimizing errors between measured and simulated response time histories. For the seismic data, the optimization is performed in the frequency domain by minimizing errors between measured and simulated modal parameters (such as natural frequencies and modal shapes). The measured modal parameters are those extracted from low-amplitude segments of the seismic response (i.e., pre- and post-strong motion segments) using the frequency response functions. It is noted that data recorders usually have buffer that stores 5 to 10 seconds of pre-event data, as illustrated in Fig. 35. The following subsections describes the genetic

algorithm-based optimization method and its experimental validation by the seismic shaking table tests.

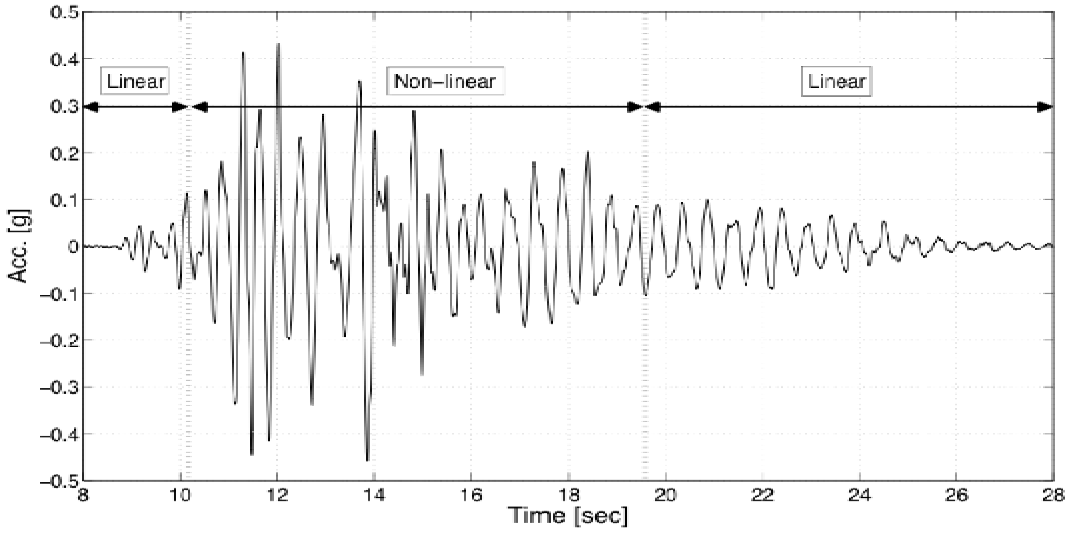


Figure 35 Three Segments of Earthquake Response Time History

### 3.7.1 Genetic Algorithm-Based Optimization

The goal of the optimization is to identify changes in structural parameters such as stiffness due to structural damage by minimizing the errors (i.e., the objective function) between modal parameters measured from structural vibration data and estimated from a parameterized analytical model. Based on the identified stiffness changes in individual structural members, the existence, location, and extent of damage can be assessed. In other words, the problem of structural damage assessment is implemented as an optimization problem. The modal parameters including natural frequencies and mode shapes can be

extracted from the measured low-amplitude (linear) segments of seismic responses using, for example, transfer function techniques.

An optimal set of the structural parameters are found by searching the parameter space for a set of structural parameters that minimizes a weighted objective function.

$$J_2 = \sum_{i=1}^{n_d} \left( W_{fi} \Delta f_i + W_{\phi i} \left(1 - MAC_i\right) \right) \tag{72}$$

Where:

$$\Delta f_i = \left| \frac{f_i^e - f_i^a}{f_i^a} \right| \tag{73}$$

$$MAC_i = \frac{\left( (\phi_i^a)^T . (\phi_i^e) \right)^2}{\left( (\phi_i^a)^T . (\phi_i^a) \right) \left( (\phi_i^e)^T . (\phi_i^e) \right)} \tag{74}$$

Where $x$ is the model parameters set, $i$ is the number of identified experimental modes and $W_{fi}$ and $W_{fi}$ are the user specified weights for the error between analytical and experimental frequencies and mode shapes respectively.

Genetic algorithms (GA's) are proposed to identify values of the structural parameters (such as sectional stiffness of a column) in the analytical model by minimizing the objective functions. GAs are a type of evolutionary algorithms that are stochastic optimization techniques based on laws of nature and biology. Conventional optimization methods are gradient based and usually lead to a local minimum only, but GAs are considered as a global optimization technique that can derive a more accurate and reliable solution (Holland, 1975, Friswell et. al., 1998, Chou and Ghaboussi, 2001, Au et. al., 2003, Franco et al. 2004, Koh et. al., 2003, Shim and Suh, 2003, Haralampidis et al., 2005, Rao et.al., 2004, Alimoradi et. al., 2006, Raich and Liszkai, 2007, and Kouchmeshky et. al., 2007). One of the most important characteristics of GA's is their effectiveness and

robustness in dealing with uncertainty, insufficient information and noise. GA's process starts with a population of individuals where each individual, as a point in parameter space, represents a candidate solution to the optimization problem. Starting from a population rather than a single individual, as in the conventional optimization techniques, minimizes the probability of being trapped in a local minimum. As in nature, population of individuals evolves in generations. In other words, average fitness of the new generation is equal or higher than the average fitness of the current generation provided that appropriate selection and genetic operators are applied for generation of the new population. The evolving process in GA's is summarized as follows:

- Choose an initial population of S individuals $\Theta_0 = [q_{1,0}, q_{2,0} \mathbf{K} q_{S,0}]$
- Evaluate objective function for all of individuals of the initial population ($Obj(\Theta_0)$).
- Iterate for k = 1, 2, …
- Apply selection operator: $\Theta_{new} = Select(\Theta_{k-1})$.
- Apply genetic operators (crossover, mutation, etc.): $\Theta_k = Genops(\Theta_{new}))$.
- Test for the termination criterion and either go to step 3 or stop.

The selection function decides which individuals are carried over to the next generation based on their fitness values. This function in GA's works stochastically, which means that the survival of no individual is guaranteed although higher survival probabilities are assigned to fitter individuals. Random experiments select the parent individuals for the next generation. Different GA selection schemes are proposed to date. The most common one is the so-called *roulette wheel selection*. In this method the probability of survival of each individual is defined as the ratio of the fitness value of that individual to sum of fitness values of all individuals. The main drawback of this scheme is that the selection process

depends on the exact definition of fitness function and not only on the ranking of the individuals. Alternatives to roulette wheel selection are the ranking-based selection schemes. They base the selection on the ranking of each individual in whole population rather than on its absolute fitness value. In this paper, a ranking-based selection operator, called *tournament selection*, is used for selection of parents. In this selection scheme a group of individuals are selected randomly and the best individual is selected as a parent. The tournament selection has several benefits: it is efficient to code, works on parallel architectures and allows the selection pressure to be easily adjusted. The selection pressure is an evolutionary variable that controls the convergence behavior of the algorithm. A very high selection pressure decreases the diversity of the population since only the very best individuals have a significant probability of surviving. This lowers the capability of GA's in exploring new regions of the parameter space and may lead to convergence to local optima. On the other hand, a very low selection pressure makes GA's to work too global and inefficient.

GA operators are mechanisms such as crossover and mutation that ensure diversity in the populations by introducing random variations in the solution set. Once the parent population is available, crossover allows for the creation of new individuals based on the previous generation. Crossover is the most important genetic operator in which the bit-strings of two (or more) parents are cut into two (or more) pieces and the parts of bit-string are crossed over. The point where the parents are cut is determined randomly. In the strategy presented here, a uniform crossover function is used in which each parameter of the child is selected from parents' parameters with uniform probability. Through the crossover operator a new child population has been created using inherited values from the parent population. The mutation operator is used to insert new information into the new population and prevent GA from getting stuck in certain regions of the parameter space. The mutation consists of making slight changes in parameters of child population after they have been generated by crossover. Changes in parameters of each individual are calculated using a Gaussian distribution centered on zero. Standard deviation of the distribution is set

to shrink as the number of generations increases which lets GA to search more global at the very first generation and more local at final generations (where the algorithm is about to converge).

In order to stop the evolutionary process and accept the fittest individual as the final solution to the optimization problem, one or several criteria have to be established. Limiting the number of generations or the evolution time is from the common criteria. Another way is to stop the process if the rate of change in fitness of best individual is less than a certain value or fitness exceeds a certain threshold. In this study, the number of generations is limited to 100 generations and the process has been set to stop if the change in fitness of the best individual in the last 10 generations falls below 0.001. No limits are imposed on best individual's fitness or objective value. In general convergence to a near-global optima is always guaranteed if evolution continues for sufficient generations and the solution lies within the boundaries of the search space.

### 3.7.2 Validation by Seismic Shaking Table Tests

The proposed GA-based optimization method is experimentally validated by the seismic shaking table tests of the large three two-column Bent concrete bridge model. As described in Section 3.3, the bridge model was subjected to a series of low to high amplitude earthquakes, inducing progressive seismic damage to the structure. Between earthquake ground motions, low amplitude white noise excitations were input to the bridge structure to simulate the effect of traffic induced motions. Eleven accelerometers were installed on the tables and the bridge to record input ground motions and the responses of the structure. For the validation purposes, strain sensors were installed on the column rebar and embedded in concrete during the construction.

The objective of the validation is to demonstrate that the stiffness of the bridge columns can be reliably identified by processing the measured low-amplitude vibration data using the genetic algorithm-based optimization method, and the change of the stiffness pre- and post-earthquake can be reliably linked to the structural damage observed by visual inspection and by embedded strains sensors (as presented in Table 1).

**Damage Detection Based on Seismic Response Data**

Both the seismic response and the white noise response data are used to identify the change in structural stiffness of the bridge. For the seismic data, the structural stiffness values are identified by minimizing errors between measured and simulated modal parameters, using the GA-based optimization. The measured modal parameters are those extracted from the low-amplitude segments of seismic data by the FRF estimator. Figure 36 plots the FRF's of the last low-amplitude segments of the bridge responses (as the third segment in Figure 35) to earthquake ground motion T-12 through T-18. The cut-off timing of such a segment is determined at the time when the acceleration response becomes less than 0.1g. In the figure, the peak of each FRF function is marked by a red circle, from which the natural frequency is picked. Table 4 summarizes the identified first natural frequency and the first mode shape of the bridge. Again, the natural frequency decreases as the seismic damage to the bridge becomes more severe.

The change of element stiffness values in the bridge caused by the seismic damage is identified based on the modal identification results in Table 4, using the GA-based optimization method. A finite element model of the structure is built using the OPENSEES software. The change of stiffness is defined by stiffness correction coefficient, $\beta_i$' , which is a fraction of the designed sectional stiffness, as defined in Eq. 63. Four stiffness correction coefficients are defined for the bridge model in this study: three correction coefficients for the bending stiffness of the three different Bents and one for the bending stiffness of the deck. The results are shown in Table 5 and Fig. 37.

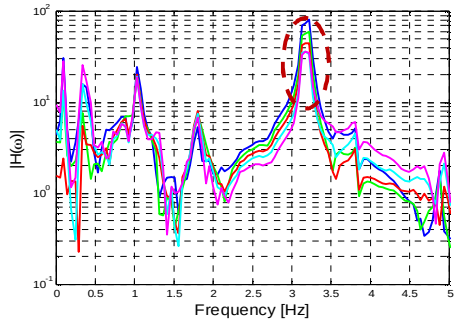


(a) T-12

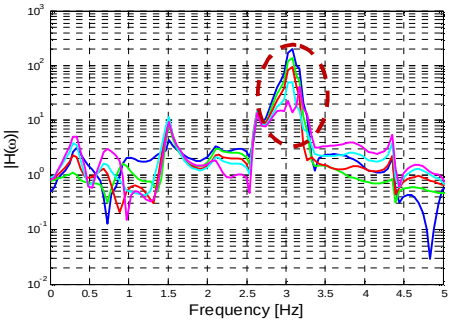


(b) T-13

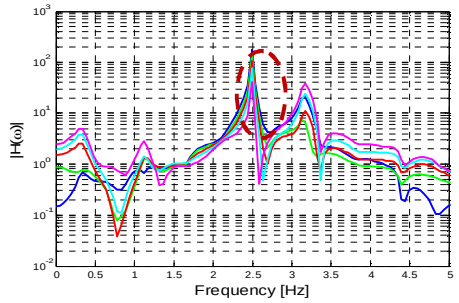


(c) T-14

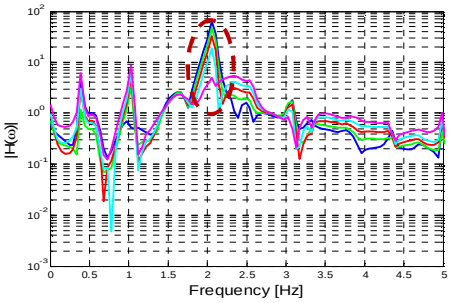


(d) T-15

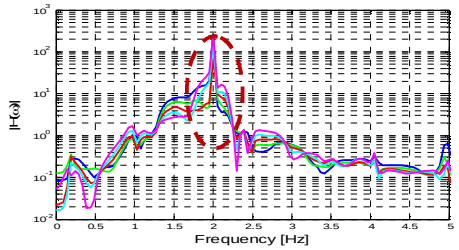


(e) T-17

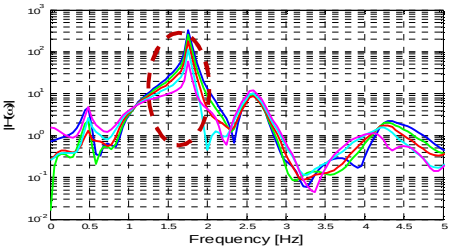


(f) T-18

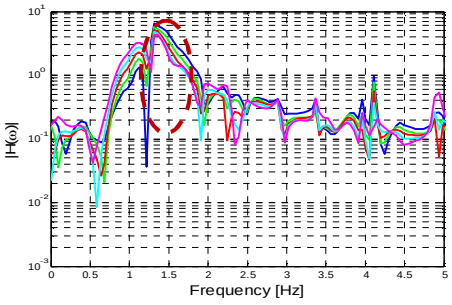


(g) T-19

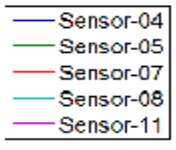


Figure 36 Frequency Response Functions

Table 4 Modal Identification Results Using FRF Technique

| Tests | $f_1$ (Hz) | . $f_{4-1}$ | . $f_{5-1}$ | . $f_{7-1}$ | . $f_{8-1}$ | . $f_{11-1}$ |
|---|---|---|---|---|---|---|
| WN-1 | 2.880 | 0.595 | 0.514 | 0.434 | 0.350 | 0.264 |
| WN-2 | 2.490 | 0.644 | 0.518 | 0.419 | 0.315 | 0.208 |
| WN-3 | 1.662 | 0.661 | 0.511 | 0.390 | 0.292 | 0.253 |
| WN-4 | 1.456 | 0.595 | 0.498 | 0.433 | 0.356 | 0.289 |

**Damage Detection Based on White Noise Ambient Vibration Data**

On the other hand, for the white noise data, the structural stiffness values are identified by minimizing errors between the measured and simulated response time histories with the objective function shown in Eq. 71. The genetic algorithms are used to solve the optimization problem. The identified stiffness correction coefficients are shown in Table 6 and Fig. 37, together with those identified based on the seismic data.

Table 6 Identified Stiffness Correction Coefficients

| | BENT-1 | BENT-2 | BENT-3 |
|---|---|---|---|
| **WN-1** | 1.000 | 1.000 | 1.000 |
| **T-12** | 1.000 | 1.000 | 1.000 |
| **T-13** | 0.634 | 0.990 | 0.813 |
| **T-14** | 0.599 | 0.784 | 0.639 |
| **WN-2** | 0.721 | 0.784 | 0.786 |
| **T-15** | 0.397 | 0.676 | 0.324 |
| **T-16** | 0.280 | 0.379 | 0.260 |
| **T-17** | 0.261 | 0.389 | 0.232 |
| **WN-3** | 0.224 | 0.396 | 0.220 |
| **T-18** | 0.235 | 0.269 | 0.199 |
| **T-19** | 0.222 | 0.129 | 0.113 |

| | | | |
|---|---|---|---|
| **WN-4** | 0.211 | 0.232 | 0.178 |

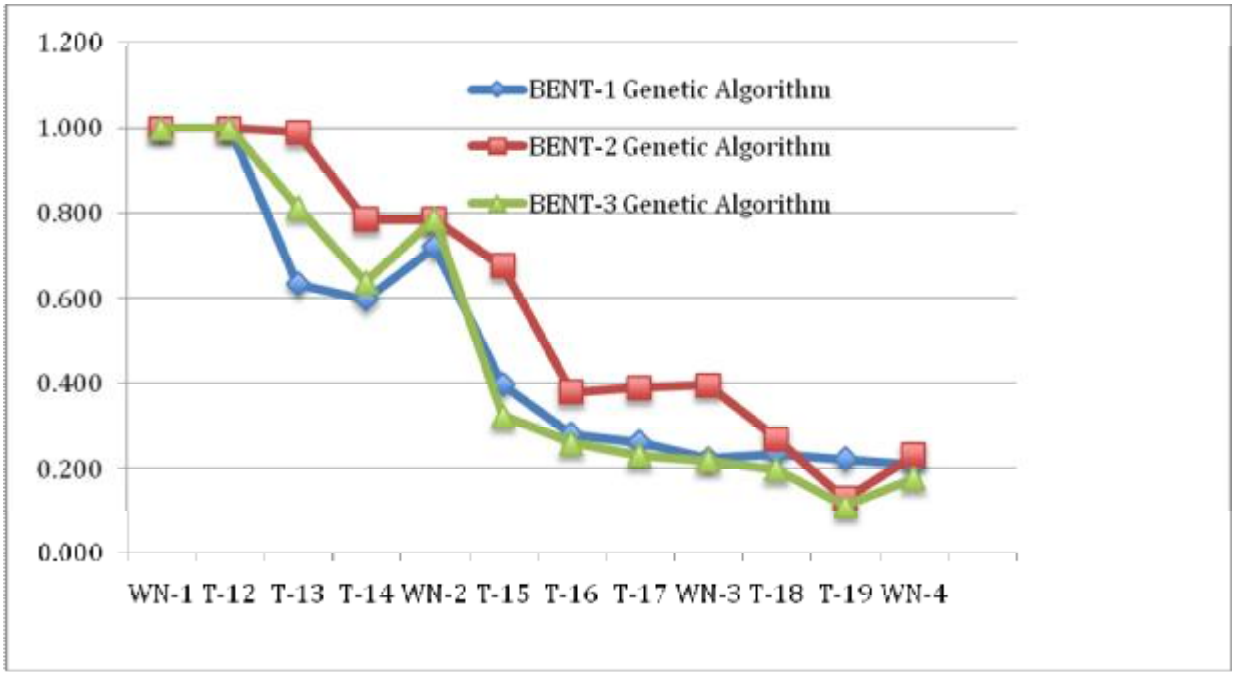


Figure 37 Identified Stiffness Degradation

The identified damage locations and extents at each step of the tests shown in Fig. 37 are in good agreement with the damage description (shown in Table 1) provided by the visual inspection and the measurements from the embedded strain. The identified stiffness degradation clearly indicates the same damage procedure as observed in the experiment. Bent 1 yields **à** Bent 3 yields **à** Bent 2 yields **à** Bent 3 steel buckles. Furthermore, the results based on the seismic data by minimizing the measured and simulated modal parameters, agree well with the results based on the white noise data by minimizing the measured and simulated acceleration time histories.

In conclusion, the seismic shaking table test results validated the proposed genetic algorithm-based optimization method, by demonstrating that the stiffness reduction of the

bridge columns can be reliably identified by processing the measured low-amplitude vibration data, and the amount of stiffness reduction shows a strong correlation with the extent of damage observed by visual inspection and by the embedded strain sensors. The identified damage locations also agree well with the observations.

# 3.8 REMAINING CAPACITY ESTIMATION

The ultimate goal of this project is to provide a tool for assisting decisions regarding post-event operations of bridges. The identified structural damage represented by the stiffness degradation needs to be further linked to the remaining load carrying capacity of the bridge. This study proposes a new pushover analysis-based method for estimating the remaining capacity based on the identified stiffness degradation. The push-over analysis is now required for seismic design of a bridge to check its ultimate lateral displacement capacity, and thus bridge capacity curves are available.

The remaining capacity of a bridge is estimated by superposing a line (with a slope equivalent to the identified stiffness) onto the capacity curve of a bridge column, and compare the displacement at the pivot point with the ultimate displacement capacity. A structure, particularly a concrete structure, experiencing a damaging event, exhibits significant hysteresis behaviors and thus is a nonlinear system. However, the same structure experiencing low-amplitude ambient vibration pre- and post the event can be modeled as a linear and time-invariant (LTI) system. This section first examines hysteresis loops that a structure experiences in low-amplitude vibration following an established hysteresis model. This provides a conceptual justification for the use of a linear line to represent the post-event stiffness. Then, the procedure for remaining capacity estimation based on the pushover analysis is described. Finally the method is validated by the seismic shaking table tests.

## 3.8.1 Hysteresis in Low Amplitude Vibration

Many hysteresis models have been developed (e.g., Bouc, 1967; Clough, 1966; Takeda et al., 1970; Wen, 1976) to characterize the force-deformation relation of a structural component in cyclic loading. Efforts have been made to present these models in a holistic

manner (Sain et al., 1997; Sivaselvan and Reinhorn, 2000). Among them, the Takeda model is one of the most used. It is accepted as a realistic model because it was experimentally developed and verified (Takeda et al., 1970). The detail empirical rules in the original Takeda model have been simplified and modified aiming at a more efficient numerical implementation and a better account for phenomena such as pinching (e.g., Emori and Schnobrich, 1981; Saiidi, 1982; Takayanagi and Schnobrich, 1979). In Park et al. (1987), it was found that the stiffness degradation can be accurately predicted by the pivot rule, according to which, the load-reversal branches are targeting a pivot point on the opposite side. In terms of this rule, the bi-linear Takeda model shown in Fig. 38 can be described as: (i) loading/reloading rule – if the structure has never yielded in the loading direction, the pivot point is the yielding point; otherwise, it is the largest excursion point (the maximum deformation ever reached in this direction); and (ii) unloading rule – the elastic unloading slope is same to the initial stiffness $k_0$, while the post-yielding unloading follows a slope of $k_u = k_0(d_y/d_m)^{0.5}$, where $d_y$ and $d_m$ are the yielding and largest excursion deformations, respectively.

Following this hysteresis model, the force-deformation paths under low amplitude vibrations can be examined:

(a) Pre-event loops:

Assuming that the vibration amplitude is so low that yielding of the structure is not engaged before the event, the pivot points are the yielding points in both directions. The loops degrade to a straight line with a slope equal to the initial stiffness $k_0$.

(b) Post-event loops:

If the event is damaging, yielding in either/both directions might have occurred. Assuming again that the post-event vibration amplitude is small and no further damage is engaged (which implies that the largest excursion points ever reached in the damaging event have not been exceeded during the entire post-event low amplitude vibration), both the pivot points are the largest excursion points in the

positive and negative directions and they remain unchanged. Therefore the hysteresis goes through narrow loops (solid line in Fig. 39) that lay on top of the straight line connecting the two pivot points. A structure in such vibration generally behaves as if a linear system with a degraded stiffness ($k_a \approx F_m/d_m$) and a lightly increased damping ratio compared to pre-event situations.

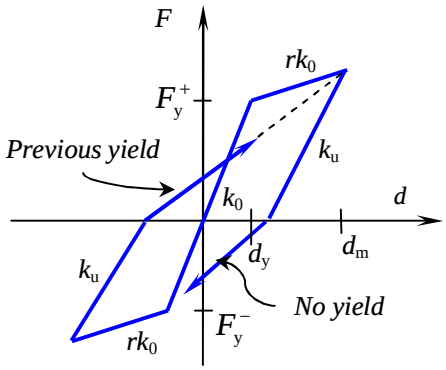


Figure 38 Hysteresis Loop

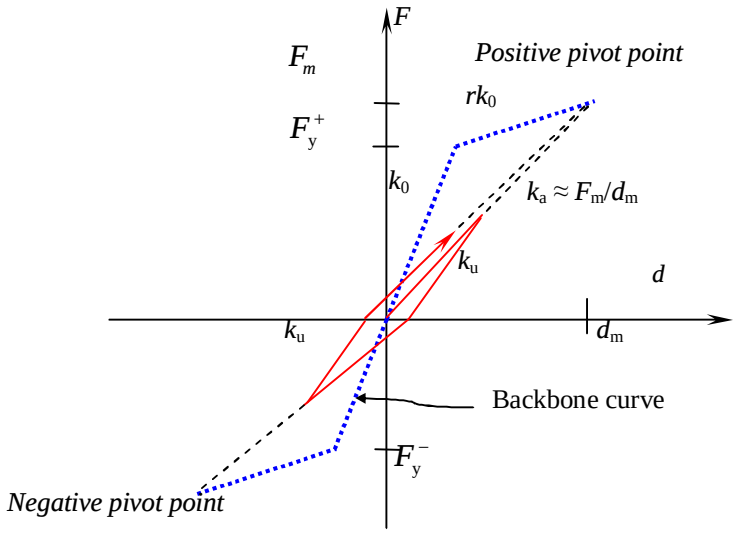


Figure 39 Post-Event Low-Amplitude Hysteresis Loop

This observation suggests that pre- and post-event low amplitude vibrations can be treated as if a LTI system, which significantly eases the identification of structural properties.

Moreover, the post-event effective stiffness $k_a$ is meaningful if correctly identified based on vibration measurements, because it can be converted back to the largest excursion point during the damaging event, if a backbone curve is obtained by e.g., a pushover analysis. The point of largest excursion contains crucial information to evaluate the residual strength and deformation capacity the damaged structure still possesses. This postulation is supported by experimental data to be discussed later.

A note shall be made here on the measurability of hysteresis loops. Hysteresis, by definition, is the relation of restoring force vs. deformation of a structural component. Deformation can be readily measured by a displacement sensor or a strain gauge in structural tests. Direct measurement of restoring force, however, is not always available, except in static or pseudo-dynamic tests where load cells are used. In a dynamic test (i.e. shake table test) of a nonlinear multi-degree-of-freedom system involving multiple structural components, the variation of relative stiffness among components during the test will cause force redistribution. As a result, the global inertial force is no longer proportional to the restoring force of an individual component. In such cases system identification methods can play an important part in constructing the hysteresis curve of a particular structural component.

It shall be also understood that, pertaining to structural condition is the hysteresis of critical structural components, not the global hysteresis of the entire structure. It has been documented in several lab and field tests that a structural assembly of components can vary its global stiffness in a considerable wide range without significant damage being observed. One explanation for this phenomenon is that, the changes of the hysteresis of some uncritical components (such as loosing of an anchorage, or cracking or softening in some

pre-selected regions, e.g. end zones of slab or gravity beams, which have been engineered to accommodate such plastic behaviors), are not impairing the overall structural performance thus not considered as damage to an assembly. The change of characteristics of uncritical components, however, is reflected in the global hysteresis of the assembly. For example, a gap developed due to an insignificant loose in the anchor bolts could result in apparent change in the hysteresis of a wall assembly, but the wall panel may still in a sound condition. Ideally for structural condition assessment, one should monitor the hysteresis changes of those components pertaining to structural performance, not the global hysteresis of an assembly. To do so, it is important to obtain from dynamic data the hysteresis for a selected component.

### 3.8.2 Pushover Analysis-Based Capacity Estimation

In the proposed method, the remaining capacity of each column of a bridge is computed by estimating the maximum displacement reached at the top of the column during an event and then comparing it with the designed ultimate displacement. The post-event stiffness of a bridge column identified from the post-event low-amplitude response data (such as the third region in the seismic response time history shown in Fig. 35, or ambient vibration response) can be converted back to the largest excursion point, referred to as a pivot point, during the damaging event, given a capacity curve of the column (Park et al, 1987). The pivot point is the intersection of the post-event stiffness line and the capacity curve, as illustrated in Fig. 40. By comparing the displacement of the pivot point with the ultimate design displacement, the remaining capacity of the column is estimated. The remaining capacity of the entire bridge is determined by the most critical column whose remaining capacity is the least among all the columns.

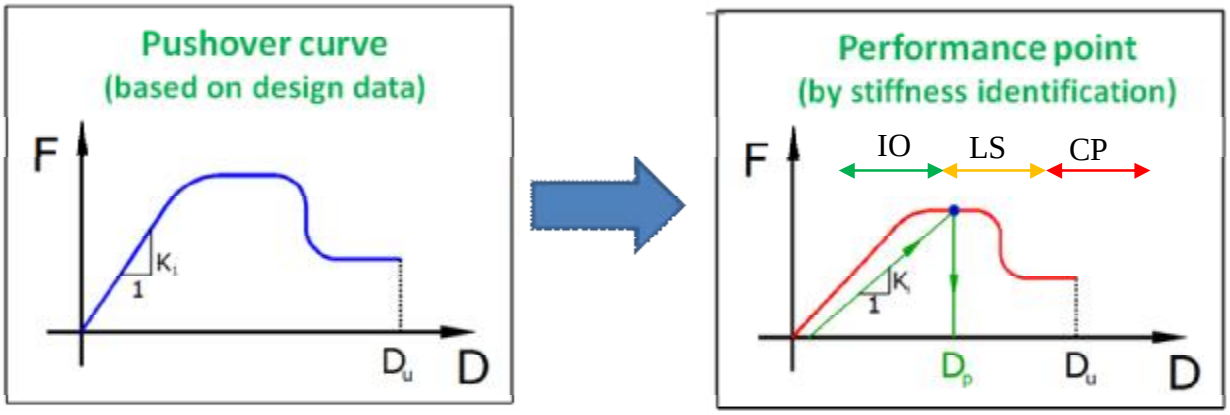


Figure 40 Remaining Capacity Estimation

The estimated remaining capacity can be used to assist post-event decisions. For example, FEMA 356 -- Prestandard and Commentary for the Seismic Rehabilitation of Buildings -- attempts to link the capacity to decision for buildings (FEMA, 2000). In FEMA 356 decisions regarding immediate occupancy (IO), life safety (LS) and collapse prevention (CP) are based on column plastic hinge performance criteria. For a given column, the rotation-based hinge performance criteria can be converted to the column displacement performance criteria, as illustrated in Fig. 40. The decision criteria for the buildings can be applied to bridges by interpreting "immediate occupancy" as "open to traffic", "life safety" as "partially open to traffic", and "collapse prevention" as "close to traffic".

Therefore, based on the post-event structural stiffness identified in Sections 3.5 through 3.7, the remaining capacity of the bridge can be evaluated, and decisions subsequently made regarding post-event bridge closure and repair prioritization. The remaining capacity estimation and decision procedure can be summarized in the following steps:

Step I: Establish a pushover capacity curve for each of the bridge columns, which should account for cyclic stiffness and strength degradation of the section.

Step II: Determine the ultimate displacement $D_u$ of the column considering all possible failure mechanisms of the column (shear, flexure or torsion).

Step III: After a major event, find the pivot point displacement, $D_p$, by superposing a post-event stiffness line from the origin with the slope equal to the identified stiffness.

Step IV: Compute the remaining capacity of the column by

$$Capacity = \frac{D_u - D_p}{D_u} \% \tag{75}$$

Step VI: Repeat Steps I through V for all the columns of the bridge. Select the least remaining capacity of all the columns and use it as the remaining capacity of the bridge.

Step VII: Based on the preset criteria on the remaining capacity, decisions are made on post-event bridge operations, i.e., "open to traffic", "partially open to traffic", or "closed to traffic. The remaining capacity results can also assist to prioritize the post-event repair and rehabilitation of bridges.

### 3.8.3 Validation by Seismic Shaking Table Tests

**Validation of LTI Assumption**

First the LTI assumption for the post-event bridge under low-amplitude vibration finds supports in experimental observation in the seismic shaking table tests of the large three two-column Bent concrete bridge model. As described in Section 3.3, the bridge model was subjected to a series of low to high amplitude earthquakes, inducing progressive seismic damage to the structure. Between earthquake ground motions, low amplitude white

noise excitations were input to the bridge structure to simulate the effect of traffic induced motions.

Plots in Fig. 41 are generated using data from the same shaking table tests described above (Johnson, et al., 2006) to reveal the hysteresis during low amplitude vibration, in order to validate the proposed LTI assumption and the identified stiffness reduction coefficient. The recorded time-history of the force exerting on Bent 3 of the bridge specimen during T-13, T-14, T-15 and T-19 was first plotted. Then a threshold of ±20 kips was selected and the record of each test was divided into three segments. The first segment, e.g. Segment (*a*) in T-13, is the 'pre-event' segment, which starts when the test began and ends when the exerting force magnitude first exceeded the selected threshold. The second segment, e.g. Segment (*b*) in T-13, is the 'event' segment, which follows the pre-event segment and lasts until the force magnitude was retained smaller than the threshold in that test. Then follows the third segment, e.g. Segment (*c*) in T-13, the 'post-event' segment. In both pre- and post-event segments, the bent experienced low-amplitude vibration, while in the event segment the vibration amplitude can be high enough to introduce damage to the bent. Twelve segments, Segments (*a*) to (*l*), are thus defined from the four test records. In each of the segment, the record of exerting force is plotted vs. the synchronized displacement record, resulting in the hysteresis curves (*a*) to (*l*) in Fig. 41 for Segments (*a*) to (*l*) respectively. In contrast to the hysteresis in the event segments, particularly Segment (*k*), where the instantaneous stiffness went through abrupt changes, the hysteresis curves during low-amplitude vibration, in both pre- and post-event segments, exhibit very narrow loops and are apparently single lines in graphs (*a*), (*c*), (*d*), (*f*), (*g*), (*i*), (*j*) and (*l*) in Fig. 41. This suggests that the system behavior under low-amplitude vibration can be described with acceptable accuracy by a LTI model.

A closer examination of the hysteresis curves in Fig. 41 reveals that, although the system appears to have some self-healing capacity and starts with similar initial stiffness in all tests in the pre-event Segments (*a*), (*d*), (*g*) and (*f*), the slopes (equivalent stiffness) of hysteresis

curves in the post-event segments, Segments (*c*), (*f*), (*i*) and (*l*), do indicate the accumulated damage of the bent. The stiffness decreases between tests and the curves are pointing to the largest excursion points the bent experienced in the events, as it is predicted by the pivot rule.

**Validation of Pivot Points**

The estimated maximum displacement of the bridge column experienced during a seismic event was further validated by the seismic shaking table tests. First, the displacement responses measured at the top of the columns are plotted against the acceleration responses measured at the same locations. It is noted that the acceleration responses are proportional to the inertial forces. In Fig. 42, the acceleration recorded at the top of Bent 3 is plotted against the displacement recorded at the same location respectively for seismic excitation tests T-12 through T-19. The maximum excursion points, theoretically the pivot points, in both positive and negative directions are highlighted by red dots. This procedure is performed for all the three Bents of the bridge. Then, the maximum excursion points under all the seismic shaking tests, from the low-amplitude T-12 through the high-amplitude T-19, are plotted in Fig. 43 for Bent 1, Bent 2, and Bent 3.

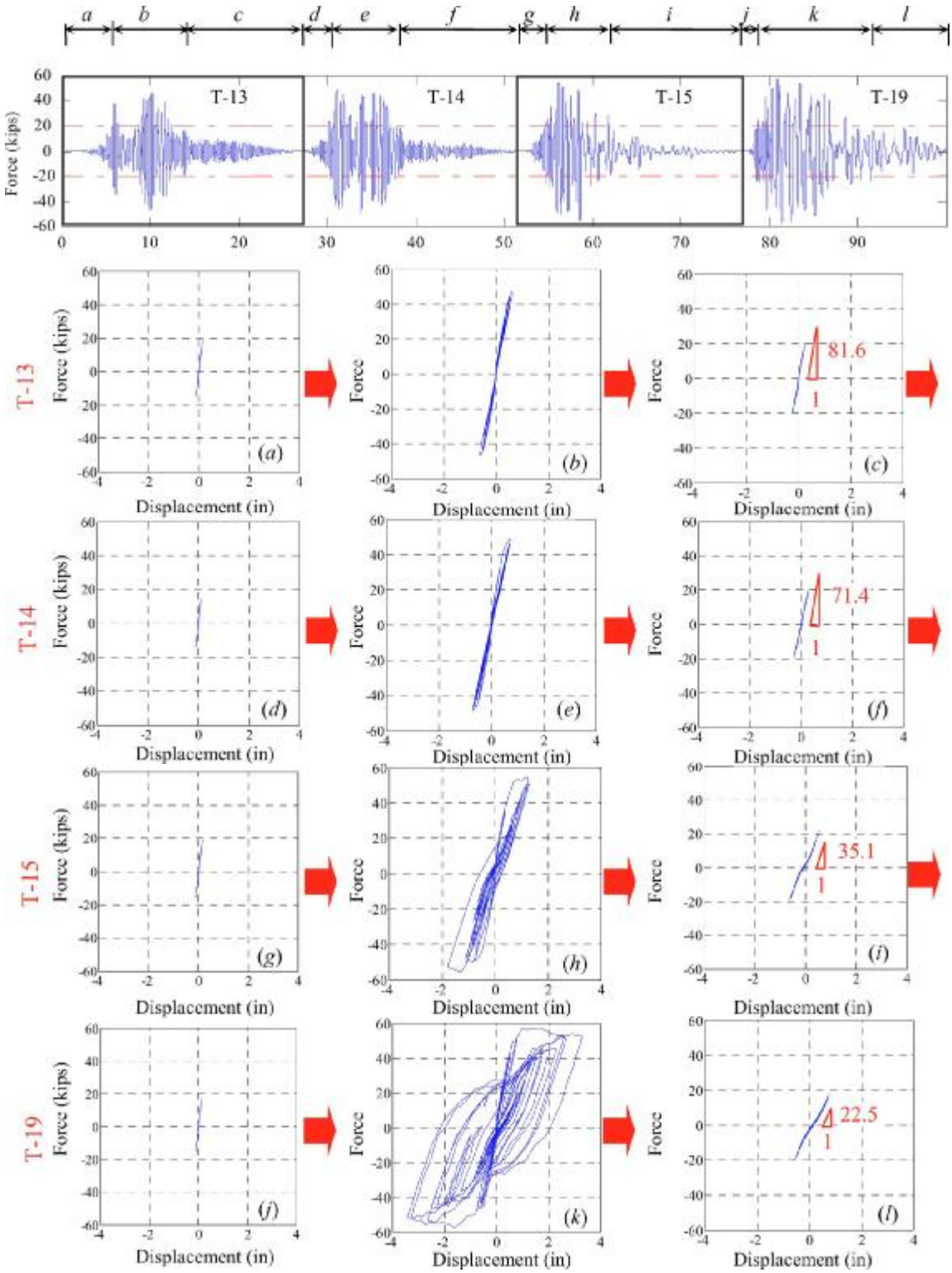


Figure 41 Experimental Hysteresis Curves

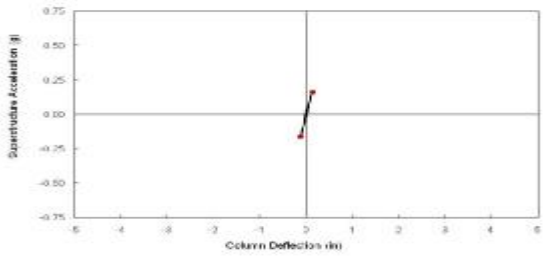


T-12

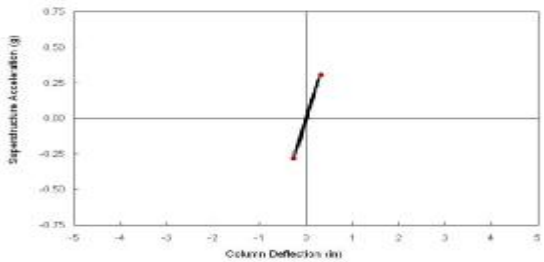


T-13

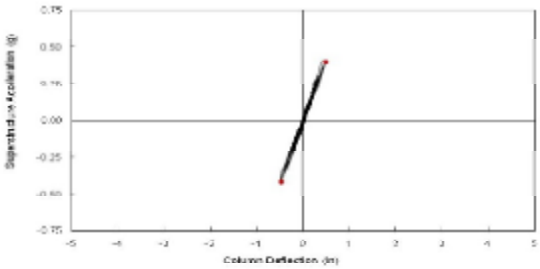


T-14

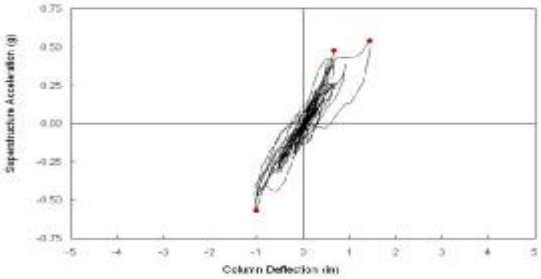


T-15

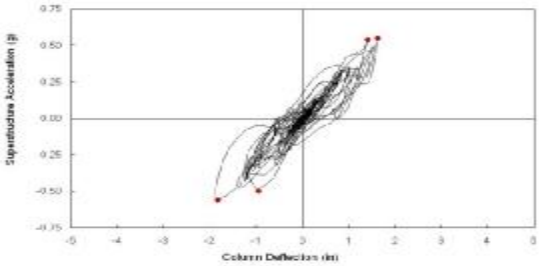


T-16

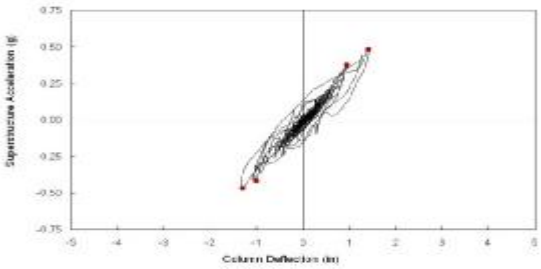


T-17

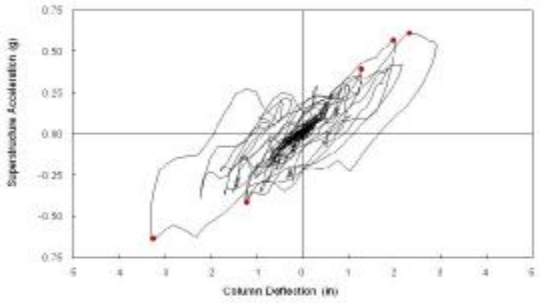


T-18

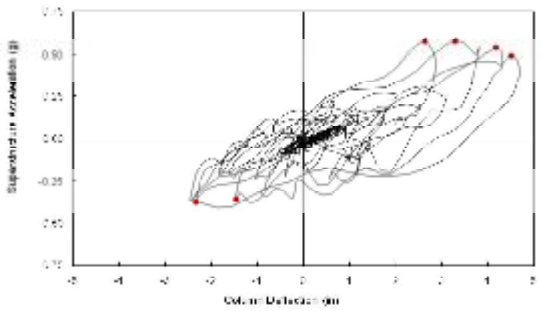

T-19

Figure 42 Measured Hysteresis

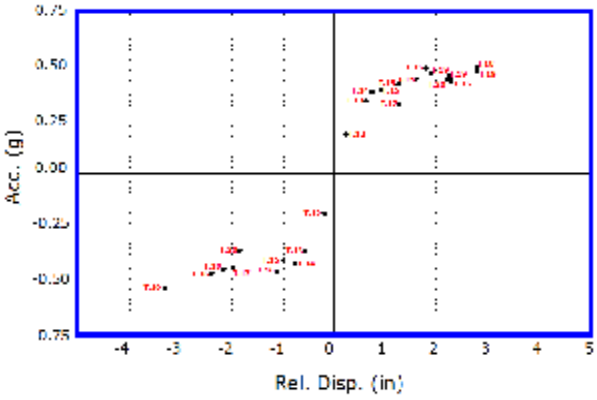


Bent 1

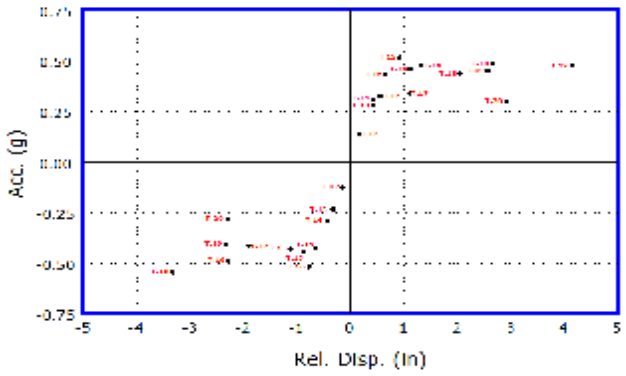


Bent 2

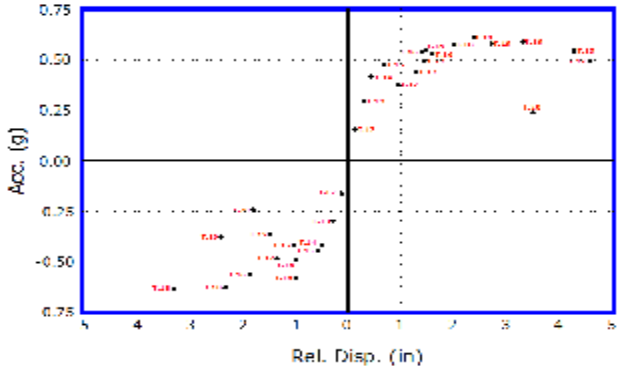


Bent 3

Figure 43 Excursion Points

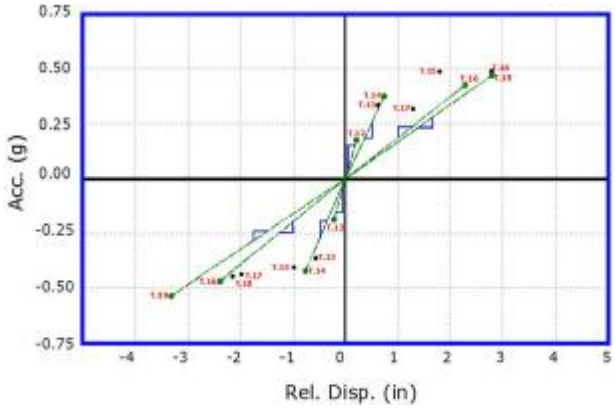


Bent 1

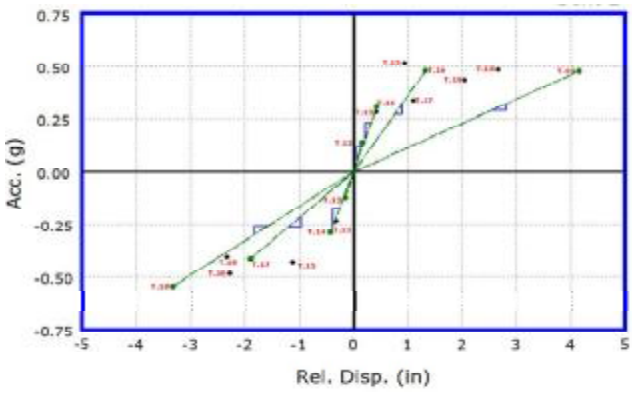


Bent 2

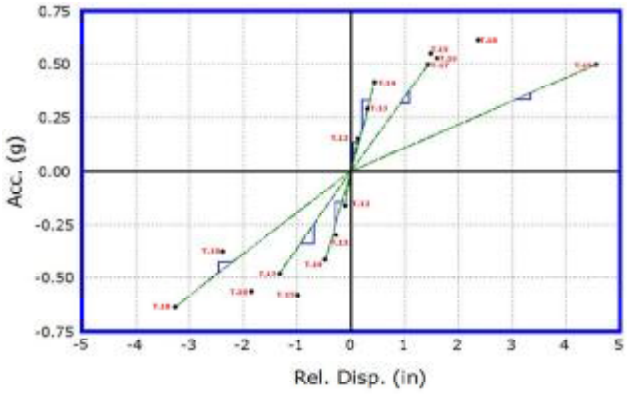


Bent 3

Figure 44 Slope Estimation

Furthermore, a line is drawn from each excursion point to the origin and its slope is measured, as shown in Fig. 44. The slope is normalized by the slope resulting from Test 12 in which the structure is undamaged. Therefore, the normalized slope (that is directly from the measured displacement and acceleration responses), referred to as the measured slope, corresponds to the stiffness correction coefficient (that is identified from the measured acceleration response). If the measured slope is equivalent to the identified stiffness correction coefficients, it will validate the proposed capacity estimation method by using the measured stiffness combined with the pushover capacity curve.

Connecting the maximum excursion point during each test is compared with the identified stiffness from the white noise response of the bridge. White noises have been input to the structure only at the four levels (undamaged before test12 and damaged after tests 14, 17 and 19). The stiffness values identified from each white noise response are compared to the slope of the line connecting the origin and the maximum excursion point reached during the seismic test before the selected white noise test. The average of the positive and the negative slopes is taken and normalized by the slope at T-12 for the comparison purposes.

Tables 6 through 8 compare the measured slopes with the stiffness values identified by the two optimization methods – the quasi-Newton and the genetic algorithm, respectively for Bent 1, Bent 2, and Bent 3. The values in parentheses indicate the error between the measured slope and the identified stiffness.

In summary, the seismic shaking table tests validated the proposed pushover-based capacity estimation method by validating (1) the assumption of a linear and time-invariant system for a damaged structure experiencing low-amplitude ambient vibration, and (2) the pivot points consistent with displacement measurement, and demonstrating that (3) the stiffness values identified by the two different optimization methods agree well with the measured slopes. In conclusion, the shaking table tests demonstrated that the post-event stiffness values can be used for estimating the remaining capacity based on the pushover curve.

Table 6 Comparison of Measured Slope with Identified Stiffness for Bent-1

| | Measured Slope | Stiffness by Quasi-Newton | Stiffness by Genetic Algorithm |
|---|---|---|---|
| **WN-1** | 1.000 | 1.000 | 1.000 |
| **WN-2** | 0.612 | 0.679 (11.09%) | 0.721 (17.87%) |
| **WN-3** | 0.220 | 0.244 (10.74%) | 0.224 (1.83%) |
| **WN-4** | 0.190 | 0.203 (6.55%) | 0.211 (11.01%) |

Table 7 Comparison of Measured Slope with Identified Stiffness for Bent-2

| | Measured Slope | Stiffness by Quasi-Newton | Stiffness by Genetic Algorithm |
|---|---|---|---|
| **WN-1** | 1.000 | 1.000 | 1.000 |
| **WN-2** | 0.838 | 1.013 (20.80%) | 0.748 (-10.77%) |
| **WN-3** | 0.345 | 0.392 (13.83%) | 0.286 (-17.03%) |
| **WN-4** | 0.165 | 0.203 (22.67%) | 0.200 (21.14%) |

Table 8 Comparison of Measured Slope with Identified Stiffness for Bent-3

| | Measured Slope | Stiffness by Quasi-Newton | Stiffness by Genetic Algorithm |
|---|---|---|---|
| **WN-1** | 1.000 | 1.000 | 1.000 |
| **WN-2** | 0.776 | 0.718 (-7.56%) | 0.748 (-3.65%) |
| **WN-3** | 0.305 | 0.212 (-30.46%) | 0.286 (-6.08%) |
| **WN-4** | 0.130 | 0.129 (0.64%) | 0.200 (53.56%) |

## 3.9 EXPLORATORY SOFTWARE AND FIELD EVALUATION

An exploratory software package has been developed in this project using selected damage assessment methods developed in this project. It has been integrated into a sensor monitoring system in an instrumented testbed bridge in California for long-term performance evaluation, demonstration, and user training.

### 3.9.1 Comparison of Damage Assessment Methods

In Task 1 of this project, we have investigated five different methods for post event damage assessment. Among them, the autoregressive (AR) model and the nonlinear damping methods are capable of damage detection, i.e., detecting the occurrence of structural damage, while the extended Kalman filter, the quasi-Newton optimization, and the genetic algorithm (GA) optimization are capable of damage assessment, i.e., not only detecting the occurrence of damage, but also locating and quantifying the extent of damage.

All of these methods were validated using the same seismic shaking table test results, and they all resulted in similar results, consistent with observed damage to the bridge during the shaking table tests. Figures 45 through 47 compares the stiffness identification results respectively for the three bents, by the extended Kalman filter using the seismic data, the quasi-Newton optimization using the white noise data, and the genetic algorithm-based optimization using both the seismic and the white noise data.

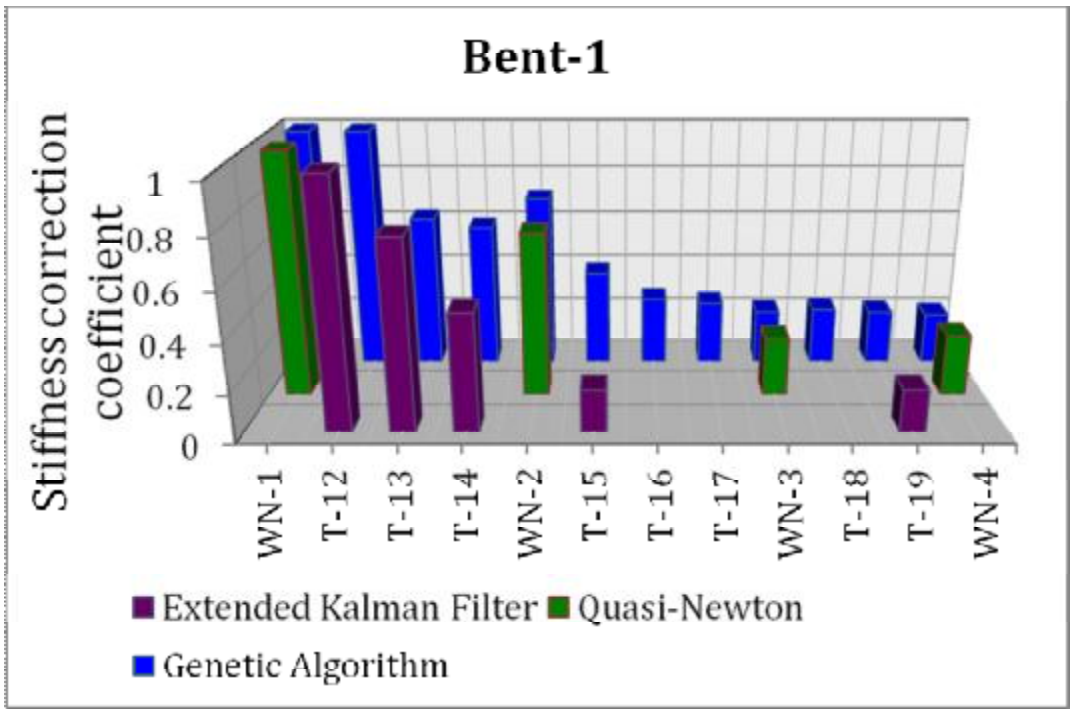


Figure 45 Comparison of Damage Assessment Results for Bent 1

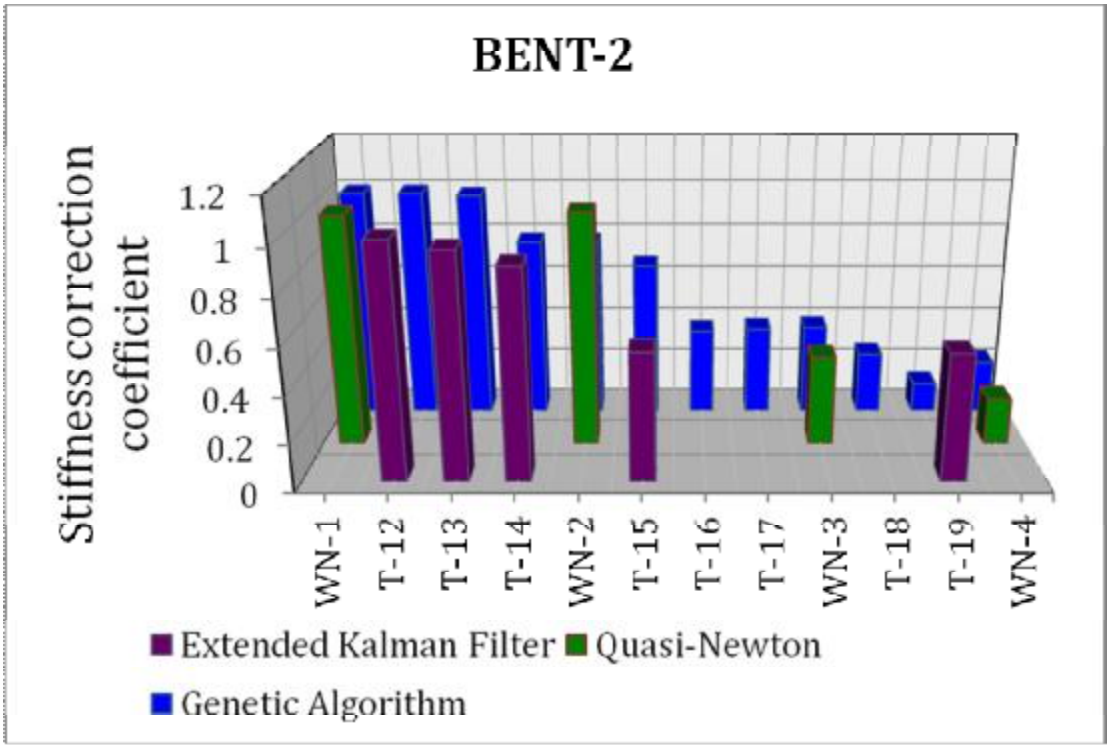


Figure 46 Comparison of Damage Assessment Results for Bent 2

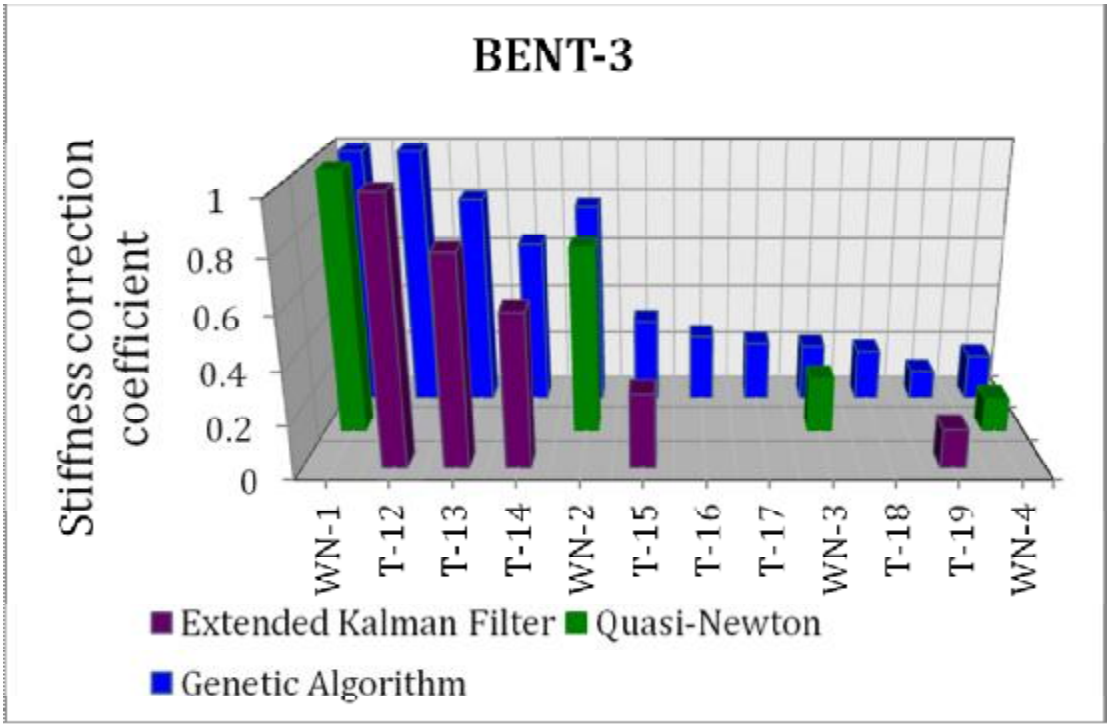


Figure 47 Comparison of Damage Assessment Results for Bent 3

Table 9 compares the pros and cons of these damage assessment methods. Considering the computational stability, the AR method has been chosen for rapid damage detection and the GA-based optimization method for detailed damage assessment in the software.

Table 9. Comparison of Different Damage Assessment Methods

| Method | Pros | Cons |
|---|---|---|
| Autoregressive Model | • Short analysis time<br>• Sensitive to damage | • No information on damage location |
| Nonlinear damping | • Short analysis time<br>• Easy to implement | • No information on damage location<br>• Needs long response measurements<br>• Sensitive to the random decrement threshold |
| Quasi-Newton-Based Optimization | • Stable identification results<br>• Identifies stiffness and damping<br>• Easy to implement | • Lack of guidance in assigning weights in objective functions<br>• Sensitive to selection of start point |
| Extended Kalman Filter | • Real-time instantaneous identification<br>• Capable of handling nonlinear response | • Divergence problem<br>• Sensitive to selection of initial values |
| Genetic Algorithm-Based Optimization | • Reliable results avoiding local optimal<br>• Identifies stiffness and damping<br>• Easy to implement | • Lack of guidance in assigning weights in objective functions |

## 9.2 Software Framework

The selected damage detection and assessment methods have been developed into computer algorithms and coded into an exploratory software package named “The Bridge Doctor”. The framework of the software is illustrated in Fig. 48.

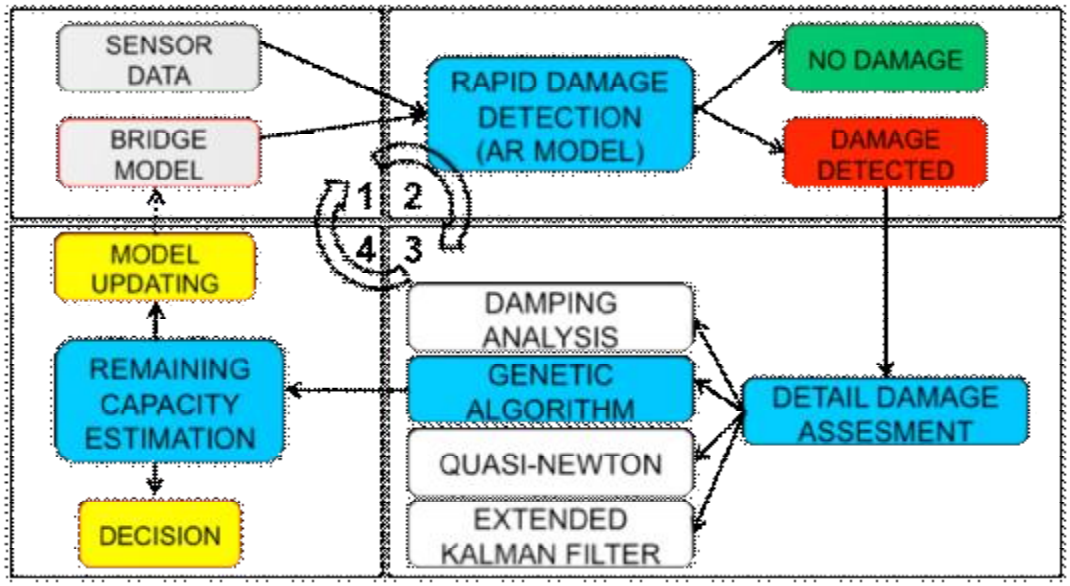


Figure 48. Block Diagram of Software Framework

The entire post-event process for an instrumented bridge consists of the following four steps:

Step I: Sensor Data Acquisition

When sensors on a bridge are triggered by an event, the software will automatically acquire sensor data via Internet in real time.

Step II: Rapid Damage Screening:

A rapid damage screening will be first performed based on the AR model. If the damage index exceeds the preset threshold, the software will automatically proceed to the next step. Otherwise, the software will display that no damage is detected.

Step II: Detailed Damage Assessment

A more detailed damage assessment will be performed in terms of the location and severity of the damage, based on the measured ground motion acceleration and the structural acceleration responses. To be more specific, the change of element stiffness values will be identified and as a result, the locations of damage be identified.

Step III: Remaining Capacity Estimation

Based on the identified stiffness degradation at each column, the analytical pushover curves will be updated and the current performance point (the pivot point) identified. In comparison with the designed ultimate capacity, the remaining capacity of the bridge structure will be estimated. Such information is highly useful for post-event emergency response operation, as well as for decision making in terms of selecting and designing the most cost-effective damage repair methods.

### 3.9.3 Testbed and Field Implementation

The Bridge Doctor software has been customized to a testbed bridge, the Jamboree Overcrossing, in Irvine, CA, and integrated with the sensor monitoring system on the bridge for long-term performance evaluation and demonstration. A copy of the software has been installed on the Caltrans Earthquake Engineering Office for long-term evaluation.

As shown in the photo in Fig. 49, the Jamboree Overcrossing is a three-span continuous cast-in-place post-tension concrete box-girders bridge with a total length of 364 ft. The bridge was straight and supported on two monolithic single columns and sliding bearings

on both abutments. There were offsets from the centers of the columns to the central line of the superstructure. It was instrumented with 16 accelerometers and one displacement sensor with their locations shown in Fig. 50. The sensors are powered by solar energy. The data logger at the bridge site is linked to Internet wirelessly through point-to-point antennas. The PI developed this real-time sensor system under the support of Caltrans and the monitoring data are available in real time at the PI's website: http://mfeng.calit2.uci.edu (Feng and Kim, 2001). The wireless Internet for the bridge is currently be upgraded and to be completed by Spring, 2011.

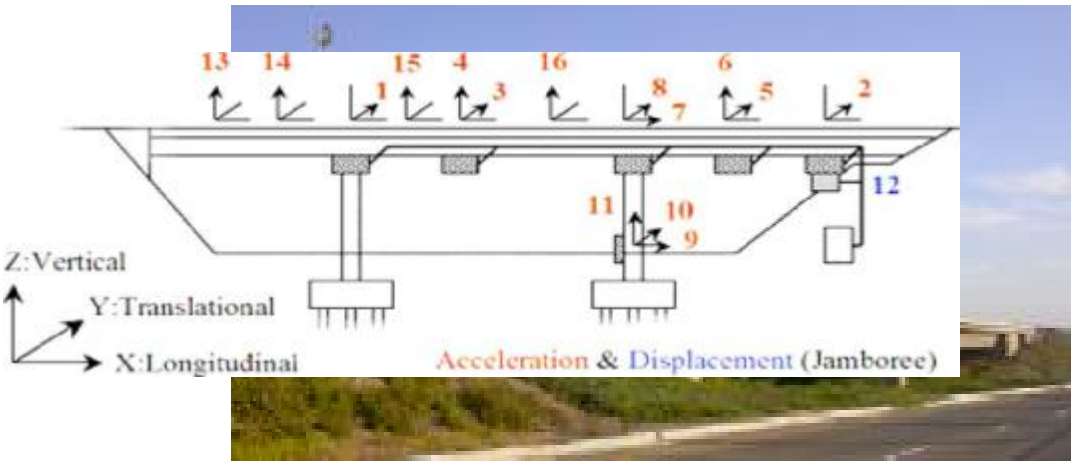


Figure 49 Instrumented Jamboree Rd. Overcrossing

Figure 50 Instrumented Jamboree Rd. Overcrossing

This testbed evaluation and demonstration involving Caltrans practitioners will serve as a critical step toward future commercialization of the software products in highway bridges for (1) real-time and remote assessment of post-event bridge damage and capacity, (2) structural condition-based bridge inspection, maintenance, and management, and (3) improvement of bridge design and construction.

# 4. PLAN FOR IMPLEMENTATION

This IDEA project has successfully delivered an exploratory Bridge Doctor software package incorporated with the damage and capacity assessment methods and algorithms developed in this study. The software has been customized to a testbed bridge in California that is instrumented with accelerometers, and transferred to Caltrans for long-term performance evaluation and demonstration.

Once the upgrade of the data logger and wireless Internet at the testbed bridge is completed, users at the Caltrans Earthquake Engineering Office and any authorized users will be able to view and download the sensor data in real time using the Bridge Doctor software at any time and from any locations. Immediately after an earthquake, the software will acquire sensor data via Internet and perform rapid damage screening on the bridge. If damage is detected, detailed assessment will be carried out to identify the locations and extents of the damage, and further estimating the remaining load-carrying capacity of the bridge. The results from the software can be used to assist making decisions about post-event bridge operations, and prioritization of bridge repair and retrofit. In addition, the users can also use the software to update the bridge analytical model based on ambient (traffic) vibration response measurement for long-term bridge health monitoring.

# 4.1 ROADMAP TOWARD IMPLEMENTATION

Implementation of the Bridge Doctor software is planned in two major stages: evaluation/validation and commercialization. The long-term field evaluation and demonstration of the Bridge Doctor software at the testbed bridge will be continued for at least ten years, during which the project team will interact with the end users and improve the algorithms and software to enhance their reliability, computational efficiency, and user-friendliness, based on comments and suggestions by the Caltrans users.

However, it is unknown when the software will be validated by a real earthquake. This difficulty can potentially delay the market entry of the software. Therefore, this project team is currently establishing a partnership with the Public Works Research Institute (PWRI) to collect data from the seismic shaking table tests of full-scale concrete bridges by the E-Defense project in Japan, which is equipped with the world largest seismic shaking tables.

By the end of 2011, Bridge Doctor will be made into a prototype product upon validation by the full-scale shaking table tests. A number of demonstration and training workshops will be held to potential early adopters including Caltrans and other DOT's at earthquake-prone states. In the end of 2012, the first generation of product – Bridge Doctor I – will be released.

The planned Bridge Doctor products are shown in Table 10. They include the first generation, *Bridge Doctor I*, for post-event damage assessment of concrete bridges, and the second generation, *Bridge Doctor II*, for post-event damage assessment of steel and other types of bridges. The software will be available in a general version and a customized version. The general version has a module that allows the users to customize the software for their specific bridges, while the customized version is made for a specific bridge to save

users' effort. A long-term service package is usually associated with the customized version.

In order to capture a broader market, Newport Sensors, Inc., plans to apply the concept and methods of Bridge Doctor developed in this IDEA project to buildings and other civil engineering structures. The Building Doctor products are also listed in Table 10.

Table 10 Product Metrics

| **Products** | **General** | | **Customized** |
|---|---|---|---|
| | **Single-user** | **Multi-user** | |
| Damage assessment of concrete bridges | *Bridge Doctor I–G-S* | *Bridge Doctor I–G-S* | *Bridge Doctor I–C* |
| Damage assessment of other types of bridges | *Bridge Doctor II–G-S* | *Bridge Doctor II–G-S* | *Bridge Doctor II–C* |
| Health monitoring of bridges | *Bridge Doctor III–G-S* | *Bridge Doctor III–G-S* | *Bridge Doctor III–C* |
| Damage assessment of concrete buildings | *Building Doctor I–G-S* | *Building Doctor I–G-S* | *Building Doctor I–C* |
| Damage assessment of other types of buildings | *Building Doctor II–G-S* | *Building Doctor II–G-S* | *Building Doctor II–C* |
| Health monitoring of buildings | *Building Doctor III–G-S* | *Building Doctor III–G-S* | *Building Doctor III–C* |

A 5-year post-IDEA roadmap toward commercialization is summarized in Table 11, which includes the market entry time and the estimated revenue of the Bridge Doctor and

Building Doctor products. It is noted that revenues from the service associated with the customized software are not included in this table.

In addition, the company plans to further apply the post-even damage assessment methods developed in this IDEA project for long-term structural health monitoring. Considering the aging and structural deterioration of the nation's civil engineering structures, demands for such software are expected to continue rise. The software, linked with sensor systems, can be incorporated into highway bridge inspection and management programs. This will eventually lead to a paradigm shift from the current time-based periodic inspection to more cost-effective condition-based inspection.

Newport Sensors, Inc. is also developing a marketing strategy to package a complete structural health monitoring system by integrating the software with the company's unique fiber optic accelerometers (successfully developed and commercialized under the support of another IDEA grant). Currently no such a system is commercially available.

Table 11. Road Map toward Commercialization

| Time By | Milestones | Estimated Revenue ($k) |
|---|---|---|
| 12/31/2011 | • Field evaluation and improvement of the software in collaboration with Caltrans<br>• Validation by full-scale seismic shaking table tests in collaboration with PWRI and E-Defense in Japan | |
| 3/31/2012 | Software demonstration and training to Caltrans Bridge Maintenance Division and California Office of Emergency Services | |
| 8/31/2012 | Software demonstration and training to DOT's of earthquake-prone states | |
| 12/31/2012 | Release Bridge Doctor I and secure one adoption of<br>***Bridge Doctor I – G - M*** | $50 |
| 12/31/2013 | • Secure 5 adoptions of ***Bridge Doctor I - G – S***<br>• Secure 5 adoptions of ***Bridge Doctor I – G - M***<br>• Secure 5 adoptions of ***Bridge Doctor I – C***<br>• Release Bridge Doctor II and secure one early adoption of<br>***Bridge Doctor II – G - M*** | $8*5=$40<br>$50*5=$250<br>$50*5=$250<br><br>$50 |
| 12/31/2014 | • Secure 30 adoptions of ***Bridge Doctor I***<br>• Secure 5 adoptions of ***Bridge Doctor II – G - S***<br>• Secure 5 adoptions of ***Bridge Doctor II – G - M***<br>• Secure 5 adoptions of ***Bridge Doctor I – C***<br>• Release Building Doctor I and secure one early adoption ***Building Doctor I – G -M*** | $1,080<br>$8*5=$40<br>$50*5=$250<br>$50*5=$250<br><br>$60 |

## 4.2 POTENTIAL PAYOFF FOR PRACTICE

Due to aging and deterioration, our nation's highway transportation infrastructure is becoming increasingly vulnerable to natural and man-made disasters such as destructive earthquakes, hurricanes, vehicle overloading, and traffic accidents. Lack of information about post-event damage in highway bridges can cause safety hazards, halts mobility of the transportation network, and disrupt emergency response. It, therefore, is important to quickly assess the post-event condition of bridges in terms of locations and severity of damage and capability for carrying traffic loads.

Structural damage assessment typically relies on a detailed visual inspection and evaluation that is time consuming and requires physical presence of an inspection team at the bridge site. The current state of practice lacks the urgently needed elements for assisting a rapid decision-making process that could be accomplished within minutes rather than days or months. Installation of sensor systems with remote, real-time monitoring capabilities and appropriate push-button structural damage assessment software will provide necessary tools for rapid implementation of effective post-event operations. The real-time monitoring and damage assessment results can timely provide highway authorities with information to make decisions in terms of issuing early warning, traffic rerouting, and repair prioritization immediately after a disastrous event.

In addition to post-event operations, the proposed research can make a broader impact on the safety and security of the nation's aging highway transportation infrastructure and result in a high payoff for bridge management practice. Although this project focuses on damage caused by destructive events such as earthquakes, the same methods based on identification of structural stiffness change can be applied to detect structural degradation due to aging

and to assess structural safety under operational (traffic) loads. The real-time structural integrity information can be used for daily bridge management, changing the current time-based periodic inspection to structural condition-based inspection, which is more timely and cost-effective. The monitoring results can also assist the bridge owners to make more objective decisions when prioritizing bridges for structural repair, strengthening, retrofit and rehabilitation. Furthermore the monitored structural performance can provide valuable feedback for improving the current bridge structural design and construction practices.

# REFERENCES:


Alimoradi A., Miranda E., Taghavi S. and Naeim F. (2006). "Evolutionary modal identification utilizing coupled shear-flexural response - implication for multistory buildings - part I: Theory. Structural Design of Tall and Special Buildings", 15(1):51–65, 2006.

Au F. T. K., Cheng Y. S., Tham L. G., and Bai Z. Z. (2003), "Structural damage detection based on a micro-genetic algorithm using incomplete and noisy modal test data. " " Journal of Sound and Vibration, 259(5):1081–1094, 2003.

Bouc R. (1967), "Forced vibration of mechanical systems with hysteresis." Proc., 4th Conf. on Non-linear Oscillations, Prague, Czechoslovakia.

Chou J. H. and Ghaboussi J. (2001), "Genetic algorithm in structural damage detection". Computers & Structures, 79(14):1335– 1353.

Clough R. W. (1966), "Effects of stiffness degradation on earthquake ductility requirement." Rep. No. 6614, Struct. And Mat. Res., University of California, Berkeley.

Doebling, S.W., Farrar, C.R., Prime, M.B. and Shevitz, D.W., (1996) "Damage identification and health monitoring of structural and mechanical systems from changes in their vibration characteristics : a literature review", Los Alamos National Laboratory Report LA-13070-MS, Los Alamos National Laboratory, Los Alamos, NM 87545

Emori K. and Schnobrich W. C. (1981), "Inelastic Behavior of Concrete Frame-Wall Structures." Journal of the Structural Division, ASCE, 107(1), pp.145-164

FEMA 356, 2000. "Prestandard and Commentary for the seismic rehabilitation of buildings," Building Seismic Safety Council, Washington, D.C., November

Feng, M. Q. and Kim, D.K. (2001). "Long-Term Structural Performance Monitoring of Two Highway Bridges", Technical Report of Caltrans.

Feng, M.Q. (2009), "Application of Structural Health Monitoring in Civil Infrastructure", Smart Structures and Systems, Vol. 05, No. 4, pp. 469-482.

Franco G., Betti R. and Lus H. Identification of structural systems using an evolutionary strategy. Journal of Engineering Mechanics-Asce, 130(10):1125–1139, 2004.

Friswell M. I., Penny J. E. T. and Garvey S. D.(1998), “A combined genetic and eigensensitivity algorithm for the location of damage in structures”. Computers & Structures, 69(5):547–556, 1998.

Fugate, M. L., Sohn, H. and Farrar, C. R., (2001) Vibration-Based Damage Detection Using Statistical Process Control, Accepted for publication of Mechanical Systems and Signal Processing

Haralampidis Y., Papadimitriou C. and Pavlidou M. (2005), “Multi-objective framework for structural model identification”. Earthquake Engineering & Structural Dynamics, 34(6):665–685, 2005.

Hoshiya S, and Saito E. Structural Identification by Extended Kalman Filter. *Journal of Engineering Mechanics* 1984; **110**(12): 1757-1770.

Johnson N. S., Saiidi M. and Sanders D. H. (2006), “Large-Scale Experimental and Analytical Seismic Studies of a Two-Span Reinforced Concrete Bridge System”, Report No. CCEER-06-02, Center for Civil Engineering Earthquake Research, Department of Civil and Environmental Engineering/258, University of Nevada Reno, Nevada 89557

Kalman, R.E., (1960) “A New Approach to Linear Filtering and Prediction Problems”, Journal of Basic Engineering, 82(1): 35-45.

Koh C. G., Chen Y. F. and Liaw C. Y. (2003), “A hybrid computational strategy for identification of structural parameters”. Computers & Structures, 81(2):PII S0045–7949(02)00344–9, 2003.

Kouchmeshky B., Aquino W., Bongard J. C. and Lipson H. (2007), “Co-evolutionary algorithm for structural damage identification using minimal physical testing”. International Journal for Numerical Methods in Engineering, 69(5):1085–1107, 2007.

Lee S. Y., Park T., and Voyiadjis G. Z. (2008). “Detection of stiffness reductions in concrete decks with arbitrary damage shapes using incomplete dynamic measurements”. Journal of Engineering Mechanics-Asce, 134(7):567–577.

Loh, C.H., and Chung, S.T., (1993) “A Three-Stage Identification Approach for Hysteretic Systems”, Earthquake Engineering and Structural Dynamics, 22: 129-150.

Loh, C.H., and Tou, I.C., (1995) “A System Identification Approach to the Detection of Changes in Linear and Non-linear Structural Parameters” Earthquake Engineering and Structural Dynamics, 24: 85-97.

Park Y. J., Reinhorn A. M. and Kunnath S. K. (1987), "IDARC: Inelastic damage analysis of reinforced concrete frame – shear-wall structures." Tech. Rep. NCEER-87-0008, State University of New York at Buffalo, Buffalo, NY

Park, H. W., Shin, S. B. and Lee, H. S., (2001) Determination of an optimal regularization factor in system identification with Tikhonov function for linear elastic continua International Journal for Numerical Methods in Engineering, 51(10), pp.1211-1230

Park, H. W., Park, M. W., Ahn, B. K. and Lee, H. S., (2007) 1-norm based regularization scheme for system identification of structures with discontinuous system parameters, International Journal for Numerical Methods in Engineering, Vol. 69, No. 3, pp. 504-523

Paulay T., Priestley M. J. N., (1992). Seismic Design of Reinforced Concrete and masonry buildings. Wiley, New York.

Polak E. (1997), "Optimization: algorithms and consistent approximations", Springer-Verlag, NY

Raich A.M. and Liszkai T. R., (2007). "Improving the performance of structural damage detection methods using advanced genetic algorithms". Journal of Structural Engineering-Asce, 133(3):449–461, 2007.

Rao M. A., Srinivas J. and Murthy B. S. N. (2004), "Damage detection in vibrating bodies using genetic algorithms", Computers & Structures, 82(11-12):963–968, 2004.

Saiidi M. (1982), "Hysteresis Models for Reinforced Concrete." Journal of the Structural Division, ASCE, 108(5), pp. 1077-1087

Sain P. M., Sain M. K. and Spencer B. F. (1997), "Models of hysteresis and application to structural control." Proc. of American Control Conference, pp. 16-20

Shim M. B. and Suh M.W. (2003), "Crack identification using evolutionary algorithms in parallel computing environment", Journal of Sound and Vibration, 262(1):PII S0022–460X(02)01031–3/

Sivaselvan M. V. and Reinhorn A. M. (2000), "Hysteretic models for deteriorating inelastic structures." Journal of Engineering Mechanics, 126(6), pp. 633-640.

Sohn, H., Czarnecki, J.J. and Farrar, C.R., (2000) "Structural Health Monitoring using Statistical Process Control", Journal of Structural Engineering, ASCE, Vol.126, No.11, pp.1356-1363

Sohn, H. and Farrar, C.R., (2001) Damage diagnosis using time series analysis of vibration signals, Smart Materials and Structures, vol.10, pp.446-451

Sohn H., Farrar C. R., Hemez F. M., Shunk D. D., Stinemates D. W. and Nadler B. R. (2003), "A Review of Structural Health Monitoring Literature: 1996-2001", Los Alamos National Laboratory Report, LA-13976-MS

Takayanagi T. and Schnobrich W. C. (1979), "Non-Linear Analysis of Coupled Wall Systems." Earthquake Engineering and Structural Dynamics, Vol. 7, pp. 1-22.

Takeda T., Sozen M. A. and Nielsen N. N. (1970), "Reinforced concrete response to simulated earthquakes." Journal of the Structural Division, ASCE, 96(12), pp. 2557-2573

Wen Y.-K. (1976), "Method for random vibration of hysteretic systems." Journal of Engineering Mechanics Division, ASCE, 102(2), pp. 249-263

Yang, J.N., Lin, S., Huang, H., and Zhou, L., (2005) "An Adaptive Extended Kalman Filter for Structural Damage Identification", Journal of Structural Control and Health Monitoring, 13(4): 849-867.

Yun, C.B., and Shinozuka, M., (1980) "Identification of Nonlinear Structural Dynamic Systems", Journal of Structural Mechanics, 8: 187-203.

Zhang, Q. W., (2007) Statistical damage identification for bridges using ambient vibration data, Computers and Structures, vol.85, pp 476-485